UNIVERSITY
OF TRENTO - Italy
Department of Industrial Engineering

Doctoral School in Materials Science and Engineering
XXV cycle

Computer simulation of electron transport in solids with applications to materials analysis and characterization

Maurizio Dapor

Trento - April 24^{th}, 2013

Computer simulation of electron transport in solids with applications to materials analysis and characterization

Maurizio Dapor
dapor@fbk.eu

Approved by:

Prof. S. Gialanella, Tutor,
University of Trento

PhD committee:

Prof. P. Scardi,
University of Trento

Prof. S. Schmauder,
Universität Stuttgart

Prof. C.-K. Tsung,
Boston College

University of Trento
Department of Industrial Engineering
Doctoral Thesis
Maurizio Dapor - 2013
Published in Trento (Italy) by University of Trento

ISBN: 978-88-8443-471-5

to my dearest father, always alive in my mind and in my heart

Acknowledgements

Firstly, I would like to gratefully thank my sweet wife, our beloved children, and my dear parents, for their immense patience, their generous availability, and their continuous support.
It is also a pleasure to mention many people, friends and colleagues, who, with their enthusiasm, invaluable suggestions, ideas, and competence, considerably contributed to achieve the results presented in this work.
I wish to express my warm gratitude to Diego Bisero, Lucia Calliari, Giovanni Garberoglio, and Simone Taioli, for their sincere friendship, encouragement, and excellent scientific suggestions.
I am particularly grateful to my tutor and advisor, Stefano Gialanella, for his patient guidance and continuous help.
I am also indebted with all the researchers who made possible with their help the completion of the project: Nicola Bazzanella, Eric Bosch, Mauro Ciappa, Michele Crivellari, Sergey Fanchenko, Wolfgang Fichtner, Massimiliano Filippi, Stephan Holzer, Emre Ilgüsatiroglu, Beverley J. Inkson, Mark A.E. Jepson, Alexander Koschik, Antonio Miotello, Cornelia Rodenburg, John M. Rodenburg, Manoranjan Sarkar, Giorgina Scarduelli, Stefano Simonucci, and Laura Toniutti.
I would like to thank all my colleagues at the Interdisciplinary Laboratory for Computational Science (LISC) in Trento for the fruitful discussions. The stimulating atmosphere of LISC provided the ideal environment to work to this project.
I am also indebted to the Department of Engineering Materials of the University of Sheffield and the Integrated Systems Laboratory of the Swiss Federal Institute of Technology (ETH) of Zurich for their warm hospitality.

Contents

Chapter 1

Introduction

The interaction of electron beams with matter is a scientific topic that has interested many researchers since the first half of the twentieth century. In this regard, we can find in the literature many excellent works, among which the classic reviews of Bothe [1] and Birkhoff [2]. In the last decades several books and articles appeared, both experimental and theoretical, devoted to this subject: see, for example the works by Ibach [3], Niedrig [4], Goldstein *et al.* [5], Newbury *et al.* [6], Feldman and Mayer [7], Sigmund [8], and Egerton [9, 10]. Many papers and books are dedicated specifically to transport Monte Carlo: among the numerous excellent works, see in particular the reviews by Carter and Cashwell [11], Salvat *et al.* [12], Shimizu and Ding Ze-Jun [13], Joy [14], and Bielajew [15].

1.1 Interaction of electrons with solid targets

In a typical experiment in which an electron beam impinges on a solid target, many electrons of the primary electron beam can be backscattered, after having interacted with the atoms and electrons of the target. A fraction of them conserves the original kinetic energy, having experienced only elastic scattering collisions with the atoms of the target: these electrons constitute the elastic peak, whose maximum is located at the energy of the primary beam. Electrons scattered by electron-phonon collisions can be found very close to the elastic peak: their energy loss is typically lower than 0.1 eV. Electrons inelastically scattered by plasmon excitations can be found in a range of approximately 50 eV below the elastic peak. They represent the

electrons belonging to the primary electron beam that emerge from the surface after having suffered a single inelastic collision with a plasmon. Multiple collisions with plasmons are present in the spectrum as well: their intensities are quickly decreasing as the number of inelastic collisions increases. Electrons from direct ionization as well as Auger electrons can be found in the range from 50 eV to the energy of the elastic peak. The secondary electrons produced by a cascade process are those electrons which have been extracted from the atoms by inelastic electron-electron collisions and are able to emerge from the target surface. Their energy distribution presents a pronounced peak in the very low energy region of the spectrum, typically below 50 eV. The secondary electron emission yield is conventionally measured integrating the area of the spectrum from 0 to 50 eV including, in such a way, also the tail of backscattered electrons. The number of backscattered electrons in this energy region is negligible and can be safely ignored unless the primary energy be very low as well.

1.2 Structure of the work

Monte Carlo (MC) technique allows solving mathematical and physical problems of great complexity. One of the main topics that can be approached using the MC strategies concerns the study of the electron-solid interaction (transport MC). The aim of this work is to investigate some physical problems related to the transport of electrons in solid targets using our transport MC codes. The numerical and theoretical results will be validated through a comparison with experimental evidences. We also tackle issues related to methodological aspects. In particular, we will make systematic comparisons among different calculation schemes. Different expressions for the calculation of cross sections and/or stopping power and different simulation methods will be compared with experimental data both acquired with specifically designed experiments – involving SEM, AES, and REELS – both taken from literature studies, in order to establish the limits of validity of the various theories and methods which have been proposed in the literature.

The thesis is divided in four parts.

In the first one the basic aspects of the scattering mechanisms are summarized. In particular, after a summary of the basic theoretical aspects, our numerical calculations of the cross-sections relative to the various scattering processes are presented and compared with experimental data and/or theo-

retical calculations (by other authors) with the aim to validate the present approach.

The second part of the thesis is dedicated to the methodological aspects and, in particular, to the description of the present Monte Carlo method: we provide details, in particular, of the two MC schemes we have implemented in our code, i.e., the *continuous-slowing-down approximation scheme* (were electrons are assumed to continuously lose energy along their travel into the solid) and the *energy-straggling approach* (where the statistical fluctuations of the electron energy losses are properly taken into account).

The third part is devoted to a brief description of the experimental methods: in this context, they are fundamental tools for the validation of the present MC calculations and for the comparison between the two MC schemes described in the second part. The materials used for the experiments and the MC simulations are also briefly described.

In the fourth part of the thesis, some critical aspects of the present MC approaches along with specific MC methodologies concerning particular physical processes are discussed; comparison to experimental data are provided; and examples of technological applications are given.

In the appendices, the main theories utilized in our work for the calculations of the various cross-sections are collected: they are the Mott theory of elastic scattering, the Fröhlich theory of electron-phonon interaction, the Ritchie dielectric theory, and the Chen and Kwei theory of the depth dependence of the differential inverse inelastic mean free path. They are described there in order to make it easier and smoother the reading of the main text. Also a list of the papers published by the present author during his PhD course are provided in the last appendix.

1.3 Applications of the MC

The MC schemes presented in the work are applied to various physical processes. Our MC calculations regard, in particular, (i) the backscattering coefficient of electrons emerging from bulks and thin surface films; (ii) the secondary electron yields; (iii) the electron energy distributions (concerning plasmon losses, energy losses of Auger electrons, and secondary electrons). Furthermore, technological applications of Monte Carlo calculations are described. In fact, since transport MC allows predicting the behavior of charged particles traveling through the matter, it can be utilized in many applica-

tions. Among them, on the side of the chemical analysis of the surfaces and the interfaces of materials, let us mention Scanning Electron Microscopy (SEM), Transmission Electron Microscopy (TEM), Reflection Electron Energy Loss Spectroscopy (REELS), and Auger Electron Spectroscopy (AES). Concerning the simulation of the backscattering coefficient, it is utilized in the present work for evaluating the chemical composition of the target and for measuring the thickness of thin surface films – even in case of multi-layered structures. Regarding the secondary electron emission, our MC simulations are used for the study of (1) the line-scan calculations of resist materials with given geometrical cross-sections deposited on silicon substrates; and (2) the energy selective SEM for image contrast in silicon p-n junctions. We shall discuss the above described applications and present some of the results we obtained.

Part I

Electron transport in solid materials

Chapter 2

Electron transport in solids

The Monte Carlo method is used for evaluating the many physical quantities necessary to the study of the interactions of particle-beams with solid targets. The simulation of the relevant physical processes, by random sampling, allows to solve many particle transport problems. Considering the effects of the single collisions and letting the electrons carry out an artificial, random walk it is possible to accurately evaluate the diffusion process.

Studies of backscattered and secondary electrons are of great interest for many analytical techniques. A better comprehension of the processes which occur before the emission of backscattered and secondary electrons would allow a more general understanding of surface physics.

2.1 Electron-beam interactions with solids

During their travel in the solid, the incident electrons lose energy and change direction at each collision with the atoms bound in the solid. Because of the large difference between the masses of the electron and the atomic nucleus, nuclear collisions deflect electrons without any relevant kinetic energy transfer. This process is described by the differential elastic scattering cross-section (which can be calculated by the so-called relativistic partial wave expansion method, corresponding to the Mott cross-section [16]). The Mott cross-section can be approximated with the screened Rutherford formula: this is possible when the conditions corresponding to the first Born approximation are satisified, i.e., for high, even if not relativistic, energy and for low atomic number of the target atom. On the other hand, excitation and

ejection of atomic electrons, and excitation of plasmons, affect the energy dissipation. These processes only slightly affect the direction of the incident electron in the solid, so that they can be described as inelastic events. Plasmon excitations are ruled by the equations for the differential inelastic scattering cross-sections, calculated by the use of Ritchie's dielectric theory [17]. The Fröhlich theory [18] can be used for describing the quasi-elastic electron-phonon interactions. Electron-phonon interactions are considered quasi-elastic for the corresponding energy losses and gains are very small when compared to the plasmon energy losses. When, in insulating materials, electron kinetic energies considerably decreases, trapping phenomena due to the polaronic effect have to be taken into account as well [19].

While for electron kinetic energies higher than 10 keV, MC simulations provide excellent results by the simple use of the Rutherford differential elastic scattering cross-section (elastic scattering) and of the Bethe-Bloch stopping power formula or semi-empirical stopping power formulas (inelastic scattering), when the electron energies become much lower than 5 keV – and this is the case of secondary electron emission – this approach fails. There are many reasons, and the most important ones are related to the three following facts:

(i) As the Rutherford formula is a result of the first Born approximation, it is a high energy approximation.

(ii) Also the Bethe-Bloch formula is valid only for quite high energies; in particular, the Bethe-Bloch stopping power does not provide the correct predictions when the electron energy E becomes lower than the mean ionization energy J. It reaches a maximum for $E \approx 2.5J$ and then approaches zero as E approaches $J/1.166$. Below $J/1.166$, the predicted stopping power becomes negative. The use of semi-empiric approaches can sometimes mitigate the problem. Actually, numerical approaches based on the calculation of the dielectric function - as a function of the energy loss and of the momentum transfer - are necessary to calculate low energy inelastic processes.

(iii) The inclusion of the stopping power in the MC code corresponds to the use of the so-called continuous-slowing-down approximation (CSDA). Such a way of describing energy losses completely neglects that actually electrons lose their energy in several inelastic collisions. Sometimes an electron can even lose all its energy in a single collision. In other words, any realistic model of the electron trajectories should avoid the approximation of continuity in describing the electron energy losses. CSDA can be used (and will be used, when possible, in the present work as well) but only in cases where

the details of the energy loss mechanisms are not crucial for the accurate description of the process under investigation. CSDA can be used, for example, for the calculation of the backscattering coefficient. We will see that, in some specific cases, even the calculation of the secondary electron yield can be performed using CSDA. On the other hand, the description of the energy distributions of the emitted electrons (both backscattered and secondary) have to be performed avoiding the approximation of continuity in the energy loss processes and including *energy straggling* (ES) – i.e., the statistical fluctuations of the energy loss due to the different energy losses suffered by each electron of the penetrating beam – in the calculations.

A detailed approach able to accurately describe low energy elastic and inelastic scattering and to appropriately take into account the energy straggling is required for the description of secondary electron cascade. The whole cascade of secondary electrons must be followed: indeed any truncation, or cut off, underestimates the secondary electron emission yield. What is more, as already discussed, for insulating materials the main mechanisms of energy loss cannot be limited to the electron-electron interaction for, when the electron energy becomes very small (lower than 10-20 eV, say), inelastic interactions with other particles or quasi-particles are responsible for electron energy losses. In particular, at very low electron energy, trapping phenomena due to electron-polaron interactions (polaronic effects) and electron-phonon interactions are the main mechanisms of electron energy loss. For the case of electron-phonon interaction, even phonon annihilations and the corresponding energy gains should be taken into account. Actually the energy gains are often neglected, for their probability of occurence is very small: much smaller, in any case, than the probability of phonon creation.

Summarizing, incident electrons are scattered and lose energy, due to the interactions with the atoms of the specimen, so that the incident electrons direction and kinetic energy are changed. It is usual to describe the collision events assuming that they belong to three distinct kinds: elastic (scattering with atomic nuclei), quasi-elasic (scattering with phonons) and inelastic (scattering with the atomic electrons and trapping due to polaronic effect).

2.1.1 Electron energy-loss peaks

Electron energy-loss spectroscopy treats the primary process in which the incident electron loses amounts of energy which characterize the target material (see, for example, Refs. [17, 20, 3, 21, 22, 23, 24, 25, 26, 27, 28, 29, 30,

31, 32, 33, 10, 9, 34, 35, 36]). An electron spectrum represents the number of electrons as a function of the energy they have after interaction with a target. The spectrum can be represented either as a function of the electron energy or of the energy-loss. In this second case, the first peak, centered at zero energy-loss, is known as the *zero-loss peak*. Also known as the *elastic peak*, it collects all the electrons which were transmitted – in transmission EELS (TEELS) – or backscattered – in reflection EELS (REELS) – without any measurable energy loss: it includes both the electrons which did not suffer any energy loss and those which were transmitted (TEELS) or backscattered (REELS) after one or more quasi-elastic collisions with phonons (for which the energy transferred is so small that, with conventional spectrometers, it cannot be experimentally resolved). In TEELS, elastic peak includes also all the electrons which were not scattered at all, namely which were not deflected during their travel inside the target and did not lose energy.

In the first 30-40 eV from the elastic peak a generally quite broad peak collects all the electrons which suffered inelastic interaction with the outer-shell atomic electrons. Typically it includes electrons which suffered energy loss for inelastic interaction with plasmons (*plasmon-losses*) and corresponding to inter-band and intra-band transitions. If the sample is sufficiently thick (in TEELS) and in the case of bulk targets (in REELS), the probability that an electron, before emerging from the specimen, has suffered more than one inelastic collision with plasmons is not negligible: such a multiple electron-plasmon inelastic collisions are represented in the spectrum by the presence of a set of equidistant peaks (the distance from each other being given by the plasma energy). The relative intensities of these multiple inelastic scattering peaks is decreasing as the energy loss increases, demonstrating that the probability of suffering one inelastic collision is greater than the probability of suffering two inelastic collisions, which is in turn higher than the probability of suffering three inelastic collisions, and so on. Of course, in transmission EELS, the number of measurable plural scattering peaks is also a function of the thickness of the sample. Plural scattering peaks at multiples of the plasma energy are clearly observable – in the energy-loss region between the elastic peak and approximately 100-200 eV (i.e., in the energy spectrum, between 100-200 eV and the elastic peak) – when the film thickness is much higher than the electron inelastic mean free path. On the other hand, when the film thickness is much smaller that the electron inelastic mean free path, a strong elastic peak and only the first plasmon-loss peak are observed in the energy-loss region below 100-200 eV (i.e., above

100-200 eV from the elastic peak, in the energy spectrum).

For higher energy-losses, edges (of relatively low intensity with respect to the plasmon-losses), corresponding to inner-shell atomic electron excitations, can be observed in the spectrum. These edges are followed by slow falls, as the energy-loss increases. The energy position of these steps or, better, sharp rises, corresponds to the ionization threshold. The energy-loss of each edge is an approximate measure of the binding energy of the inner-shell energy level involved in the inelastic scattering process.

With an energy resolution better than 2 eV, it is possible to observe, in both the low-loss peaks and in the ionization threshold edges, detailed features related to the band structure of the target and its crystalline characteristics. For example, in carbon, plasmon peaks can be found at different energies in the spectrum, according to the carbon structure. This is due to the different valence-electron densities of diamonds, graphite and amorphous carbon.

For an excellent review about electron energy-loss spectra, see the Egerton book [10].

2.1.2 Secondary electron peak

Secondary electrons – produced by a cascade process – are those electrons extracted from the atoms by inelastic electron-electron collisions. Actually not all the secondary electrons generated in the solid emerge form the target. In order to emerge from the surface, the secondary electrons generated in the solid must reach the surface and satisfy given angular and energetic conditions. Of course, only the secondary electrons which are able to emerge from the target are included in the spectrum. Their energy distribution presents a pronounced peak in the region of the spectrum below 50 eV. The secondary electron emission yield is conventionally measured integrating the area of the spectrum from 0 to 50 eV (including, in such a way, also the tail of backscattered electron whose number, on the other hand, in this energy region is negligible – unless the primary energy be very low as well).

2.2 Characterization of materials

Simulation of transport of electrons in materials has been demonstrated to be very important for many applications. The determination of electron

emission from solids irradiated by a particle beam is of crucial importance, especially in connection with the analytical techniques that utilize electrons to investigate chemical and compositional properties of solids in the near surface layers.

Electron spectroscopies and microscopies, examining how electrons interact with matter, represent fundamental tools to investigate electronic and optical properties of matter. The electron spectroscopies and microscopies allow to study the chemical composition, the electronic properties, and the crystalline structure of materials. According to the energy of the incident electrons, a broad range of spectroscopic techniques can be utilized: for example, Low Energy Electron Diffraction allows to investigate the crystalline structure of surfaces, Auger Electron Spectroscopy permits to analyze the chemical composition of the surfaces of solids, Electron Energy Loss Spectroscopy – both in transmission, when the spectrometer is combined with Transmission Electron Microscope, and in reflection – can be used to characterize materials by comparing the shape of the plasmon-loss peaks and the fine-structure features due to interband and intraband transitions with those of suitable standards.

The study of the properties of a material using electron probes requires the knowledge of the physical processes corresponding to the interaction of the electrons with the particular material under investigation. A typical AES peak of an atomic spectrum, for example, has a width in the range from 0.1 to 1.0 eV. On the other hand, in a solid, many energy levels are involved which are very close in energy, so that broad peaks are typically observed in AES spectra of solids. Their features also depend on the instrumental resolution. Another important characteristic of the spectra is related to the shift in energy of the peaks due to chemical environment: indeed the core energy levels of an atom are shifted when it is a part of a solid. This property is used to characterize materials, as the shift can be determined theoretically or by comparison with suitable standards. Even the changes in spectral intensities and the appearence of secondary peaks can be used for analyzing unknown materials. Electron spectra are used for self-supported thin film local thickness measurements, multilayer surface thin film thickness evaluation, doping dose determination in semiconductors, radiation damage investigations, and so on.

The backscattering electron coefficient can be used for non-destructive evaluation of over-layer film thickness [37, 38], while the study of the energy distribution of the backscattered electrons may be utilized for materials

characterization through the study of the shape of plasmon-loss peaks [39].

Secondary electron investigation allows extraction of critical dimensions by modeling the physics of secondary electron image formation [40, 41, 42]. It permits to investigate doping contrast in p-n junctions and to evaluate accurate nanometrology for the most advanced CMOS processes [43, 44].

2.3 Concluding remarks about electron transport

Transport Monte Carlo simulation is a very useful mathematical tool for describing many important processes relative to the interaction of electron beams with solid targets. In particular, the backscattered and secondary electron emission from solid materials can be investigated with the use of the Monte Carlo method. Many applications of the Monte Carlo study of backscattered and secondary electrons concern material analysis and characterization.

We shall present, in particular, the application of our MC simulations to non-destructive evaluation of over-layer film thickness [37, 38], materials characterization through the study of the shape of plasmon-loss peaks [39], extraction of critical dimensions by modeling the physics of secondary electron image formation [40, 41, 42] and doping contrast in p-n junctions for the evaluatation of accurate nanometrology for the most advanced CMOS processes [43, 44].

Chapter 3

Cross-sections: basic aspects

In the electron microscopies and spectroscopies, electrons penetrate into a material experiencing many different scattering processes. For a realistic description of the electron emission, it is necessary to know all the scattering mechanisms involved.

This chapter is devoted to the introduction of the concepts of cross-section and stopping power. For an excellent review of the topics treated in this chapter, also see Ref. [8]. The chosen approach is deliberately elementary, since the focus is on the basic aspects of the penetration theory. Specific details will be provided in the next chapter.

From the macroscopic point of view, the *cross-section* represents the area of a target that can be hit by a projectile, so that it depends on the geometrical properties of both the target and the projectile. Let us consider, for example, a point bullet impinging on a spherical target whose radius is r. The cross-section σ of the target is, in such a case, simply given by $\sigma = \pi r^2$.

In the microscopic world the concept has to be generalized in order to take into account that the cross-section does not only depend on the projectile and on the target, but also on their relative velocity and on the physical phenonomena we are interested in: examples are represented by the *elastic scattering cross-section* and the *inelastic scattering cross-section* of electrons (projectiles) impinging on atoms (targets). The elastic scattering cross-section describes the interactions in which the kinetic energy of the incident particle (the electron) does not change and is as a consequence the same before and after the interaction. The inelastic scattering cross-section, on the other hand, describes the collisions corresponding to an energy transfer from the incident particle (the electron) to the target (the atom): as a

consequence the kinetic energy of the incident electron decreases due to the interaction, so that the electron slows down. As the cross-section is a function of the kinetic energy of the incident electron, after every inelastic collision the cross-sections (both elastic and inelastic) of the subsequent collision, if any, will be accordingly changed.

In real experiments, the investigators cannot measure the cross-section corresponding to a single electron which hits a single atom. The typical experiment consists, instead, in the collision of a great number of electrons, called the *beam*, with a medium constituted by a configuration of many atoms and/or molecules (a gas, for example, or an amorphous or crystalline solid). The electrons constituting the beam have, in principle, all the same initial energy (the primary energy) and do not interact with each other but only with the atoms of the medium. Actually, in practical cases, the energies of the electrons constituting the primary beam are distributed around the primary energy which has to be considered, as a consequence, their mean energy. Furthermore the electrons of the beam do not interact only with the target atoms (or molecules) but with each other as well. Neglecting these interactions corresponds to investigate the so-called *low current beam approximation* [8].

3.1 Cross-section and probability of scattering

Let us indicate with σ the cross-section of the physical effect we are interested in describing, and with J the density current, i.e., the number of electrons per unit area and per unit time in the beam. Let us indicate, furthermore, with N the number of target atoms per unit volume in the target and with S the area of the target where the beam is spread. Let us assume that the beam spreading is homogeneous. If z is the depth where the collisions occur, then the volume where the electrons interact with the stopping medium is given by zS and, as a consequence, the number of collisions per unit time can be calculated by $NzSJ\ \sigma$. As the product of S by J is the number of electrons per unit time, the quantity

$$P\ =\ Nz\sigma \tag{3.1}$$

represents the mean number of collisions per electron. In the hypothesis that the target thickness z is very small (thin layers) or the density of the target atoms N is very small (gas targets), so that $P \ll 1$, P represents the probability that an electron suffers a collision while travelling in the medium.

In order to take into account that in the great majority of the experiments the projectile undergoes many collisions, let us associate to the trajectory of each particle a cylindrical volume $V = z\sigma$ and calculate the probability P_ν to hit ν target particles in this volume. If the positions of any two targets particle are not correlated like in the case, for example, of an ideal gas, such a probability is given by the Poisson distribution

$$P_\nu \;=\; \frac{(NV)^\nu}{\nu!}\;\exp(-NV) \;=\; \frac{(Nz\sigma)^\nu}{\nu!}\;\exp(-Nz\sigma)\;, \tag{3.2}$$

where $\nu \;=\; 0, 1, 2, 3, ...$

Let us firstly consider the single collision problem, $\nu \;=\; 1$. The probability of hiting precisely one particle in the volume $z\sigma$ is given by

$$P_1 \;=\; P_{(\nu=1)} \;=\; (Nz\sigma)\;\exp(-Nz\sigma)\;, \tag{3.3}$$

so that, in the limit $Nz\sigma \ll 1$,

$$P_1 \;\cong\; P \;=\; Nz\sigma\;, \tag{3.4}$$

which is the same result deduced above.

Also notice that, in the same limit, the probability for no collision at all is given by $1 - P \;=\; 1 - Nz\sigma$. This is the first order in $Nz\sigma$ of the well known Lambert and Beer's absorption law:

$$P_0 \;=\; P_{(\nu=0)} \;=\; \exp(-Nz\sigma)\;. \tag{3.5}$$

Note that, to the first order in $Nz\sigma$, the probability for double events is equal to zero.

As it is well known, one of the characteristics of the Poisson distribution is that its expected value and variance are identical. In particular, the average value $\langle\nu\rangle$ and the variance $\langle(\nu - \langle\nu\rangle)^2\rangle$, are given by

$$\langle \nu \rangle \;=\; \langle (\nu - \langle \nu \rangle)^2 \rangle \;=\; N z \sigma \;, \tag{3.6}$$

so that the relative fluctuation goes to zero as the reciprocal of the square root of $\langle \nu \rangle \;=\; N z \sigma$:

$$\sqrt{\frac{\langle (\nu - \langle \nu \rangle)^2 \rangle}{\langle \nu \rangle^2}} \;=\; \frac{1}{\sqrt{\nu}} \;. \tag{3.7}$$

3.2 Stopping power and inelastic mean free path

Let us now consider the collisions with the stopping medium resulting in a kinetic energy transfer from the projectile to the target atoms and/or molecules constituting the target. Let us assume that the energy transfers T_i ($i \;=\; 1, 2, ...$) are small with respect to the incident particle kinetic energy E. Let us also assume that ν_i be the number of events corresponding to the energy loss T_i, so that the total energy ΔE lost by an incident particle passing through a thin film of thickness Δz is given by $\sum_i \nu_i T_i$.

As the mean number of collisions of type i, according to Eq. (3.6), is given by $\langle \nu_i \rangle \;=\; N \Delta z \sigma_i$, where σ_i is the energy-loss cross-section, the energy loss is given by

$$\langle \Delta E \rangle \;=\; N \Delta z \sum_i T_i \sigma_i \;. \tag{3.8}$$

The *stopping power* is defined as

$$\frac{\langle \Delta E \rangle}{\Delta z} \;=\; N \sum_i T_i \sigma_i \;, \tag{3.9}$$

and the *stopping cross-section* S is given by

$$S \;=\; \sum_i \; T_i \; \sigma_i \;, \tag{3.10}$$

so that

$$\frac{\langle \Delta E \rangle}{\Delta z} \;=\; NS \;. \tag{3.11}$$

If the spectrum of the energy loss in continuous, instead of discrete, the *stopping cross-section* assumes the form

$$S \;=\; \int \; T \; \frac{d\sigma_{\rm inel}}{dT} \; dT \;, \tag{3.12}$$

while the *total inelastic scattering cross-section* $\sigma_{\rm inel}$ is given by

$$\sigma_{\rm inel} \;=\; \int \; \frac{d\sigma_{\rm inel}}{dT} \; dT \;, \tag{3.13}$$

and $d\sigma_{\rm inel}/dT$ is the so-called *differential inelastic scattering cross-section*. Once the total inelastic scattering cross-section $\sigma_{\rm inel}$ is known, the *inelastic mean free path* $\lambda_{\rm inel}$ can be calculated by

$$\lambda_{\rm inel} \;=\; \frac{1}{N \; \sigma_{\rm inel}} \;. \tag{3.14}$$

3.3 Range

While the inelastic mean free path is the average distance between two inelastic collisions, the *maximum range* is the total path length of the projectile. It can be easily estimated – using the simple way we are describing in this section – in all the cases in which the *energy straggling*, i.e., the statistical fluctuations in energy loss, can be neglected because small. Indeed, in this case, the energy of the incident particle is a decreasing function of the depth z calculated from the surface of the target, so that $E \;=\; E(z)$. As the stopping cross-section is, on the other hand, a function of the incident particle energy, $S \;=\; S(E)$, the equation (3.11) assumes the form of the following differential equation

$$\frac{dE}{dz} \;=\; -NS(E) \;, \tag{3.15}$$

where the minus sign has been introduced in order to take into account that,

as already noticed, the projectile energy $E(z)$ is a decreasing function of the depth z. Indicating with E_0 the initial energy of the projectiles (the so-called *beam primary energy*) the maximum range R can be easily obtained by the integration

$$R \;=\; \int_0^R dz \;=\; \int_{E_0}^0 dE\, \frac{dz}{dE}\;, \tag{3.16}$$

so that

$$R \;=\; \int_0^{E_0} \frac{dE}{N\, S(E)}\;. \tag{3.17}$$

3.4 Energy straggling

Actually the range calculated in such a way can be different from the real one because of the statistical fluctuations of the energy loss. The consequences of such a phenomenon, known as energy straggling, can be evaluated following a procedure similar to that used for introducing the stopping cross-section.

Let us firstly consider then, as before, the discrete case and calculate the variance Ω^2, or mean square fluctuation, in the energy loss ΔE, given by

$$\Omega^2 \;=\; \langle (\Delta E \;-\; \langle \Delta E \rangle)^2 \rangle\;. \tag{3.18}$$

Since

$$\Delta E \;-\; \langle \Delta E \rangle \;=\; \sum_i \left(\nu_i - \langle \nu_i \rangle\right) T_i\;, \tag{3.19}$$

we have, due to the statistical independence of the collisions and the properties of the Poisson distribution,

$$\Omega^2 \;=\; \sum_i \langle (\nu_i - \langle \nu_i \rangle)^2 \rangle\; T_i^2 \;=\; \sum_i \langle n_i \rangle\; T_i^2\;. \tag{3.20}$$

As a consequence, taking into account that $\langle n_i \rangle \;=\; N \Delta z \sigma_i$, the energy straggling can be expressed as

$$\Omega^2 \;=\; N\, \Delta z \sum_i T_i^2\, \sigma_i \;=\; N\, \Delta z\, W \tag{3.21}$$

where we have introduced the straggling parameter defined as

$$W \;=\; \sum_i \; T_i^2 \; \sigma_i \; . \tag{3.22}$$

If the spectrum of the energy loss is continuous, instead of discrete, the straggling parameter assumes the form

$$W \;=\; \int \; T^2 \; \frac{d\sigma_{\rm inel}}{dT} \; dT \; . \tag{3.23}$$

3.5 Concluding remarks about cross-sections

In this introductory chapter, the elementary theory of electron penetration in solid targets has been briefly described [8]. We have discussed the fundamental concepts of cross-section, stopping power, maximum range of penetration, and energy straggling. Details of specific applications and calculations of the scattering mechanisms along with the main theoretical approaches, which describe the cross-sections relative to the interaction of the incident electrons with atomic nuclei, atomic electrons, plasmons, phonons, and polarons, will be the subject of the next chapter.

Chapter 4

Scattering mechanisms

This chapter is devoted to the main mechanisms of scattering (elastic, quasi-elastic, and inelastic) which are relevant for the description of the interaction of electron beams with solid targets.

We shall firstly describe the elastic scattering cross-section, comparing the screened Rutherford formula to the more accurate Mott cross-section [16]. The Mott theory is based on the relativistic partial wave expansion method and the numerical solution of the Dirac equation in a central field. We shall show that the Mott cross-section is in better agreement with the available experimental data.

Then we shall briefly describe the Fröhlich theory as well [18], which describes the quasi-elastic events occurring when electron energy is very low and the probability of electron-phonon interaction becomes significant. We shall discuss energy loss and energy gain due to electron phonon-interactions, and see that electron energy gains can be safely neglected, while electron energy losses are fractions of eV.

The Bethe stopping power [45] and semi-empiric approaches [46, 47] will be presented, along with the limits of these models for the calculation of energy losses.

The Ritchie dielectric theory [17] will be then considered, which is used for the accurate calculation of electron energy losses due to electron-plasmon interaction.

Polaronic effect will be also mentioned, as it is an important mechanism for trapping very slow electrons in insulating materials [19].

In the end of the chapter, a discussion about the inelastic mean free path will be provided which takes into account all the inelastic scattering

mechanisms introduced in this chapter.

Many details about the most important theoretical models presented in this chapter can be found in the relative Appendices.

4.1 Elastic scattering

Electron-atom elastic scattering is the main responsible for the angle deflection of electrons traveling in solid targets. For some excellent reviews about the subject of elastic scattering see, for example, Refs. [8, 10, 9, 48].

Elastic scattering is not only the cause of the electron deflection: it has to be taken into account also for electron energy-loss problems, for it contributes in changing the angular distribution of the inelastically scattered electrons [10, 9].

Since a nucleus is much more massive that an electron, the energy transfer is usually negligible in an electron-nucleus collision. The great majority of elastic collisions correspond to the interaction of the incident electrons with the electrostatic nuclear field in regions which are far from the center of mass of the nucleus where, due to both the inverse square law and the shielding of the nucleus by the atomic electrons, the potential is relatively weak. For this reason, many electrons are elastically scattered through small angles.

Conservation of energy and momentum requires small transfers of energy between the electrons and the nuclei which depends on the angle of scattering. Even if the electron energy transfers are very small fraction of eV, in many circumstances they cannot be neglected. Furthermore notice that, despite to this general rule, in a few cases significant energy transfers are possible. Indeed, even if electron energy-losses are typically very small and often ignorable in electron-nucleus collisions, for the very rare cases of head-on collisions, where the scattering angle is equal to 180 °, the energy transfer can be, for the case of light elements, higher than the displacement energy, namely the energy necessary to displace the atom from its lattice position. In these cases, displacement damage and/or atom removal (sputtering) can be observed [10, 9].

The differential elastic scattering cross-section represents the probability per unit solid angle that an electron be elastically scattered by an atom, and is given by the square modulus of the complex scattering amplitude f, which is a function of the scattering angle ϑ, of the incident electron energy E_0, and of the (mean) atomic number Z of the target. The angular

distribution, once taken into account that the Coulomb potential is screened by the atomic electrons, can be calculated either by the use of the first Born approximation (screened Rutherford cross-section) or, to get more accurate results – in particular for low-energy electrons –, by solving the Schrödinger equation in a central field (partial wave expansion method, PWEM).

Typically, for the case of the screened Rutherford formula obtained within the first Born approximation, the screening of atomic electrons is treated using the Wentzel formula [49], which corresponds to a Yukawa exponential attenuation of the nuclear potential as a function of the distance from the center of mass of the nucleus. The more accurate partial wave expansion method requires a better description of the screening, so that Dirac-Hartree-Fock-Slater methods are generally used for calculating the screened nuclear potential in this case.

A further improved approach to get a very accurate calculation of the differential elastic scattering cross-section, valid also for relativistic electrons, is represented by the so-called relativistic partial wave expansion method (RPWEM), – which is based on the solution of the Dirac equation in a central field (Mott cross-section) – where the sum of the squares of the moduli of two complex scattering amplitudes f and g is required for the calculation of the elastic scattering probabilities [16]. Also in this case, Dirac-Hartree-Fock-Slater methods are utilized to calculate the shielded nuclear potential.

4.1.1 Mott cross-section vs. screened Rutherford cross-section

The relativistic partial wave expansion method (Mott theory) [16] permits to calculate the differential elastic scattering cross-section as follows:

$$\frac{d\sigma_{\mathrm{el}}}{d\Omega} = \mid f \mid^2 + \mid g \mid^2 , \tag{4.1}$$

where $f(\vartheta)$ and $g(\vartheta)$ are the scattering amplitudes (direct and spin-flip, respectively). For details about the Mott theory, see appendix A [34, 35, 36].

Once calculated the differential elastic scattering cross-section, the total elastic scattering cross-section σ_{el} and the first transport elastic scattering cross-section σ_{tr} can be computed using the following equations:

$$\sigma_{\mathrm{el}} = \int \frac{d\sigma_{\mathrm{el}}}{d\Omega}\, d\Omega , \tag{4.2}$$

$$\sigma_{\rm tr} \;=\; \int (1-\cos\vartheta)\,\frac{d\sigma_{\rm el}}{d\Omega}\,d\Omega\;, \tag{4.3}$$

It can be interesting to investigate the high energy and low atomic number limits of the Mott theory (corresponding to the first Born approximation). Along with the assumption that the atomic potential can be written according to the Wentzel recipe [49]:

$$V(r) \;=\; \frac{Z\,e^2}{r}\;\exp\left(-\frac{r}{a}\right)\;, \tag{4.4}$$

where r is the distance between the incident electron and the nucleus, Z the target atomic number, e the electron charge, and a approximately represents the screening of the nucleus by the orbital electrons, given by

$$a \;=\; \frac{a_0}{Z^{1/3}}\;, \tag{4.5}$$

where a_0 is the Bohr radius, the first Born approximation permits to write the differential elastic scattering cross-section in an analytic closed form. It is the so-called screened Rutherford cross-section:

$$\frac{d\sigma_{\rm el}}{d\Omega} \;=\; \frac{Z^2e^4}{4E^2}\;\frac{1}{(1\;-\;\cos\theta\;+\;\alpha)^2}\;, \tag{4.6}$$

$$\alpha \;=\; \frac{me^4\pi^2}{h^2}\frac{Z^{2/3}}{E} \tag{4.7}$$

In these equations, m is the electron mass and h is the Planck constant.

Even if not able to describe all the features corresponding to the elastic scattering as a function of the scattering angle that one can observe when incident electron kinetic energies are lower than ∼5-10 keV and the target atomic number is relatively high, the screened Rutherford formula has been largely used. In Figs. 4.1, 4.2, 4.3 and 4.4 the differential elastic scattering cross-section $d\sigma_{\rm el}/d\Omega$ (DESCS) – calculated with both the Mott and the

Rutherford theories – are compared. The presented data concern two different elements (Cu and Au) and energies (1000 eV and 3000 eV). It is quite clear by the comparison that the Rutherford theory approaches the Mott theory as the atomic number decreases and the primary energy increases. Indeed, the Rutherford formula can be deduced assuming the first Born approximation, which is valid when

$$E \gg \frac{e^2}{2a_0} Z^2 \, . \tag{4.8}$$

In other words, higher the electron energy – in comparison with the atomic potential – higher the accuracy of the Rutherford theory (see, in particular, Fig. 4.3). Anyway, the Rutherford formula represents a decreasing function of the scattering angle, so that it should not be surprising that it cannot describe the features which emerges as the electron energy is low and atomic number is high (see, in particular, Fig. 4.2).

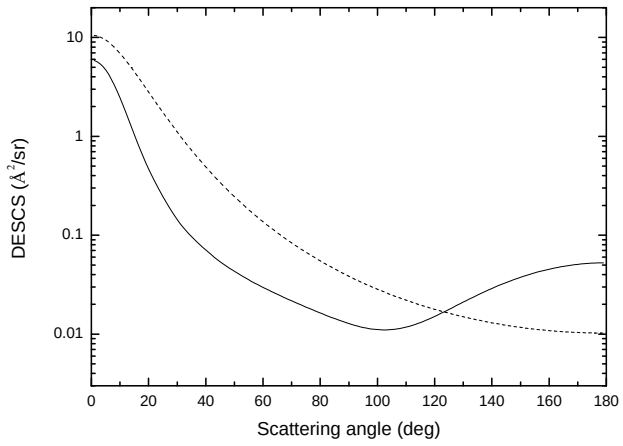

Figure 4.1: Present calculation of the differential elastic scattering cross-section of 1000 eV electrons scattered by Cu as a function of the scattering angle. Solid line: Relativistic partial wave expansion method (Mott theory). Dashed line: Screened Rutherford formula, Eq. (4.6).

In Monte Carlo simulations, when electron primary energy is higher than 10 keV, Rutherford cross-section is sometimes used – instead of the more

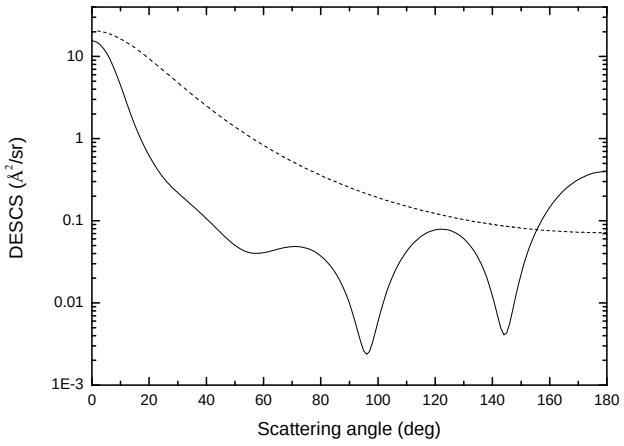

Figure 4.2: Present calculation of the differential elastic scattering cross-section of 1000 eV electrons scattered by Au as a function of the scattering angle. Solid line: Relativistic partial wave expansion method (Mott theory). Dashed line: Screened Rutherford formula, Eq. (4.6).

accurate Mott cross-section – mainly because it provides a very simple analytic way to calculate both the cumulative probability of elastic scattering into an angular range from 0 to θ, $P_{\rm el}(\theta, E)$, and the elastic scattering mean free path, $\lambda_{\rm el}$. Even if not used in this work, where numerical calculations of Mott cross-section will always be utilized, it can be useful to see how $P_{\rm el}(\theta, E)$ and $\lambda_{\rm el}$ can be calculated in a completely analytic way taking advantage of the particular form of the screened Rutherford formula. In the first Born approximation these quantities are in fact given, respectively, by

$$P_{\rm el}(\theta, E) \;=\; \frac{(1 \;+\; \alpha/2)\;(1 \;-\; \cos\theta)}{1 \;+\; \alpha \;-\; \cos\theta}\;, \tag{4.9}$$

$$\lambda_{\rm el} \;=\; \frac{\alpha\;(2 \;+\; \alpha)\;E^2}{N\;\pi\;e^4\;Z^2}\;, \tag{4.10}$$

where N is the number of atoms per unit volume.

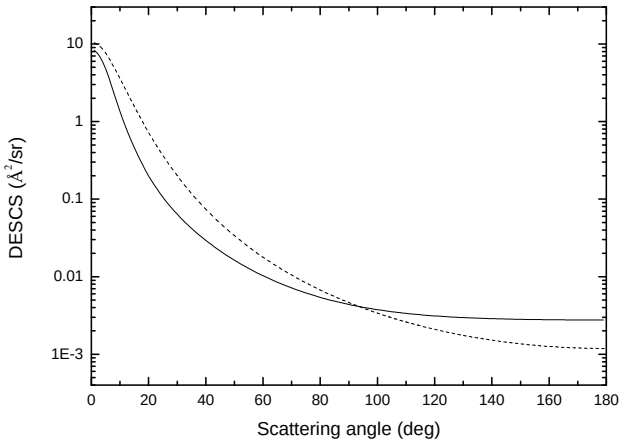

Figure 4.3: Present calculation of the differential elastic scattering cross-section of 3000 eV electrons scattered by Cu as a function of the scattering angle. Solid line: Relativistic partial wave expansion method (Mott theory). Dashed line: Screened Rutherford formula, Eq. (4.6).

The demonstration of these equations is quite easy. Indeed

$$P_{\rm el}(\theta, E) \;=\; \frac{e^4 Z^2}{4\sigma_{\rm el} E^2} \int_0^{\theta} \frac{2\pi \sin\vartheta \; d\vartheta}{(1 \;-\; \cos\vartheta \;+\; \alpha)^2} \;=\; \frac{\pi e^4 Z^2}{2\sigma_{\rm el} E^2} \int_{\alpha}^{1-\cos\theta+\alpha} \frac{du}{u^2} \;,$$

where

$$\sigma_{\rm el} \;=\; \frac{e^4 Z^2}{4E^2} \int_0^{\pi} \frac{2\pi \sin\vartheta \; d\vartheta}{(1 \;-\; \cos\vartheta \;+\; \alpha)^2} \;=\; \frac{\pi e^4 Z^2}{2E^2} \int_{\alpha}^{2+\alpha} \frac{du}{u^2} \;.$$

Since

$$\int_{\alpha}^{1-\cos\theta+\alpha} \frac{du}{u^2} \;=\; \frac{1-\cos\theta}{\alpha(1-\cos\theta+\alpha)}$$

and

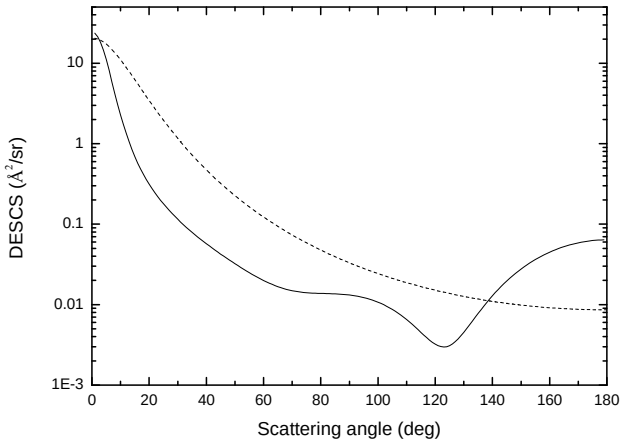

Figure 4.4: Present calculation of the differential elastic scattering cross-section of 3000 eV electrons scattered by Au as a function of the scattering angle. Solid line: Relativistic partial wave expansion method (Mott theory). Dashed line: Screened Rutherford formula, Eq. (4.6).

$$\int_{\alpha}^{2+\alpha} \frac{du}{u^2} \;=\; \frac{1}{\alpha(1+\alpha/2)} \;,$$

Eqs. (4.9) and (4.10) immediately follow.

Note that from the cumulative probability expressed by Eq. (4.9) it follows that the scattering angle can be easily calculated from:

$$\cos\theta \;=\; 1 \;-\; \frac{2\alpha \; P_{\rm el}(\theta, E)}{2 \;+\; \alpha \;-\; 2P_{\rm el}(\theta, E)} \;. \tag{4.11}$$

Due to the excellent agreement between experimental data and Mott cross-section (see, for a comparison, Fig. 4.5), the most recent Monte Carlo codes (and also all the calculations presented in this work) use the Mott cross-section to describe the differential elastic scattering cross-section – and the cumulative probability necessary for sampling the scattering angle. Nevertheless, it is worth noticing that excellent results can also be obtained using

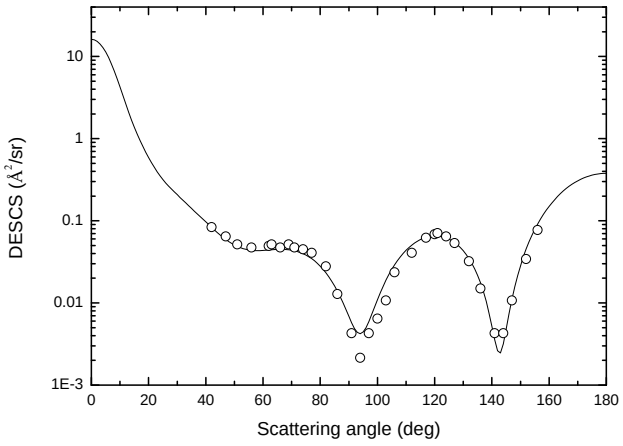

Figure 4.5: Present calculation of the differential elastic scattering cross-section of 1100 eV electrons scattered by Au as a function of the scattering angle. Solid line: Relativistic partial wave expansion method (Mott theory). Circles: Reichert experimental data [50].

the simple screened Rutherford formula, Eq. (4.6), provided that the kinetic primary energy of the incident electrons is higher than 10 keV.

4.2 Quasi-elastic scattering

Due to thermal excitations, atoms in crystalline structures vibrate around their equilibrium lattice sites. These vibrations are known as *phonons*. A mechanism of energy loss (and energy gain as well) is represented by the interaction of the electrons with the optical modes of the lattice vibrations. These transfers of small amounts of energy among electrons and lattice vibrations are due to quasi-elastic processes known as *phonon creation* (electron energy-loss) and *phonon annihilation* (electron energy-gain) [18, 51]. Phonon energies do not exceed $k_{\mathrm{B}}T_{\mathrm{D}}$, where k_{B} is the Boltzmann constant and T_{D} is the Debye temperature. As $k_{\mathrm{B}}T_{\mathrm{D}}$ typically is not greater than 0.1 eV, the energy losses and gains due to electron-phonon interaction are usually smaller than 0.1 eV, so that they are generally not resolved by conventional spectrometers [10]. These mechanisms of electron energy loss – and, with

much smaller probability, energy gain – are particularly relevant when the electron energy is low (few eV) [19].

4.2.1 Electron-phonon interaction

According to Fröhlich [18] and Llacer and Garwin [51], the inverse mean free path for electron energy loss due to phonon creation can be written as

$$\lambda_{\text{phonon}}^{-1} \;=\; \frac{1}{a_0}\;\frac{\varepsilon_0 \;-\; \varepsilon_\infty}{\varepsilon_0\;\;\varepsilon_\infty}\;\frac{\hbar\omega}{E}\;\frac{n(T)\;+\;1}{2}\;\ln\left[\frac{1\;+\;\sqrt{1\;-\;\hbar\omega/E}}{1\;-\;\sqrt{1\;-\;\hbar\omega/E}}\right]\;, \quad (4.12)$$

where E is the energy of the incident electron, $W_{\text{ph}} = \hbar\omega$ the electron energy loss (of the order of 0.1 eV), ε_0 the static dielectric constant, ε_∞ the high frequency dielectric constant, a_0 the Bohr radius and

$$n(T) \;=\; \frac{1}{e^{\hbar\omega/k_{\text{B}}T}\;-\;1} \quad (4.13)$$

the occupation number. Notice that a similar equation can be written to describe electron energy gain (corresponding to phonon annihilation). The probability of occurrence of phonon annihilation is much lower than that of phonon creation. Electron energy gain can thus be safely neglected for many practical purposes.

For further details about electron-phonon interaction and Fröhlich theory [18, 51] see Appendix B.

4.3 Inelastic scattering

Let us consider now the inelastic scattering due to the interaction of the incident electrons with the atomic electrons located around the nucleus (both the core and the valence electrons). For an excellent review about this subject, see Ref. [10].

If the incident electron energy is high enough, it can excite an *inner-shell* electron which can make a transition from its ground state to one of the unoccupied electron states above the Fermi level. Due to energy conservation, the incident electron loses an amount of energy equal to the difference between the state above the Fermi level occupied by the excited atomic electron

and its ground state; while the atom is left in an ionized state. The following de-excitation of the target atom generates an excess energy that can be liberated in one of two competitive ways: either generating an X-ray photon (Energy Dispersive Spectroscopy, EDS, is based on this process) or by the emission of another electron (Auger emission): this is the phenomenon on which Auger Electron Spectroscopy is based.

Outer-shell inelastic scattering can occur according to two alternative processes. In the first one, an outer-shell electron can suffer a single-electron excitation. A typical example is constituted by inter-band and intra-band transitions. If the atomic electron excited in such a way is able to reach the surface with an energy higher than the potential barrier between the vacuum level and the minimum of the conduction band, it can emerge from the solid as a secondary electron, the energy needed for this transition being provided by the fast incident electron. De-excitation can occur through the emission of electromagnetic radiation in the visible region – corresponding to the phenomenon known as cathode-luminescence – or through radiation-less processes generating heat. Outer-shell electrons can also be excited in collective states corresponding to the oscillation of the valence electrons denoted as plasma resonance. It is generally described as the creation of quasi-particles known as *plasmons*, with energies – characteristic of the material – that range, typically, in the interval from 5 to 30 eV. Plasmon decay generates secondary electrons and/or produces heat.

4.3.1 Stopping: Bethe-Bloch formula

In the CSDA, energy losses are calculated by utilizing the stopping power. Using a quantum mechanical treatment, Bethe [45] proposed the following formula for the stopping power:

$$-\frac{dE}{dz} = \frac{2\pi e^4 N Z}{E} \ln\left(\frac{1.166E}{I}\right) , \tag{4.14}$$

where I represents the mean ionization energy which, according to Berger and Seltzer [52], can be approximated by the following simple formula:

$$I \;=\; (9.76 \;+\; 58.8\; Z^{-1.19})\; Z\,. \tag{4.15}$$

As we have already discussed, the Bethe-Bloch formula is valid for energies

higher than $\sim I$. It approaches zero as E approaches $I/1.166$. When E becomes smaller than $I/1.166$, the stopping power predicted by the Bethe-Bloch formula becomes negative. Therefore, the low-energy stopping power requires a different approach (see the dielectric approach, below).

4.3.2 Stopping: semi-empiric formulas

The stopping power can also be described using semi-empiric expressions, such as the following;

$$-\frac{dE}{dz} = \frac{K_{\mathrm{e}} N Z^{8/9}}{E^{2/3}} \ , \tag{4.16}$$

proposed in 1972 by Kanaya and Okayama (with $K_{\mathrm{e}} = 360$ eV$^{5/3}$ Å^2) [47]. This last formula allows one to analytically evaluate the maximum range of penetration as a function of the primary energy E_0, where

$$R = \int_{E_0}^{0} \frac{dE}{dE/dz} = \frac{3E_0^{5/3}}{5K_e N Z^{8/9}} \ \propto \ E_0^{1.67}. \tag{4.17}$$

A similar empirical formula for the evaluation of the maximum range of penetration of electrons in solid targets was firstly proposed, in 1954, by Lane and Zaffarano [46] who found that their range-energy experimental data (obtained by investigating electron transmission in the energy range 0-40 keV by thin plastic and metal films) fell within 15 percent of the results obtained by the following simple formula:

$$E_0 \ = \ 22.2 R^{0.6} \ , \tag{4.18}$$

where E_0 was expressed in keV and R in mg/cm^2. As a consequence, the Kanaya and Okayama formula is consistent with the Lane and Zaffarano experimental observations, which are described as well by the relationship

$$R \propto E_0^{1.67} \, . \tag{4.19}$$

4.3.3 Dielectric theory

In order to get a very accurate description of the electron energy loss processes, of the stopping power, and of the inelastic mean free path, valid even when electron energy is low, it is necessary to consider the response of the ensemble of conduction electrons to the electromagnetic field generated by the electrons passing through the solid: this response is described by a complex dielectric function. In the Appendix C the Ritchie theory [17, 20] is described which demonstrates, in particular, that the energy loss function, $f(k,\omega)$, necessary to calculate both the stopping power and the inelastic mean free path, is the reciprocal of the imaginary part of the dielectric function

$$f(k,\omega) \;=\; \mathrm{Im}\left[\frac{1}{\varepsilon(k,\omega)}\right] \;. \tag{4.20}$$

In Eq. (4.20), $\hbar\vec{k}$ represents the momentum transferred and $\hbar\omega$ the electron energy loss.

Once known the energy loss function, the differential inverse inelastic mean free path can be calculated as [26]

$$\frac{d\lambda_{\mathrm{inel}}^{-1}}{d\hbar\omega} \;=\; \frac{1}{\pi\; E\; a_0} \int_{k_-}^{k_+} \frac{dk}{k}\; f(k,\omega)\;, \tag{4.21}$$

where

$$\hbar\; k_{\pm} \;=\; \sqrt{2\; m\; E} \;\pm\; \sqrt{2\; m\; (E \;-\; \hbar\omega)}\;, \tag{4.22}$$

E is the electron energy, m the electron mass, and a_0 the Bohr radius. The limits of integration, expressed by Eq. (4.22), come from conservation laws (see section 6.2.3).

In order to calculate the dielectric function, and hence the energy loss-function, let us consider the electric displacement $\vec{\mathcal{D}}$ [35, 36]. If $\vec{\mathcal{P}}$ is the polarization density of the material, and $\vec{\mathcal{E}}$ the electric field, then

$$\vec{\mathcal{P}} \;=\; \chi_{\varepsilon}\, \vec{\mathcal{E}}\;, \tag{4.23}$$

where

$$\chi_\varepsilon \;=\; \frac{\varepsilon \;-\; 1}{4\,\pi} \tag{4.24}$$

and

$$\vec{\mathcal{D}} \;=\; \vec{\mathcal{E}} \;+\; 4\,\pi\,\vec{\mathcal{P}} \;=\; (1 \;+\; 4\,\pi\chi_\varepsilon)\,\vec{\mathcal{E}} \;=\; \varepsilon\,\vec{\mathcal{E}}\,. \tag{4.25}$$

If n is the density of the outher-shell electrons, i.e., the number of outer-shell electrons per unit volume in the solid, and ξ the electron displacement due to the electric field, then

$$\mathcal{P} \;=\; e\,n\,\xi\,, \tag{4.26}$$

so that

$$|\vec{\mathcal{E}}| \;=\; \frac{4\,\pi\,e\,n\,\xi}{\varepsilon \;-\; 1}\,. \tag{4.27}$$

Let us consider the classical model of electrons elastically bound, with elastic constants $k_{\rm n} = m\omega_{\rm n}^2$ and subject to a frictional damping effect due to collisions, irradiations, described by a damping constant Γ. We have indicated here with m the electron mass and with $\omega_{\rm n}$ the natural frequencies. The electron displacement satisfies the equation [22]

$$m\,\ddot{\xi} \;+\; \beta\dot{\xi} \;+\; k\,\xi \;=\; e\,\mathcal{E} \tag{4.28}$$

where $\beta = m\Gamma$. Assuming that $\xi \;=\; \xi_0\;\exp(i\omega t)$, a straightforward calculation allows to conclude that

$$\varepsilon(0,\omega) \;=\; 1 \;-\; \frac{\omega_{\rm p}^2}{\omega^2 \;-\; \omega_{\rm n}^2 \;-\; i\Gamma\omega}\,, \tag{4.29}$$

where $\omega_{\rm p}$ is the *plasma frequency*, given by

$$\omega_{\rm p}^2 \;=\; \frac{4\,\pi\,n\,e^2}{m}\,. \tag{4.30}$$

Let us now consider a superimposition of free and bound oscillators. In such a case the dielectric function can be written as:

$$\varepsilon(0,\omega) \;=\; 1 \;-\; \omega_{\rm p}^2 \sum_n \frac{f_{\rm n}}{\omega^2 \;-\; \omega_{\rm n}^2 \;-\; i\Gamma_{\rm n}\omega} \;, \tag{4.31}$$

where $\Gamma_{\rm n}$ are positive frictional damping coefficients and $f_{\rm n}$ are the fractions of the valence electrons bound with energies $\hbar\omega_{\rm n}$.

The extension of the dielectric function from the optical limit (corresponding to $k = 0$) to $k > 0$ is obtained including, in the previous formula, an energy $\hbar\omega_k$ related to the dispersion relation, so that

$$\varepsilon(k,\omega) \;=\; 1 \;-\; \omega_p^2 \sum_n \frac{f_n}{\omega^2 \;-\; \omega_n^2 \;-\; \omega_k^2 \;-\; i\Gamma_n\omega} \;. \tag{4.32}$$

In the determination of the dispersion relation, one has to take into account a constraint, known as the *Bethe ridge*. According to the Bethe ridge, as $k \to \infty$, $\hbar\omega_k$ should approach $\hbar^2k^2/2m$. Of course, an obvious way to obtain this result (the simplest one, actually) is to impose that [26, 29],

$$\hbar\omega_k \;=\; \frac{\hbar^2k^2}{2m} \;. \tag{4.33}$$

Another way to satisfy the constraint represented by the Bethe ridge corresponds to the use of the following equation [17, 20]:

$$\hbar^2\,\omega_k^2 \;=\; \frac{3\,\hbar^2\,v_F^2\,k^2}{5} \;+\; \frac{\hbar^4\,k^4}{4\,m^2} \;, \tag{4.34}$$

where v_F represents the velocity of Fermi.

Once the dielectric function is known, the loss function $\mathrm{Im}\Big[\frac{1}{\varepsilon(k,\omega)}\Big]$ is given by

$$\mathrm{Im}\left[\frac{1}{\varepsilon(k,\omega)}\right] = \;-\;\frac{\varepsilon_2}{\varepsilon_1^2+\varepsilon_2^2} \;, \tag{4.35}$$

where

$$\varepsilon(k,\omega) = \varepsilon_1(k,\omega) + i\varepsilon_2(k,\omega) \ , \tag{4.36}$$

The calculation of the energy loss function can be also performed by the direct use of experimental optical data. In Figs. 4.6 and 4.7, the energy loss function of Polymethyl Methacrylate and silicon dioxide are represented, respectively. The calculation of the dielectric function from optical data can be performed by

$$\varepsilon_1(0,\omega) = \mu^2 - \nu^2 \ , \tag{4.37}$$

$$\varepsilon_2(0,\omega) = -2\mu\nu \tag{4.38}$$

where μ is the index of refraction and ν the extinction coefficient.

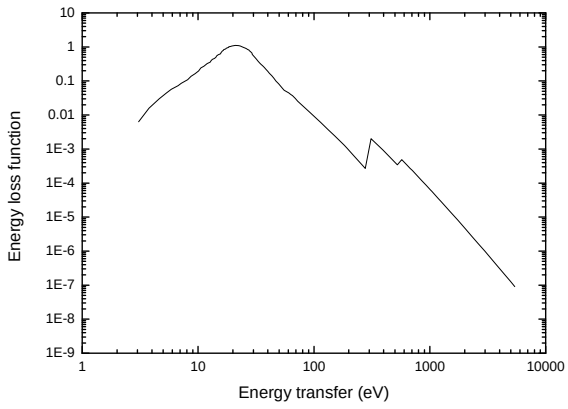

Figure 4.6: Optical energy loss function for electrons in Polymethyl Methacrylate. For energies lower than 72 eV we utilized the optical data of Ritsko *et al.* [53]. For higher energies the calculation of the optical loss function was performed using the Henke *et al.* atomic photo-absorption data [54, 55].

A quadratic extension into the energy- and momentum-transfer plane of the energy loss function through

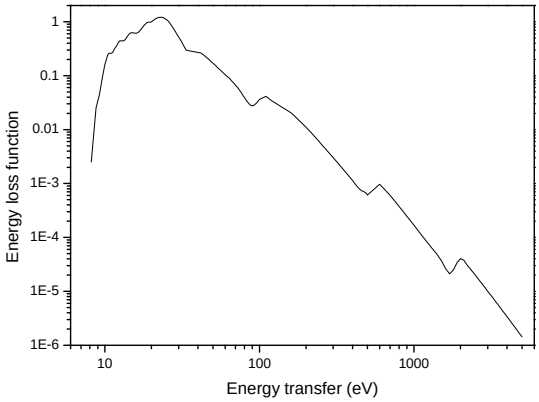

Figure 4.7: Optical energy loss function for electrons in silicon dioxide (SiO_2). For energies lower than 33.6 eV we utilized the optical data of Buechner [56]. For higher energies the calculation of the optical loss function was performed using the Henke *et al.* atomic photo-absorption data [54, 55].

$$\mathrm{Im}\left[\frac{1}{\varepsilon(k,\omega)}\right] \;=\; \int_0^{+\infty} d\omega'\;\omega'\;\mathrm{Im}\left[\frac{1}{\varepsilon(0,\omega')}\right]\;\frac{\delta[\hbar\,\omega\;-\;(\hbar\,\omega'\;+\;m\,k^2/2)]}{\omega}\;. \tag{4.39}$$

allows the extension of the dielectric function from the optical limit to $k > 0$ [24, 25].

Penn [24] and Ashley [25] calculated the energy loss function using optcal data and extending as described above [see Eq. (4.39)] the dielectric function from the optical limit to $k > 0$. According to Ashley [25], the inverse inelastic mean free path $\lambda_{\mathrm{inel}}^{-1}$ of electrons penetrating solid targets can be calculated by

$$\lambda_{\mathrm{inel}}^{-1}(E) = \frac{me^2}{2\pi\hbar^2 E}\int_0^{W_{max}} \mathrm{Im}\left[\frac{1}{\varepsilon(0,w)}\right] L\left(\frac{w}{E}\right) dw\;, \tag{4.40}$$

where E is the incident electron energy and $W_{\max} = E/2$ (as usual, we have indicated with e the electron charge and with $\hbar$ the Planck constant h divided by 2π). According to Ashley, in the dielectric function $\varepsilon(\vec{k}, w)$,

the momentum transfer $\hbar\vec{k}$ was set to 0 and the ε dependence on $\vec{k}$ was factorised through the function $L(w/E)$. Ashley [25] demonstrated that a good approximation of the function $L(x)$ is given by:

$$L(x) = (1-x)\ln\frac{4}{x} - \frac{7}{4}x + x^{3/2} - \frac{33}{32}x^2 \ . \tag{4.41}$$

The calculation of the stopping power, $-dE/dz$, can be performed by using the following equation [25]:

$$-\frac{dE}{dz} = \frac{me^2}{\pi\hbar^2 E}\int_0^{W_{\max}} \mathrm{Im}\left[\frac{1}{\varepsilon(0,w)}\right] S\left(\frac{w}{E}\right)\ w\ dw \ , \tag{4.42}$$

where

$$S(x) = \ln\frac{1.166}{x} - \frac{3}{4}x - \frac{x}{4}\ln\frac{4}{x} + \frac{1}{2}x^{3/2} - \frac{x^2}{16}\ln\frac{4}{x} - \frac{31}{48}x^2 \ . \tag{4.43}$$

In Figs. 4.8 and 4.9 the stopping power of electrons in PMMA and in SiO_2 are, respectively, shown and compared with calculations perfromed by other authors. The present calculations were obtained using the just described Ashley recipe.

The differential inverse inelastic mean free path $d\lambda_{\mathrm{inel}}^{-1}(w,E)/dw$ can be calculated using the following equation:

$$\frac{d\lambda_{\mathrm{inel}}^{-1}(w,E)}{dw} = \frac{me^2}{2\pi\hbar^2 E}\mathrm{Im}\left[\frac{1}{\varepsilon(0,w)}\right] L\left(\frac{w}{E}\right) \ . \tag{4.44}$$

Bulk and surface plasmon losses

The plasma frequency ω_{p} is given, in the Drude free electron theory, by Eq. (4.30) and represent the frequency of the volume collective excitations, which correspond to the propagation in the solid of bulk plasmons with energy

$$E_{\mathrm{p}} \ = \ \hbar\omega_{\mathrm{p}} \ . \tag{4.45}$$

In the electron energy loss spectra, it is thus expected to observe a bulk

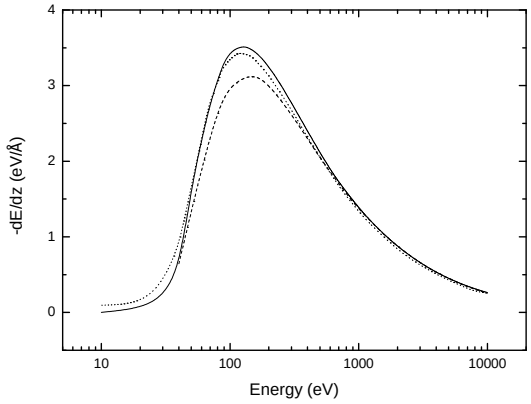

Figure 4.8: Stopping power of electrons in PMMA. Solid line represents the present calculation, obtained according to the Ashley recipe [25]. Dashed line provides the Ashley original results [25]. Dotted line describes the Tan *et al.* computational results [57]. The different optical energy loss functions utilized in the three cases explain the differences in the calculations.

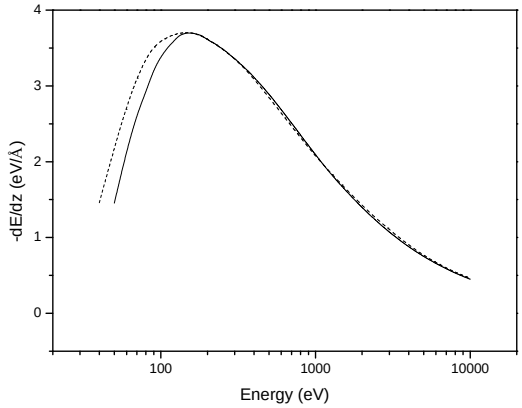

Figure 4.9: Stopping power of electrons in SiO_2. Solid line represents the present calculation, obtained according to the Ashley recipe [25]. Dashed line provides the Ashley and Anderson data [58]. The different optical energy loss functions utilized in the two cases explain the differences in the calculations.

plasmon peak whose maximum is located at an energy $E_{\rm p}$ [given by Eq. (4.45)] from the elastic or zero-loss peak.

Also features due to surface plasmon excitations appear in spectra acquired either in reflection mode from bulk targets or in transmission mode from very thin samples or small particles [59]. Indeed, in the proximity of the surface, due to the Maxwell's equation boundary conditions, surface excitations modes (surface plasmons) take place with a resonance frequency slightly lower than the bulk resonance frequency.

A rough evalution of the energy of the surface plasmons can be performed – for a free electron metal – by the following very simple considerations [10]. In general, similarly to the volume plasmons propagating inside the solid, in the presence of an interface between two different materials – which we indicate here with a and b –, longitudinal waves travel as well along the interface. From continuity considerations it follows that [10]

$$\varepsilon_{\rm a} \, + \, \varepsilon_{\rm b} \, = \, 0 \, , \tag{4.46}$$

where we have indicated with $\varepsilon_{\rm a}$ the dielectric function on the side a and with $\varepsilon_{\rm b}$ the dielectric function on the side b of the interface. Let us now consider the particular case corresponding to a vacuum/metal interface and ignore, for the sake of simplicity, the damping, so that $\Gamma \approx 0$. Then, if a represents the vacuum, we get

$$\varepsilon_{\rm a} \, = \, 1 \, , \tag{4.47}$$

and

$$\varepsilon_{\rm b} \, \approx \, 1 \, - \, \frac{\omega_{\rm p}^2}{\omega_{\rm s}^2} \, , \tag{4.48}$$

where we have indicated with $\omega_{\rm s}$ the frequency of the longitudinal waves of charge density traveling along the surface. Then we get, from Eq. (4.46)

$$1 \, = \, 1 \, - \, \frac{\omega_{\rm p}^2}{\omega_{\rm s}^2} \, .$$

As a consequence the surface plasmon energy $E_{\rm s} = \hbar\omega_{\rm s}$, i.e., the surface

plasmon peak position in the energy loss spectrum, is expected to be found at an energy

$$E_{\mathrm{s}} \;=\; \frac{E_{\mathrm{p}}}{\sqrt{2}} \tag{4.49}$$

from the position of the elastic peak.

4.3.4 Polaronic effect

A low-energy electron moving in an insulating material induces a polarization field that has a stabilizing effect on the moving electron itself. This phenomenon can be described as the generation of a quasi-particle called polaron. The polaron has a relevant effective mass and mainly consists of an electron (or a hole created in the valence band) with its polarization cloud around it. According to Ganachaud and Mokrani [19], the polaronic effect can be described assuming that the inverse inelastic mean free path that rules the phenomenon – and which is proportional to the probablity for a low-energy electron to be trapped in the ionic lattice – is given by

$$\lambda_{\mathrm{pol}}^{-1} \;=\; C\, e^{-\gamma\, E} \tag{4.50}$$

where C and γ are constants depending on the dielectric material. Thus the lower the electron energy, the higher the probability for an electron to lose its energy and to create a polaron. This approach implicitly assumes that, once generated a polaron, the residual kinetic energy of the electron is negligible. Furthermore the electron is assumed to stay trapped in the interaction site. This is quite a rough approximation, as trapped electrons – due to phonon induced processes – can actually hop from one trapping site to another. Anyway it is often a sufficiently good approximation for the Monte Carlo simulation purposes, so that it will be utilized in this work.

4.4 Inelastic Mean Free Path

We have already discussed the fact that the main mechanism which determines the inelastic scattering cross-section and the relative energy losses, for energies higher than 50 eV, is the interaction of the incident electrons with

the collective excitations of the electron sea, known as plasmons. Such energy loss mechanisms can be described by calculating the so-called energy loss function, i.e., the reciprocal of the imaginary part of the dielectric function. The Ritchie theory [17, 20] can be used – starting from the knowledge of the dependence of the dielectric function upon both the energy loss and the momentum transfer – to calculate the differential inverse electron inelastic mean free path and the electron inelastic mean free path. When the electron energy is higher than 50 eV, both the electron inelastic mean free path and the electron stopping power calculated within the dielectric formalism are in very good agreement with the experiment (and with theoretical data obtained by other investigators).

When, on the other hand, the electron energy becomes lower than 50 eV, the dielectric formalism alone is no longer able to accurately describe the energy loss phenomena. In fact, as the electron energy decreases, the electron inelastic mean free path calculated using only the electron-electron interaction increases indefinitely (see Figs. 4.10 and 4.11), while the stopping power goes quickly to zero (see Figs. 4.8 and 4.9). This means that if only electron-electron interactions were active for inelastic scattering, electrons with such a low energy would no longer interact inelastically (i.e., losing energy) with the solid. As a consequence they would travel without any change in their kinetic energy. For a semi-infinite target, this very long travel in the solid would continue forever or until the electron reaches the surface of the material and is able to emerge.

When the energy becomes lower than 20-30 eV, actually, we know that further mechanisms of energy loss becomes very important (electron-phonon and electron-polaron interactions) so that the actual inelastic mean free path approaches zero as the electron energy goes to zero (see Figs. 4.12, 4.13).

4.5 Concluding remarks about scattering

Elastic and inelastic scattering cross-sections were described in this chapter. They are the main ingredients of the Monte Carlo simulation. In particular, the elastic scattering collisions are calculated by the Mott cross section, the electron-plasmon inelastic scattering events by the Ritchie dielectric theory, and electron-phonon energy losses by the Fröhlich theory. Polaronic effects are also included in the Monte Carlo code.

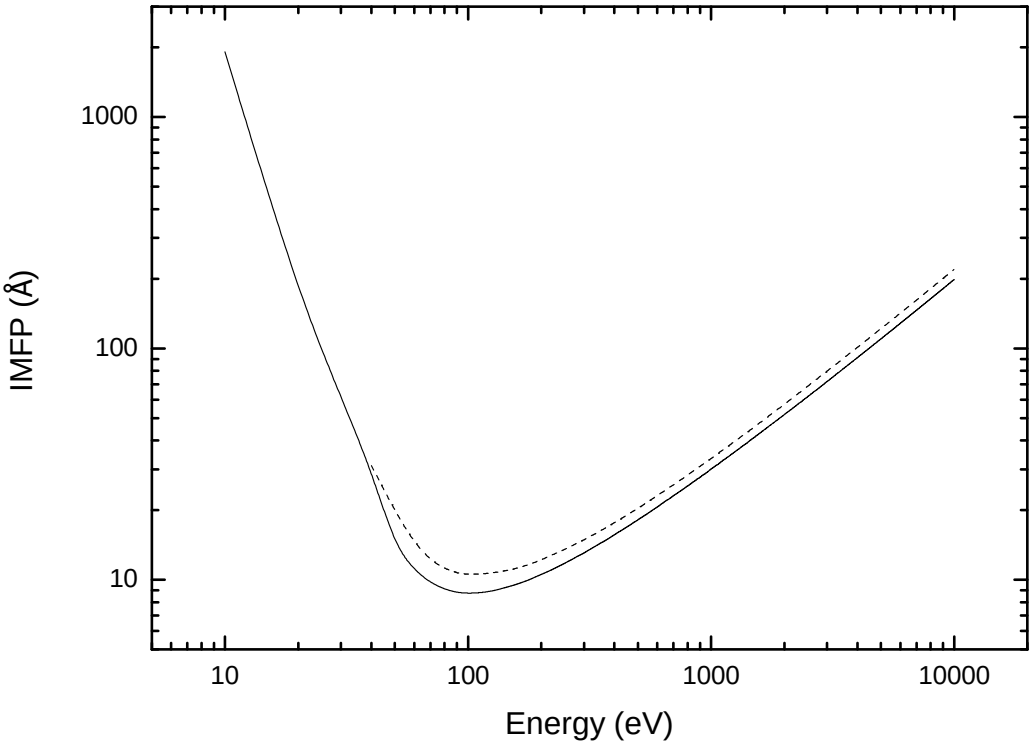

Figure 4.10: Present calculation of the inelastic mean free path of electrons in PMMA due to electron-electron interaction. Solid line represents the present calculation, based on the Ashely model [25], obtained utilizing the Ashley approach for the extension of the energy loss function out from the optical domain. Dashed line describes the original Ashley results [25].The differences in the two calculations are due to the different optical energy loss functions utilized. The present calculations have been shown even for energies lower than 50 eV in order to demonstrate that, if only electron-electron interactions were active for inelastic scattering, electrons with such a low energy would no longer interact inelastically (i.e., losing energy) with the solid.

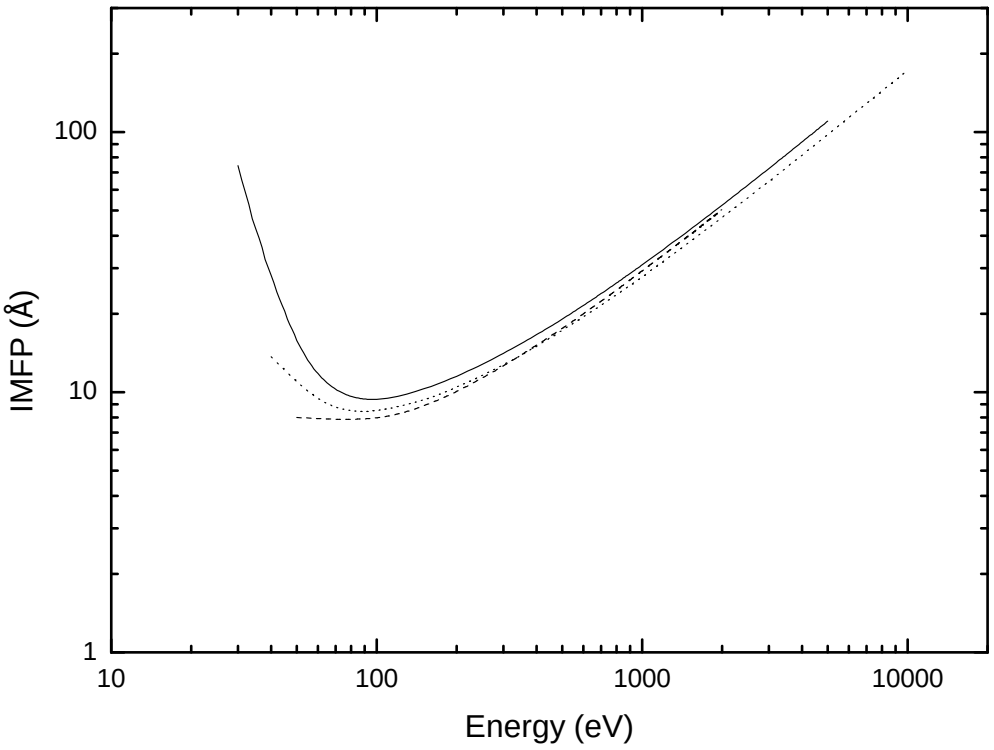

Figure 4.11: Present calculation of the inelastic mean free path of electrons in SiO_2 due to electron-electron interaction. Solid line represents the present calculation, based on the Ashely model [25], obtained utilizing the Ashley approach for the extension of the energy loss function out from the optical domain. Dashed line describes the Ashley and Anderson data [58]. Dotted line provides the Tanuma, Powell and Penn computational results [60]. The differences in the calculations are due to the different optical energy loss functions utilized.The present calculations have been shown even for energies lower than 50 eV in order to demonstrate that, if only electron-electron interactions were active for inelastic scattering, electrons with such a low energy would no longer interact inelastically (i.e., losing energy) with the solid.

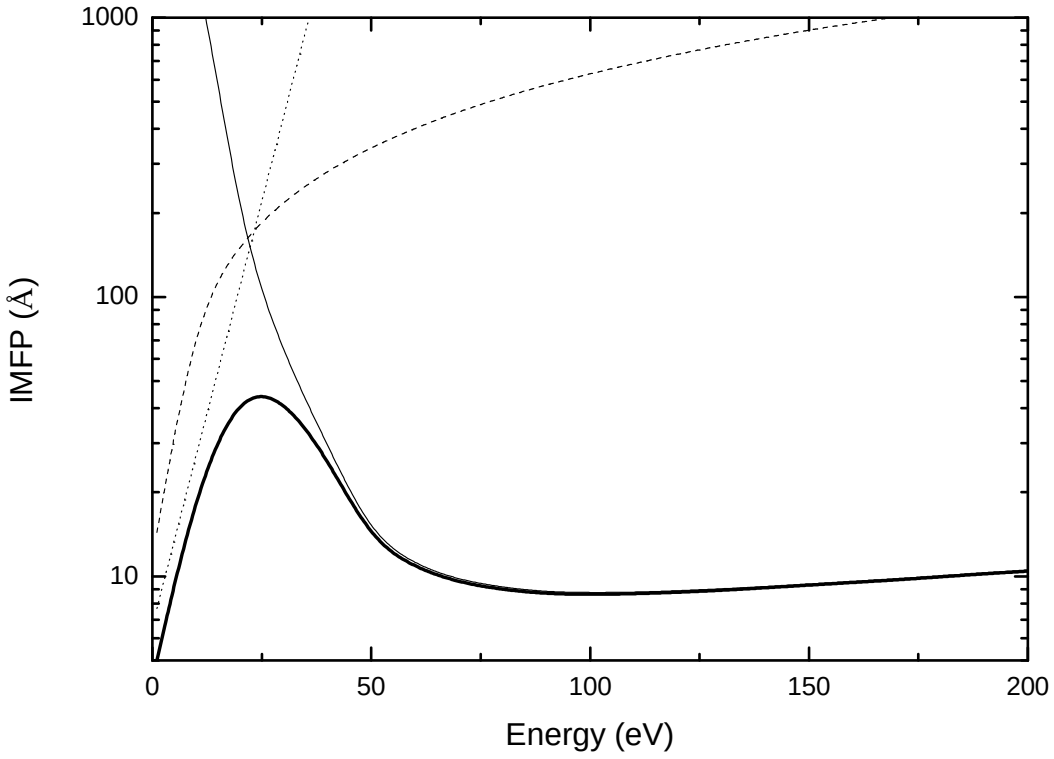

Figure 4.12: Inelastic mean free path (IMFP) of electrons in PMMA corresponding to the various mechanisms of energy loss. Electron-electron inelastic mean free path, $\lambda_{\rm inel}$, is represented by the solid line. Electron-phonon inelastic mean free path, $\lambda_{\rm phonon}$, is represented by the dashed line. Electron-polaron inelastic mean free path, $\lambda_{\rm pol}$, is represented by the dotted line. The electron inelastic mean free path $\lambda_{\rm in}$ is given by $\lambda_{\rm in}^{-1} = \lambda_{\rm inel}^{-1} + \lambda_{\rm phonon}^{-1} + \lambda_{\rm pol}^{-1}$ and is represented by the bold solid line. It approaches zero as the electron energy goes to zero. $W_{\rm ph}$=0.1 eV, C=0.15 Å^{-1}, γ=0.14 eV^{-1}.

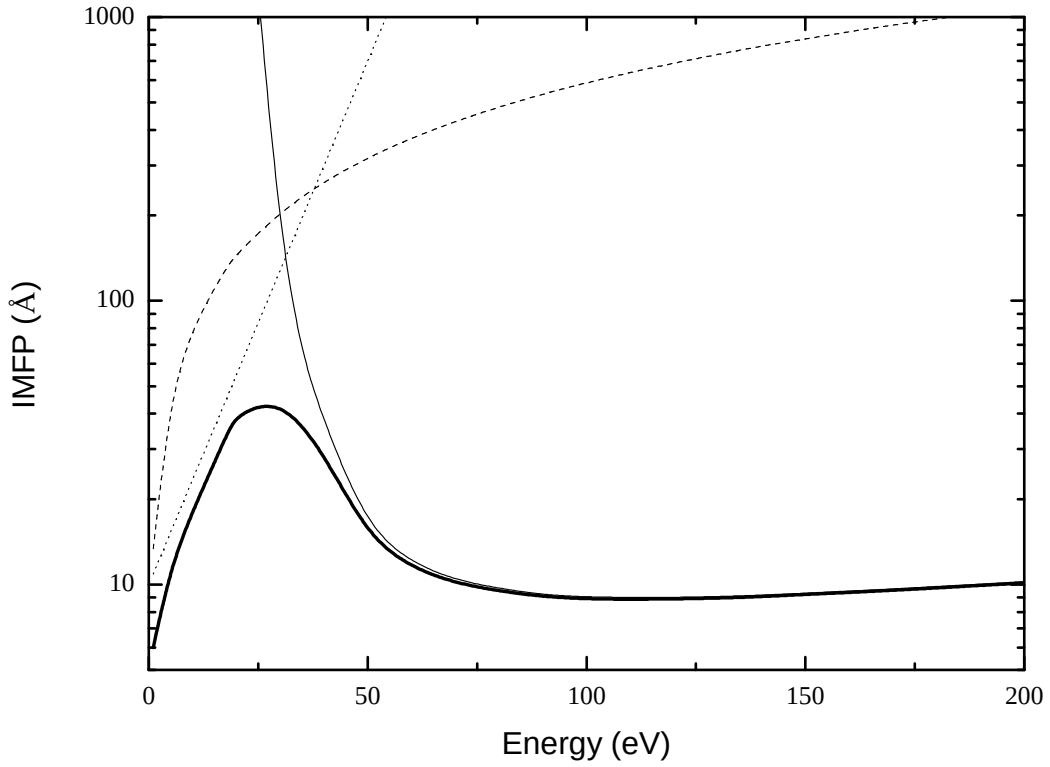

Figure 4.13: Inelastic mean free path (IMFP) of electrons in SiO_2 corresponding to the various mechanisms of energy loss. Electron-electron inelastic mean free path, $\lambda_{\rm inel}$, is represented by the solid line. Electron-phonon inelastic mean free path, $\lambda_{\rm phonon}$, is represented by the dashed line. Electron-polaron inelastic mean free path, $\lambda_{\rm pol}$, is represented by the dotted line. The electron inelastic mean free path $\lambda_{\rm in}$ is given by $\lambda_{\rm in}^{-1} = \lambda_{\rm inel}^{-1} + \lambda_{\rm phonon}^{-1} + \lambda_{\rm pol}^{-1}$ and is represented by the bold solid line. It approaches zero as the electron energy goes to zero. $W_{\rm ph}$=0.1 eV, C=0.1 Å^{-1}, γ=0.085 eV^{-1}.

Part II

Monte Carlo and modeling methodology

Chapter 5

Random numbers

As Monte Carlo is a statistical method, the accuracy of its results depends on the number of simulated electron trajectories and on the pseudo-random number generator used to perform the simulations. We will briefly summarize how pseudo-random numbers can be generated. We will describe, as well, how to calculate selected random number distributions which are particularly relevant for the Monte Carlo purposes [61].

5.1 Basic aspects

We are firstly interested in a generator of pseudo-random numbers uniformly distributed in the range [0, 1]. Once it is given, we shall describe the way to generate pseudo-random numbers uniformly distributed in a given interval; pseudo-random numbers distributed according to the Poisson density of probability; and pseudo-random numbers distributed according to the Gauss density of probability [62].

5.1.1 Generating pseudo-random numbers

The algorithm most frequently used for the generation of pseudo-random numbers uniformly distributed in a given interval provides the entire sequence from a "seed" number: starting with an initial number, known as the seed, one calculates the subsequent random numbers using an equation which permits to obtain each random number from the previous one. Every number of the sequence is computable knowing the value of the last calculated

random number [62, 63].

Let us suppose that $\mu_{\rm n}$ is the $n^{\underline{\rm th}}$ pseudo-random number. Then the next random number $\mu_{\rm n+1}$ is given by

$$\mu_{\rm n+1} = (a\mu_{\rm n} + b) \bmod m \tag{5.1}$$

where a, b and m are three integer numbers. Choosing the values of the three "magic" numbers a, b, and m in a proper way, one obtains sequences of random numbers corresponding to the maximum period (which is equal to m). In such a way, for every initial seed μ_0, all the integer numbers from 0 to $m-1$ will be in the sequence.

Several proposals were provided for the three "magic" numbers a, b, and m. Statistical tests have been used to establish the values of the three numbers a, b, and m in order to well approximate a sequence of integer random numbers uniformly distributed in the interval from 0 to $m-1$ [62]. A simple proposal is the so-called "minimal standard" which corresponds to a=16807, b=0, m=2147483647.

In order to obtain a sequence of real numbers uniformly distributed in the range [0, 1], it is sufficient to divide by m all the numbers obtained by Eq. (5.1).

Pseudo-random number generators used today in the programming languages such as C or C++ are more accurate than the minimal standard. They are based, anyway, on an approach similar to that expressed by Eq. (5.1) [62].

5.1.2 Testing pseudo-random number generators

A classical test to check the quality and the uniformity of a pseudo-random number generator consists in simulating $\pi = 3.14...$. Let us generate a statistical significant number of pairs of random numbers in the range $[-1, 1]$. If the distribution of the generated pseudo-random numbers would approach a perfectly uniform distribution of random numbers, then the fraction of generated points which lie within the unit circle (i.e., the number of pairs in the circle divided by the total number of generated pairs) should approach $\pi/4$. Using the random number generator "rand()" provided by the C++ compiler "Dev-C++ 4.9.9.0", we obtained for π the values 3.1411 ± 0.0005 with 10^7 pairs, 3.1415 ± 0.0001 with 10^8 pairs, and 3.1417 ± 0.0001 with 10^9

pairs.

5.1.3 Pseudo-random numbers distributed according to a given probability density

Let us indicate with ξ a random variable defined in the range $[a, b]$ distributed according to a given probability density $p(s)$. If μ represents a random variable uniformly distributed in the range [0,1], then the values of ξ can be obtained by the use of the equation:

$$\int_a^{\xi} p(s)\, ds = \mu \; . \tag{5.2}$$

Pseudo-random numbers uniformly distributed in the interval $[a, b]$

Starting from a distribution μ uniformly distributed in the range [0, 1], we can use Eq. (5.2) to obtain a uniform distribution η in the interval $[a, b]$. The distribution η corresponds to the probability density:

$$p_\eta(s) = \frac{1}{b-a} \; . \tag{5.3}$$

η satisfies the equation:

$$\mu = \int_a^{\eta} p_\eta(s)\, ds = \int_a^{\eta} \frac{ds}{b-a} \; . \tag{5.4}$$

As a consequence,

$$\eta = a + \mu(b-a) \; . \tag{5.5}$$

The expected value of the distribution is given by:

$$\langle \eta \rangle = (a+b)/2 \; . \tag{5.6}$$

Pseudo-random numbers distributed according to the Poisson density of probability

Starting from a distribution μ uniformly distributed in the range [0, 1], we can use Eq. (5.2) to get the Poisson distribution as well. It is a very important distribution for the Monte Carlo simulations, as the stochastic process for multiple scattering follows a Poisson-type law. The Poisson distribution is defined by the following probability density:

$$p_\chi(s) = \frac{1}{\lambda} \exp\left(-\frac{s}{\lambda}\right) \ , \tag{5.7}$$

where λ is a constant.

A random variable χ distributed according to the Poisson law, and defined in the interval $[0, \infty)$, is given by the solution of the equation:

$$\mu = \int_0^\chi \frac{1}{\lambda} \exp\left(-\frac{s}{\lambda}\right) \ ds \ , \tag{5.8}$$

where μ is, as usual, a random variable uniformly distributed in the range [0, 1]. Then

$$\chi = -\lambda \ln(1 - \mu) \ . \tag{5.9}$$

Since the distribution of $1 - \mu$ is equal to that of μ, we also have:

$$\chi = -\lambda \ln(\mu) \ . \tag{5.10}$$

The constant λ is the expected value of χ:

$$\langle \chi \rangle \ = \ \lambda \ . \tag{5.11}$$

Pseudo-random numbers distributed according to the Gauss density of probability

In order to describe the elastic peak, we have to calculate random variables with Gaussian distribution. The sequences of random numbers distributed with Gaussian density are calculated in this work by using the Box-Muller method [62].

Let us indicate with μ_1 and μ_2 two sequences of random numbers uniformly distributed in the interval [0, 1]. Let us consider the transformation:

$$\gamma_1 = \sqrt{-2 \ln \mu_1} \cos 2\pi\mu_2 \ , \tag{5.12}$$

$$\gamma_2 = \sqrt{-2 \ln \mu_1} \sin 2\pi\mu_2 \ . \tag{5.13}$$

Algebraic manipulations permit to calculate μ_1 and μ_2,

$$\mu_1 = \exp\left[-\frac{1}{2}(\gamma_1^2 + \gamma_2^2)\right] \ , \tag{5.14}$$

$$\mu_2 = \frac{1}{2\pi} \arctan \frac{\gamma_2}{\gamma_1} \ . \tag{5.15}$$

Let us now consider the Jacobian J of the random variables μ_1 and μ_2 with respect to the random variables γ_1 and γ_2. It is given by

$$J = -g(\gamma_1)g(\gamma_2) \ , \tag{5.16}$$

where

$$g(\gamma) = \frac{\exp(-\gamma^2/2)}{\sqrt{2\pi}} \ . \tag{5.17}$$

Thus the two random variables γ_1 and γ_2 are distributed according to the Gaussian density.

5.2 Concluding remarks about random numbers

We have described the algorithm most frequently used for the generation of pseudo-random numbers uniformly distributed in a given interval. It provides

the whole sequence from a seed number. Starting with a given initial number, the algorithm computes the subsequent pseudo-random numbers according to a simple rule. Knowing the value of the last calculated pseudo-random number, any other number in the sequence is therefore easily computable. Once provided a generator of pseudo-random numbers uniformly distributed on the range [0, 1], sequences of pseudo-random numbers distributed according to given densities of probability can be obtained by the use of specific algorithms. Several examples, useful for the purposes of transport Monte Carlo, were provided in the chapter.

Chapter 6

Monte Carlo strategies

Monte Carlo is one of the most powerful theoretical methods for evaluating the physical quantities related to the interaction of electrons with a solid target. A Monte Carlo simulation can be considered as an idealized experiment. The simulation does not investigate the fundamental principles of the interaction. It is necessary to know them – in particular the energy loss and angular deflection phenomena – to produce a good simulation. All the cross-sections and mean free paths have to be previously accurately calculated: they are then used in the Monte Carlo code in order to obtain the macroscopic characteristics of the interaction processes by simulating a large number of single particle trajectories and then averaging them. Due to recent evolution in computer calculation capability, we are now able to obtain statistically significant results in very short times of calculation.

Two main strategies can be utilized in order to simulate electron transport in solid targets. The first one, the so-called continuous-slowing-down approximation, is very simple and assumes that electrons continuously lose energy as they travel inside the solid, changing direction when elastic collisions occur. It is frequently used – for it is a very fast procedure – when the description of the statistical fluctuations of the energy loss due to the different energy losses suffered by each electron of the penetrating beam and of the shower of secondary electron are not crucial for simulating the desidered quantities: this is the case, for example, of the calculation of the backscattering coefficient or of the depth distribution of the absorbed electrons. If, on the other hand, accurate description of all the inelastic events which occur along the electron path – i.e., of the statistical fluctuations of the energy loss – are needed to describe the investigated phenomena, as for example

when we are interested in predicting the energy distribution of the electrons emitted by the surface of the solid target, a second strategy is required: a strategy where energy straggling is properly taken into account simulating all the single energy losses occuring along the electron trajectory (together with the description of the elastic events in order to take into account the changes of direction). In this chapter both these strategies will be briefly described, while the discussion of specific features and details will be found in the chapters devoted to the applications.

In both the descriptions we will adopt spherical coordinates (r, θ, ϕ) and assume that a stream of monoenergetic electrons irradiates a solid target in the z direction. In some of the applications presented in the next chapters, we shall consider angles of incidence, with respect to the normal to the target surface, different from zero.

6.1 The continuous-slowing-down approximation

Let us firstly describe the Monte Carlo method based on the continuous-slowing-down approximation. It requires the use of the stopping power – for calculating the energy losses along the electron trajectories – while the electron angular deflections are ruled by the Mott cross-section.

6.1.1 The step-length

The stochastic process for multiple scattering is assumed to follow a Poisson-type law. The step-length Δs is then given by

$$\Delta s = -\lambda_{\mathrm{el}} \ln(\mu_1) \ , \tag{6.1}$$

where μ_1 is a random number uniformly distributed in the range [0, 1] and λ_{el} is the elastic mean free path:

$$\lambda_{\mathrm{el}} = \frac{1}{N\sigma_{\mathrm{el}}} \ . \tag{6.2}$$

Here we have indicated with N the number of atoms per unit volume in the solids and with σ_{el} the total elastic scattering cross-section, given by

$$\sigma_{\rm el}(E) \;=\; \int \frac{d\sigma_{\rm el}}{d\Omega}\, d\Omega \;=\; \int_0^{\pi} \frac{d\sigma_{\rm el}}{d\Omega}\, 2\,\pi\, \sin\vartheta\, d\vartheta\;. \tag{6.3}$$

6.1.2 Interface between over-layer and substrate

For surface films, the interface between the over-layer and the substrate must be properly taken into account. The change in the scattering probabilities per unit length in passing from the film to the substrate and vice versa, have to be considered, so that Eq. (6.1) has to be accordingly modified. Let us denote with p_1 and p_2 the scattering probabilities per unit length for the two materials, where p_1 refers to the material in which the last elastic collision occured and p_2 to the other material and let us indicate with d the distance along the scattering direction between the initial scattering and the interface. According to Horiguchi *et al.* [64] and Messina *et al.* [65], if μ_1 is a random number uniformly distributed in the range [0, 1], the step-length Δs is given by,

$$\Delta s = \begin{cases} (\frac{1}{p_1})[-\ln(1-\mu_1)], & 0 \le \mu_1 < 1-\exp(-p_1 d); \\ d + (\frac{1}{p_2})[-\ln(1-\mu_1) - p_1 d], & 1-\exp(-p_1 d) \le \mu_1 \le 1. \end{cases} \tag{6.4}$$

6.1.3 The polar scattering angle

The polar scattering angle θ after an elastic collision is calculated assuming that the probability of elastic scattering into an angular range from 0 to θ,

$$P_{\rm el}(\theta, E) \;=\; \frac{2\,\pi}{\sigma_{el}} \int_0^{\theta} \frac{d\sigma_{\rm el}}{d\Omega}\, \sin\vartheta\, d\vartheta\;, \tag{6.5}$$

is a random number μ_2 uniformly distributed in the range [0, 1]:

$$\mu_2 \;=\; P_{\rm el}(\theta, E)\;. \tag{6.6}$$

In other words, the sampling of the elastic scattering is performed looking for the angle of scattering corresponding to a random number uniformly distributed in the range [0, 1] (see Fig. 6.1). The angle of scattering, for any given electron energy, is calculated looking for the upper limit of integration in Eq. (6.5), once imposed that μ_2 be equal to $P_{\rm el}(\theta, E)$ [Eq. (6.6)].

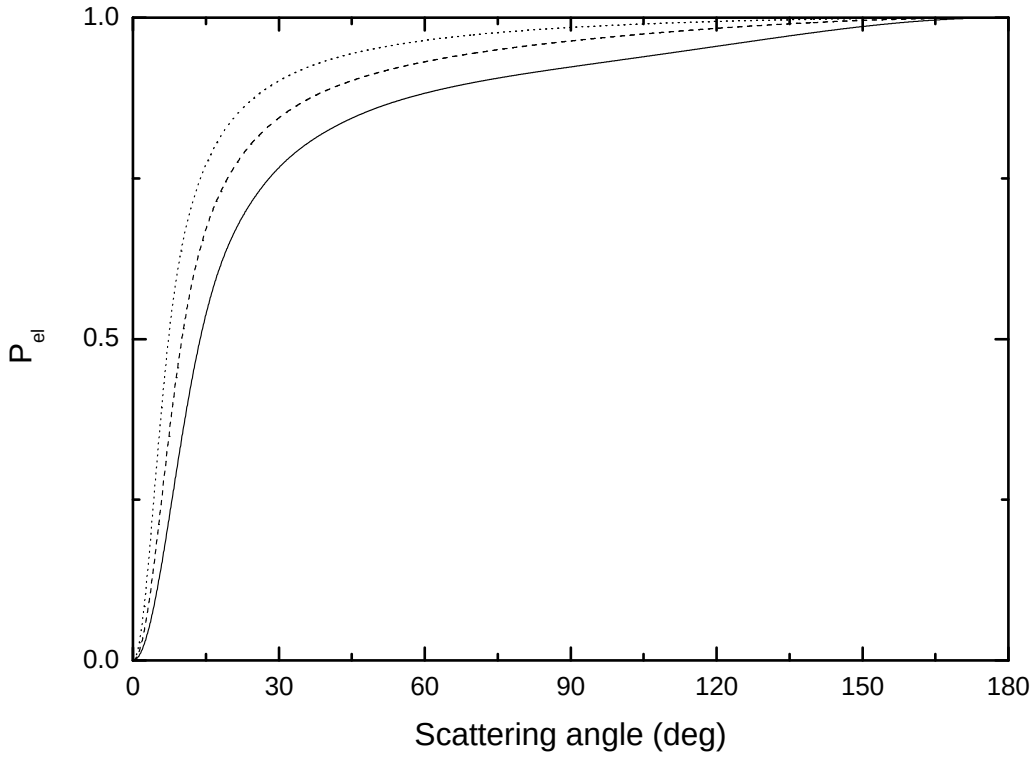

Figure 6.1: Sampling of the elastic scattering angle for electrons in silicon. P_{el} is the cumulative probability for elastic scattering into an angular range from 0 to θ calculated numerically solving the Dirac equation in a central field, according to the relativistic partial wave expansion method (Mott cross-section). Solid line: E = 500 eV; dashed line: E = 1000 eV; dotted line: E = 2000 eV. Present calculation.

6.1.4 Direction of the electron after the last deflection

The azimuth angle ϕ can assume any value selected by a random number μ_3 uniformly distributed in the range $[0,\ 2\pi]$.

Both the θ and ϕ angles refer to the last direction before the impact. The direction $\theta_z^{'}$ in which the electron is moving after the last deflection, relative to the z direction, is given by

$$\cos\theta_{\rm z}^{'} = \cos\theta_{\rm z}\cos\theta + \sin\theta_{\rm z}\sin\theta\cos\phi\ . \tag{6.7}$$

In the last equation, θ_z is the angle relative to the z direction before the impact. The step of trajectory along the z direction, Δz, is then obtained by

$$\Delta z = \Delta s\cos\theta_{\rm z}^{'}\ . \tag{6.8}$$

The new angle $\theta_{\rm z}^{'}$ is the incident angle $\theta_{\rm z}$ corresponding to the next path length.

6.1.5 The energy loss

The basic idea of the continuous-slowing-down approximation, is to assume that electrons lose energy with continuity while they are traveling in the solid: in order to calculate the energy loss along the various segments of the electron trajectory, use is made of the stopping power, introduced in the first chapter and subsequently described in the various theoretical and semi-empiric approaches one can find in the literature.

Monte Carlo codes typically approximate the energy loss ΔE along the segment of trajectory Δz by the following equation

$$\Delta E = (dE/dz)\Delta z\ , \tag{6.9}$$

where $-dE/dz$ is the electron stopping power. With this approach, statistical fluctuations of the energy losses are completely neglected. As a consequence this kind of Monte Carlo strategy should be avoided when detailed information about energy loss mechanisms are required (for example when we are interested in the energy distribution of the emitted electrons).

6.1.6 End of the trajectory and number of trajectories

Each electron is followed until its energy becomes lower than a given value or until it emerges from the target surface. The selection of the value of the cut off energy depends on the particular problem one is investigating. For the calculation of the backscattering coefficient, for example, the electrons are followed until their energy becomes smaller than 50 eV.

Notice that even the number of trajectories is a crucial quantity to get statistically significant results and to improve the signal to noise ratio. In this work the typical number of trajectories, used for the presented simulations based on the continuous-slowing-down approximation strategy, ranges from 10^5 to 10^6, depending on the particular problem investigated.

6.2 The energy-straggling strategy

Let us now describe the Monte Carlo method based on the energy-straggling strategy. It requires a detailed knowledge of all the energy loss mechanisms and probabilities (electron-electron, electron-phonon, electron-polaron cross-sections) while the electron angular deflections are ruled, as for the case of the continuous-slowing-down approximation, by the use of the Mott cross-section.

6.2.1 The step-length

The Monte Carlo method based on the energy-straggling strategy requires an approach different from that based on the continuous-slowing-down approximation. Also in this case the stochastic process for multiple scattering is assumed to follow a Poisson-type law. The step-length Δs is thus given by

$$\Delta s = -\lambda \ \ln(\mu_1) \ , \tag{6.10}$$

where μ_1 is, as for the previous case, a random number uniformly distributed in the range [0, 1]. Now λ is no longer the elastic mean free path. It is instead given by

$$\lambda = \frac{1}{N \ (\sigma_{\rm in} + \sigma_{\rm el})} \ , \tag{6.11}$$

where $\sigma_{\rm in}$ is the total inelastic scattering cross-sections (the sum of all the inelastic and quasi-elastic scattering cross-sections), i.e.,

$$\sigma_{\rm in} \;=\; \sigma_{\rm inel} + \sigma_{\rm phonon} + \sigma_{\rm pol} \tag{6.12}$$

and $\sigma_{\rm el}$ is the total elastic scattering cross-section (Mott cross-section). Therefore,

$$\lambda = \frac{1}{N\,(\sigma_{\rm inel} + \sigma_{\rm phonon} + \sigma_{\rm pol} + \sigma_{\rm el})}\;, \tag{6.13}$$

or, since $N\sigma_{\rm inel} = 1/\lambda_{\rm inel}$, $N\sigma_{\rm phonon} = 1/\lambda_{\rm phonon}$, $N\sigma_{\rm pol} = 1/\lambda_{\rm pol}$, and $N\sigma_{\rm el} = 1/\lambda_{\rm el}$,

$$\frac{1}{\lambda} = \frac{1}{\lambda_{\rm inel}} + \frac{1}{\lambda_{\rm phonon}} + \frac{1}{\lambda_{\rm pol}} + \frac{1}{\lambda_{\rm el}}\;. \tag{6.14}$$

6.2.2 Elastic and inelastic scattering

Before each collision, a random number μ_2 uniformly distributed in the range [0, 1] is generated and compared with the probability of inelastic scattering, $p_{\rm in}$, given by

$$p_{\rm in} = \frac{\sigma_{\rm in}}{\sigma_{\rm in} + \sigma_{\rm el}} \;=\; \frac{\lambda}{\lambda_{\rm in}}, \tag{6.15}$$

while that of elastic scattering is

$$p_{\rm el} = 1 - p_{\rm in}. \tag{6.16}$$

If the random number μ_2 is less than or equal to $p_{\rm in}$, then the collision will be inelastic; otherwise, it will be elastic.

If the collision is inelastic, a similar procedure is followed to establish which kind of inelastic process will occur among the following ones: electron-electron (Ritchie [17]), quasi-elastic electron-phonon (Fröhlich [18]), or electron polaron (Ganachaud and Mokrani [19]) interaction.

If the collision is elastic, the polar scattering angle θ is calculated generating a random number μ_3, uniformly distributed in the range [0, 1], representing the probability of elastic scattering into an angular range from 0 to θ:

$$\mu_3 = P_{\rm el}(\theta, E) = \frac{1}{\sigma_{el}} \int_0^{\theta} \frac{d\sigma_{el}}{d\Omega}\, 2\pi\, \sin\vartheta\, d\vartheta\ . \tag{6.17}$$

In each electron-electron inelastic collision we calculate te function $P_{\rm inel}(W, E)$ providing the fraction of electrons losing energies less than or equal to W [66] (see Fig. 6.2 where the function $P_{\rm inel}(W, E)$ is represented for 1000 eV electrons impinging on Si): the energy loss W is obtained by generating a random number μ_4 uniformly distributed in the range [0, 1], and imposing that μ_4 is equal to $P_{\rm inel}(W, E)$:

$$\mu_4 = P_{\rm inel}(W, E) = \frac{1}{\sigma_{\rm inel}} \int_0^{W} \frac{d\sigma_{\rm inel}}{dw} dw\ . \tag{6.18}$$

Also a secondary electron is generated whose energy is equal to the energy lost by the incident electron, W.

If the next collision is an electron-phonon one, the energy lost by the electron is $W_{\rm ph}$. Eventually, if a polaron is generated, the electron ends its travel in the solid, as it is trapped where the collision occured.

6.2.3 Electron-electron collisions: scattering angle

Let us consider the collision between two electrons. Let us assume that one of them is initially at rest. Let us indicate with $\vec{p}$ and E the initial momentum and energy, respectively, of the incident electron, with $\vec{p'}$ and E' the momentum and energy, respectively, of the incident electron after the collision, and with $\vec{q}$ and ΔE the momentum and energy, respectively, of the electron which was initially at rest (the so-called secondary electron) after the collision. Let us indicate with θ and θ_s, respectively, the polar scattering angles of the incident and of the secondary electrons. Useful relationships between these quantities can be provided using the so-called classical binary-collision model, which is sufficiently accurate for many practical purposes. Due to conservation of momentum and energy,

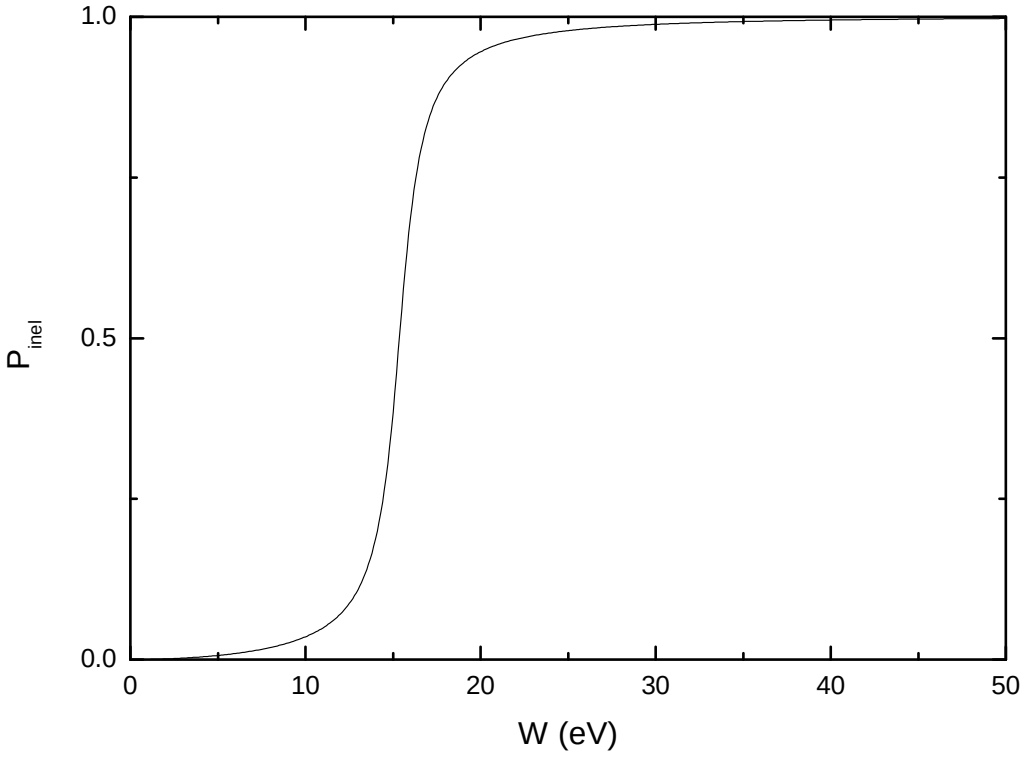

Figure 6.2: Sampling of the energy loss for electrons in silicon. $P_{\rm inel}$ is the cumulative probability for inelastic collisions of electrons in Si (calculated according to the dielectric Ritchie theory) causing energy losses less than or equal to W. The cumulative probability is here represented, as a function of the energy loss W, for E = 1000 eV. Present calculation.

$$\sin\theta_s \;=\; \cos\theta\,, \tag{6.19}$$

where the polar scattering angle θ depends on the energy loss ΔE according to the equation

$$\frac{W}{E} \;=\; \frac{\Delta E}{E} \;=\; \sin^2\theta\,. \tag{6.20}$$

Let us firstly demonstrate Eq. (6.19). To do that, we have to prove that the momenta of the two electrons in the final state are perpendicular. Let us then introduce the angle β between $\vec{p'}$ and $\vec{q}$. From momentum conservation,

$$\vec{p} \;=\; \vec{p'} \;+\; \vec{q}\,,$$

we get

$$p^2 \;=\; p'^2 \;+\; q^2 \;+\; 2p'q\cos\beta\,. \tag{6.21}$$

On the other hand, from conservation of energy,

$$E \;=\; E' \;+\; \Delta E\,,$$

it follows that

$$p^2 \;=\; p'^2 \;+\; q^2\,. \tag{6.22}$$

The comparison between Eq. (6.21) and Eq. (6.22) allows us to conclude, as anticipated, that

$$\beta \;=\; \frac{\pi}{2}\,, \tag{6.23}$$

which is equivalent to Eq. (6.19).

Let us now examine the consequences of the conservation laws to the dependence of the scattering angle θ – the angle between the initial momentum $\vec{p}$ and the final momentum $\vec{p'}$ of the incident electron – on its energy loss. As

$$\vec{p} \;-\; \vec{p'} \;=\; \vec{q}\,,$$

we get

$$q^2 \;=\; p^2 \;+ p'^2 \;-\; 2pp'\cos\theta \;. \tag{6.24}$$

Eq. (6.24) has two important consequences. The first one is that, in the final state, the absolute value of momentum $\vec{q}$ of the electron initially at rest, q, can assume only values belonging to the finite interval $[q_-,q_+]$ where

$$q_\pm \;=\; \sqrt{2mE} \;\pm\; \sqrt{2m(E-\Delta E)}\;, \tag{6.25}$$

as one can immediately see imposing, in Eq. (6.24), $\theta = 0$ (corresponding to q_-) and $\theta = \pi$ (corresponding to q_+).

The second consequence of Eq. (6.24) is that it offers the possibility, when conservation of energy is considered as well, to obtain the relationship between the scattering angle and the energy loss of the incident electron represented by Eq. (6.20). Indeed, according to Eq. (6.22), $q^2 = p^2 - p'^2$, so that, comparing this result with that expressed by Eq. (6.24), we get

$$\cos^2\theta \;=\; \frac{p'^2}{p^2} \;=\; \frac{E'}{E}\;, \tag{6.26}$$

which is equivalent to Eq. (6.20).

6.2.4 Electron-phonon collisions: scattering angle

In the case of electron-phonon collision, the corresponding polar scattering angle can be calculated according to Llacer and Garwin [51]. In Appendix B, details of the calculation are given. Here we limit ourselves to provide the equations to be used in the Monte Carlo code.

Indicating with μ_5 a new random number uniformly distributed in the range [0, 1], the polar scattering angle corresponding to an electron-phonon collision can be calculated as

$$\cos\,\theta \;=\; \frac{E \;+\; E'}{2\,\sqrt{E\;E'}}\,(1 \;-\; B^{\mu_5}) \;+\; B^{\mu_5}\;, \tag{6.27}$$

where

$$B \;=\; \frac{E \;+\; E' \;+\; 2\,\sqrt{E\;E'}}{E \;+\; E' \;-\; 2\,\sqrt{E\;E'}}\,. \tag{6.28}$$

6.2.5 Direction of the electron after the last deflection

Once the polar scattering angle has been calculated, the azimuth angle is obtained generating a random number μ_6 uniformly distributed in the range $[0,\ 2\pi]$. The direction $\theta_z^{'}$ in which the electron is moving after the last deflection, relative to the z direction, is calculated by Eq. (6.7).

6.2.6 Transmission coefficient

When dealing with very slow electrons, another important question to be considered is related to their capability to emerge from the surface of the solid [67].

In fact, the condition for an electron to emerge from the surface of a solid is not always satisfied. The interface with the vacuum represents a potential barrier, and not all the electrons that reach the surface can go beyond it. When the electrons reaching the surface cannot emerge, they are specularly reflected back in the material. This problem is particularly important when investigating secondary electron emission, as secondary electrons have tipically very low energy (lower than 50 eV), so that they often cannot satisfy the condition to emerge.

When a very slow electron of energy E reaches the target surface, it can emerge from the surface only if this condition is satisfied

$$E\,\cos^2\theta \;=\; \chi\,, \tag{6.29}$$

where θ is the angle of emergency with respect to the normal to the surface, measured inside the specimen, and χ is the so-called *electron affinity*, i.e. the potential barrier represented by the difference between the vacuum level and the bottom of the conduction band. Its value depends on the investigated material. For example, the electron affinity of un-doped silicon is 4.05 eV [68].

In order to study the transmission coefficient of slow electrons through the potential barrier χ, let us consider two regions along the z direction,

inside and outside the solid, respectively. Let us further assume that the potential barrier χ be located at at $z = 0$.

The first region, inside the solid, corresponds to the following solution of the Schrödinger equation:

$$\psi_1 = A_1 \exp(i\, k_1\, z) + B_1 \exp(-i\, k_1\, z)\,, \tag{6.30}$$

while the solution in the vacuum is given by:

$$\psi_2 = A_2 \exp(i\, k_2\, z)\,. \tag{6.31}$$

In these equations, A_1, B_1, and A_2 are three constants while k_1 and k_2 are, respectively, the electron wave vectors in the solid and in the vacuum. They are given by

$$k_1 = \sqrt{\frac{2\, m\, E}{\hbar^2}}\, \cos\theta\,, \tag{6.32}$$

$$k_2 = \sqrt{\frac{2\, m\, (E-\chi)}{\hbar^2}}\, \cos\vartheta\,. \tag{6.33}$$

Here θ and ϑ represent the angles of emergence of the secondary electrons – with respect to the normal to the surface – measured, respectively, inside and outside the material.

As the following conditions of continuity have to be satisfied

$$\psi_1(0) = \psi_2(0)\,, \tag{6.34}$$

$$\psi_1'(0) = \psi_2'(0)\,, \tag{6.35}$$

the transmission coefficient T can be easily calculated to be

$$T = 1 - \left|\frac{B_1}{A_1}\right|^2 = \frac{4\, k_1\, k_2}{(k_1 + k_2)^2}\,. \tag{6.36}$$

Taking into account the definition of electron wave vectors, we get

$$T \;=\; \frac{4\sqrt{(1\;-\;\chi/E)\cos^2\vartheta/\cos^2\theta}}{\left[1\;+\;\sqrt{(1\;-\;\chi/E)\cos^2\vartheta/\cos^2\theta}\right]^2} \tag{6.37}$$

Due to the conservation of the momentum parallel to the surface

$$E\;\sin^2\theta\;=\;(E\;-\;\chi)\;\sin^2\vartheta\;. \tag{6.38}$$

As a consequence

$$\cos^2\theta\;=\;\frac{(E\;-\;\chi)\cos^2\vartheta\;+\;\chi}{E}\;, \tag{6.39}$$

$$\cos^2\vartheta\;=\;\frac{E\cos^2\theta\;-\;\chi}{E\;-\;\chi}\;. \tag{6.40}$$

In conclusion, the transmission coefficient T is given, as a function of ϑ, by

$$T\;=\;\frac{4\,\sqrt{1\;-\;\chi/[(E\;-\;\chi)\cos^2\vartheta\;+\;\chi]}}{\left\{1\;+\;\sqrt{1\;-\;\chi/[(E\;-\;\chi)\cos^2\vartheta\;+\;\chi]}\right\}^2}\;, \tag{6.41}$$

and, as a function of θ,

$$T\;=\;\frac{4\,\sqrt{1\;-\;\chi/(E\;\cos^2\theta)}}{\left[1\;+\;\sqrt{1\;-\;\chi/(E\;\cos^2\theta)}\right]^2}\;. \tag{6.42}$$

Transmission coefficient and Monte Carlo method

The transmission coefficient is an important quantity for the Monte Carlo description of low energy electrons emerging from the surface of a solid: the code generates a random number, μ_7, uniformly distributed in the range [0, 1] and permits to the electron to be emitted into the vacuum if the condition

$$\mu_7 < T \tag{6.43}$$

is satisfied. Those electrons which, once reached the surface, cannot satisfy the condition to emerge, are specularly reflected back into the bulk of the specimen without energy loss and can contribute to the generation of further secondary electrons.

6.2.7 End of the trajectory and number of trajectories

As for the case of the continuous-slowing-down approximation, described in the previous section, each electron is followed until its energy becomes lower than a given fixed treshold or until it emerges from the target surface. If, for example, we are studying the plasmon losses, the electrons can be followed until their energy becomes smaller than $E_0 - 150$ eV, as typically all the plasmon losses can be found in the energy ranges from $E_0 - 150$ eV to E_0 (where we have indicated with E_0 the primary energy expressed in eV). If on the other hand we are facing the problem of simulating the secondary electron energy distribution, the electrons must be followed until they reach a very small minimum energy (virtually equal to 0, even if a few eV can in some cases considered acceptable.)

The number of trajectories is also a very important parameter. In this work, the typical number of trajectories, using the energy-straggling strategy for simulating spectra of energy distributions, ranges from 10^7 to 10^8.

6.3 Concluding remarks about MC strategies

In this chapter the Monte Carlo method for the study of the transport of electrons in solid targets has been briefly described. Its main features and characteristics have been summarized, considering in particular two different strategies: one based on the so-called continuous-slowing-down approximation, the other one on a scheme which takes into account the energy straggling, i.e., the statistical fluctuations of the energy losses. Electron-atom, electron-electron, electron-phonon, and electron-polaron interactions have been considered with all the corresponding effects, both in term of energy losses and scattering angles.

Further details about particular features of the Monte Carlo method, which were not examined and discussed in this chapter, will be given in the chapters devoted to specific applications.

Part III

Experimental methods and materials

Chapter 7

Experimental methods and materials

This work is devoted to the computational aspects of the interaction of electron beams with solid targets, and Monte Carlo method represents tha main topic of the research. On the other hand, as the validation of the codes and of the Monte Carlo calculations requires the comparison of the simulated results with experimental data, when such data were not available in the literature, the experiments were performed in the laboratories of the Bruno Kessler Foundation (FBK), of the University of Trento, and of the University of Surrey, UK.

7.1 Backscattering coefficient of surface films

One of the problems we have considered for the present research has been the investigation of the dependence of the backscattering coefficient on the electron primary energy and on the thickness of surface films and multilayers.

7.1.1 Deposition of over-layer films

Surface layers were deposited by electron beam evaporation (Ulvac EBX-16C with Ferrotec EV S-6 e-gun) onto silicon wafers. Background pressure in the vacuum chamber was in the 10^{-7} Torr range and the deposition rate was 5 Å/sec. The film thickness was monitored during deposition by means of a quartz crystal MAXTEK Film Deposition Controller (Maxtek MDC-

360). Pd film preparation and thickness measurements were performed by Nicola Bazzanella (University of Trento). Au film preparation and thickness measurements were performed by Michele Crivellari (FBK).

7.1.2 Analysis of over-layer films

For analysis of over-layer films with the scanning electron microscope (SEM), all samples were mounted on a single stub and backscattered electron images (BEI) were acquired using a JEOL JSM7001F FEG-SEM (some selected pictures concerning thin films of Pd deposited on a bulk of Si are reported in Fig. 7.1). To compare experimental data with Monte Carlo simulations, BEI experimental curves were obtained by analyzing the grey level scale of images at different electron beam energies and making normalization to the corresponding bulk signal of the the material constituting the overlayer. Images were acquired changing the electron beam energy from 3 up to 30 keV. BEIs were analyzed using the JMicroVision v1.2.7 software [69] to better evaluate the grey scale mean value. The standard deviation of each pixel signal level from the mean value was used to estimate the errors of the experimental data. Fig. 7.1 even shows a Pd film having a nominal thickness of 100 Å. This value is too low to provide any detectable change in the grey scale contrast as a function of the primary electron energy. Indeed, even at the lowest investigated energy (3 keV), the main contribution to backscattered electron emission is provided by the substrate(s). Therefore this over-layer cannot be used for the calculation of the backscattering coefficient. On the other hand, it provides an indication about the applicability limit of this approach to the evaluation of the thickness of thin layers. It is worth saying that when thickness is so small, the film can actually be granular, with portions directly exposed to the incoming electron beam, that in this case is not interacting at all with the over-layer material [38]. For the determination of the thickness of ultra-thin films, an approach based on the main components of the energy spectra of the backscattered electrons has been proposed [70]. BEI measurements were performed by Nicola Bazzanella (University of Trento) and Laura Toniutti (University of Trento).

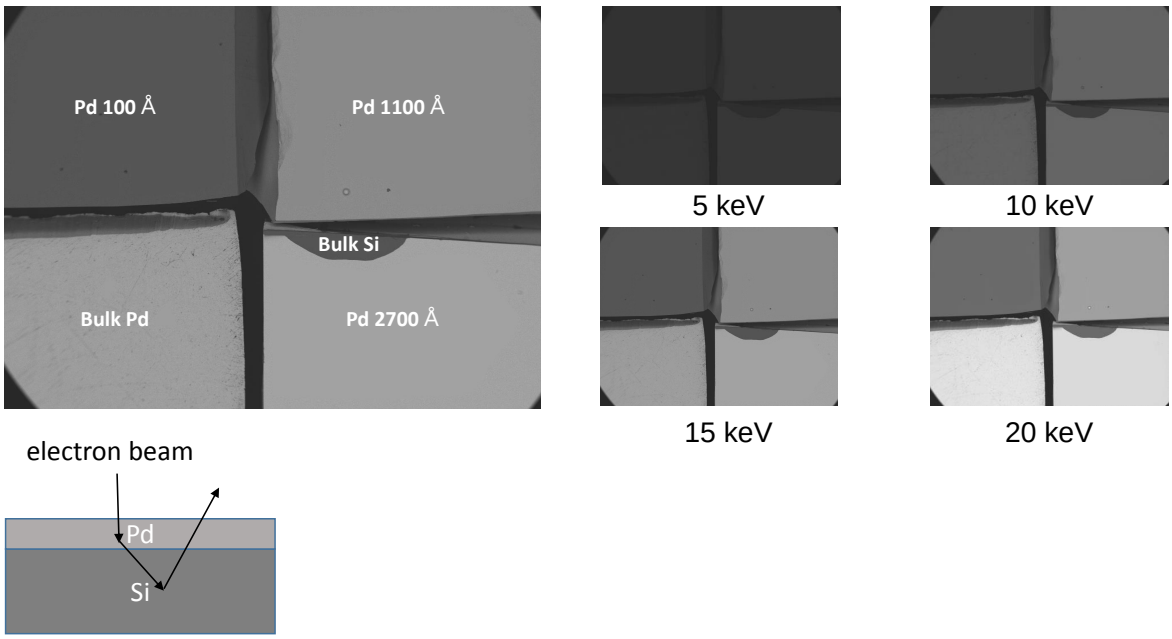

Figure 7.1: SEM BSE micrographs of the Pd on Si films, of different thicknesses, used for the experimental determination of the backscattering coefficient, and scheme of the system.

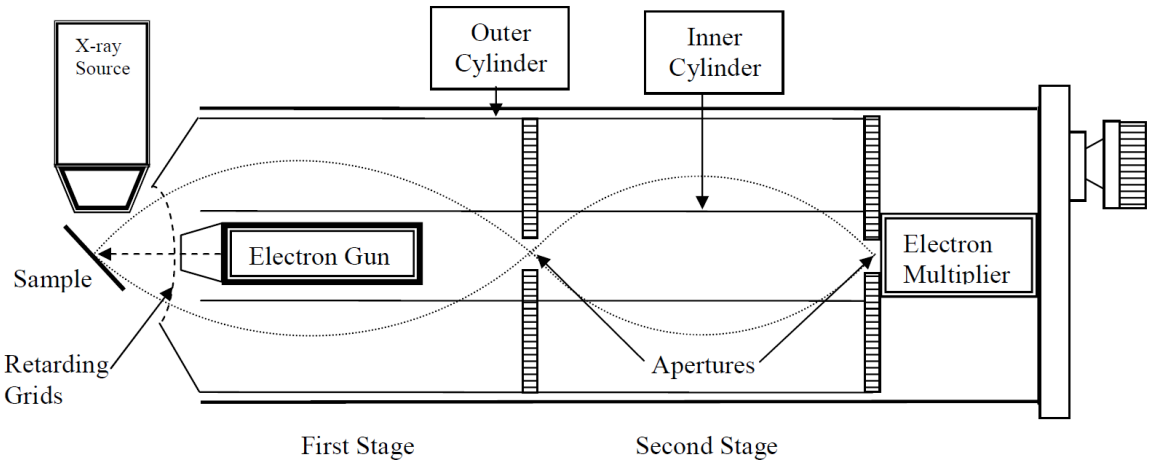

Figure 7.2: REELS experimental configuration.

7.2 Electron energy distribution spectra

Another topic we have approached in this work concerned the study of some selected feactures of the electron energy distribution spectra: in particular reflected electron energy loss peaks (specifically plasmon losses), Auger electron peaks, and secondary electron energy distributions.

7.2.1 Reflection electron energy loss and Auger electron spectra

Experimental reflection electron energy loss spectra (REELS) and Auger electron spectra (AES) were measured within a PHI545 instrument equipped with a double-pass cylindrical mirror analyser (CMA) and a coaxial electron gun (see Fig. 7.2). For a CMA, incoming electrons cross the surface at a fixed angle, $\alpha_{\text{in}} = 30°$ in our case, while outgoing electrons cross the surface at a variable angle α_{out} dependent on the angle between the surface normal and the CMA axis (30°), the entrance angle to the analyzer (42° ± 6°), and the azimuth angle in a plane normal to the CMA axis. Spectra were taken at a constant energy resolution of 0.6 eV. Once acquired, REEL spectra were corrected for the energy dependence ($E^{0.9}$) of the analyser transmission function. REELS and AES measurements were performed by Lucia Calliari (FBK), Massimiliano Filippi (FBK), and Giorgina Scarduelli (University of Trento).

7.2.2 Secondary-electron emission spectra

Experimental secondary-electron emission spectra were measured with a hemispherical analyser. The spectrometer was used in constant analyser energy (CAE) mode with a pass energy of 10 eV and a step size of 0.2 eV. All data were collected using an accelerating voltage of 1 keV and a measured sample current during collection of 1.14 nA. Secondary-electron emission measurements were performed by the group of Professor James Castle, University of Surrey, UK.

7.3 Materials

In this work some selected materials are considered for the computational study of the interaction of electrons with the matter. The behavior of an electron in a solid depends on the dielectric function, the electron affinity, the gap, the average atomic number, the phonon energy, the plasmon losses, and on many other quantities which are specific of the material investigated. As a consequence, it seems very important to validate the Monte Carlo code over a wide range of materials presenting different electronic and chemical properties.

Carbon films are deposited on various substrates (polymers, polyester fabrics, polyester yarns, metal alloys) as carbon characteristics are very useful in many fields. Carbon films are widely employed, in particular, in medical devices, as permanent thin films of pure carbon show an excellent haemo/biocompatibility. It is also well known that the fabrication of devices of interest to the microelectronic industry requires connectors to link together the circuits. Therefore, over-layer films are deposited on silicon substrates in order to create conductive pathways. These metallizations of the wafers are usually fabricated using pure metals, such as aluminum, chromium, nickel, copper, palladium, silver, platinum, gold and, sometimes, metallic alloys [37, 38].

Surface films of carbon, aluminum, copper, palladium, and gold deposited on silicon are the subject of our computational investigation of the behavior of the backscattering coefficient as a function of the film thickness. Aluminum is also one of the subjects of the present simulations of electron energy loss spectra as it exhibits very well-resolved surface and bulk plasmon peaks.

Silicon is a semi-conductor representing the most important material for the microelectronic industry and device production. Since the scale of semiconductor devices continuously decreases, reliable methods are required to quantitatively investigate the distribution of dopant atom concentrations of Si at the nanometre scale [71]. A very promising technique is the use and modeling of secondary-electron contrast in the scanning electron microscope. In this work we will present Monte Carlo results concerning secondary electron emission from silicon [43, 44]. Silicon will also be used in the present work as the substrate of thin metallic over-layers, with the purpose of investigating the behavior of the backscattering coefficient as a function of the metallic thin film thickness [37, 38]. It will be also utilized as the substrate for Polymethyl Methacrylate (PMMA), in order to extract PMMA line width

using Monte Carlo modeling [40, 41, 42] (see below).

Monte Carlo simulations of silicon plasmon-loss shape changes (surface to bulk plasmon-loss peaks ratio) as a function of the primary energy will be presented in this work as well [39, 72]. It is an useful tool for materials characterization with the use of reflection electron energy loss spectroscopy and a very promising approach for the study of the physical processes occuring at the surface of Si (low-energy electrons interactions with solids). Note that Si also exhibits, similarly to Al, quite well-resolved surface and bulk plasmon peaks.

Silicon dioxide (SiO_2) is a material of great interest for its use in the microelectronics industry. SiO_2 is used in devices utilized in radiation environments. The calculation of the energy deposition in the SiO_2 targets includes electron cascades in the material, independently on the incident radiation. In this work the simulation of the silicon dioxide electron energy loss spectrum, and the calculation of the secondary electron emission yield as a function of the incident electron energy, will be presented.

Aluminum oxide (Al_2O_3) is a ceramic material with many important biomedical applications, as it has an excellent resistance to corrosion and wear and exhibits high mechanical resistance. Furthermore, it is biocompatible, so that it is a material widely utilized in orthopedic and dental applications. In this work Monte Carlo simulations of the secondary electron emission yield as a function of the incident electron energy will be presented.

Polymethyl Methacrylate is a very important polymer for the microelectronics. In particular, it is largely used as a resist in optical and electron beam lithography. This is a crucial step in the fabrication of integrated semiconductor devices. Critical dimensions measurements during the manufacturing process have to be done. In such a way a metric is provided and yield losses are avoided. Line width extraction of PMMA resist lines is performed by high-resolution critical dimensions scanning electron microscopy (CD-SEM). Accurate nanometrology requires the comprehension of the electron beam interactions with PMMA. Then the image formation process has to be simulated in order to deconvolute the relation between the SEM image and the actual features of the specimen. As CD-SEM involves a quite complicated physics, Monte Carlo simulation of the generation and transport of secondary electrons in materials represents today the most accurate approach to solve this problem. In spite to PMMA technological importance, the number of publications that can be found in the literature describing the modeling of electron transport in PMMA is not great. Monte Carlo simulations of elec-

trons in PMMA were reported by Tan *et al.* [57]. Monte Carlo simulations of secondary electron emission with applications to linescan measurements in CD-SEM were reported in Refs. [40, 41, 42, 73, 74].

7.4 Concluding remarks about experimental methods and materials

We have briefly described the experimental equipments and methods specifically prepared and realized for the aims of the present work. Other experimental data needed to validate the Monte Carlo code were taken by the literature: in particular many results concerning both the backscattering coefficient and the secondary electron yield of bulks can be found in databases presented by several investigators in their papers devoted to these topics, and have all been quoted in the references. We have also summarized the main characteristics of the materials we have selected (C, Al, Si, Cu, Pd, Au, SiO_2, Al_2O_3, PMMA) in order to evaluate the performances of our Monte Carlo code, with the aim to validate it. The considered materials are metals, semiconductors, and insulators. The selected atomic numbers range from 6 to 79. The electronic and chemical properties of the utilized materials are very different.

Part IV

Applications of the Monte Carlo method

Chapter 8

Backscattering coefficient

The backscattered electron (BSE) emission coefficient, is defined as the fraction of electrons of the primary beam emerging from the surface of an electron-irradiated target. Secondary electrons, generated in the solid by a cascade process of extraction of the atomic electrons, are not included in the definition of the backscattering coefficient. The energy cut-off is typically 50 eV. In other words, in a typical SEM experiment aimed at measuring the fraction of backscattered electrons, investigators consider as backscattered all the electrons emerging from the surface of the target with energy higher than the cut-off energy (50 eV), while all the electrons emerging with energies lower than this conventional cut-off are considered as secondary. Of course, secondary electrons with energy higher than any predefined cut-off energy and backscattered electrons with energy lower than such a cut-off also exist. If the primary energy of the incident electron beam is not too low (if it is higher than, let's say, 1000 eV), the introduction of the 50 eV energy cut-off is generally considered as a good approximation, and it will be therefore adopted in this chapter. This choice is particularly useful, as we are interested in comparing the Monte Carlo results to many experimental data one can find in the literature, where the 50 eV energy cut-off approximation has been widely (always, actually) utilized.

Monte Carlo results concerning the Monte Carlo simulation of the electron backscattering coefficient of bulks of Al, Si, Cu, Pd, and Au will be presented in this chapter. Then a method to determine the thicknesses of thin Pd and Au over-layers – using a joint experimental/theoretical approach – will be described [37, 38]. Furthermore also a Monte Carlo study of two layers deposited on semi-infinite targets will be presented which considers, in

particular, Cu/Au/Si and C/Au/Si systems.

It is well known that over-layer films affect the electron backscattering coefficient of bulk targets. The experimental data available in the literature for backscattering coefficient are rather scattered and, sometimes, difficulties arise in their interpretation due to the lack of knowledge of the thickness, uniformity, and nature of the surface layers. In particular, a quantitative treatment of the effect of surface films deposited on bulk targets and a systematic comparison with experimental data are currently lacking. MC simulations are utilized to calculate the backscattering coefficient from surface layers deposited on bulk targets. A simple experimental set up, using a conventional Scanning Electron Microscope without the necessity of any further equipment, is demonstrated to be sufficient to establish the supported film thickness [37, 38].

In general, the determination of the C, Cu, Pd and Au over-layer thickness is a crucial step in the characterization of the microelectronic devices, so that simple ways to evaluate it are welcome and strongly encouraged. Using a field emission gun scanning electron microscope (FEG-SEM) instrument, one can fracture the Si wafer substrate and evaluate the over-layer thickness from cross-section images. Nowadays, more sophisticated approach, based on focused ion beam milling of limited regions of the device, can be adopted. In all respects, these are destructive methods, therefore not always applicable. The idea of using the energy dependence of the backscattered electrons emission coefficient for the measure of the thickness of supported thin films represents, on the other hand, a non-destructive approach as it does not require to fracture the sample. It thus provides a great advantage for many technological applications.

8.1 Electrons backscatterd from bulk targets

When an electron beam impinges on a solid target, some electrons of the primary beam are backscattered and re-emerge from the surface. We already know that the backscattering coefficient is defined as the fraction of the electrons of the incident beam which emerge from the surface with energy higher than 50 eV. This definition is very convenient and useful from the experimental point of view; it is also quite accurate, as the fraction of secondary electrons (i.e., the electrons extracted from the atoms of the target and able to reach the surface and emerge) with energy higher than 50 eV is negligible

for any practical purpose, as well as the fraction of backscattered electrons emerging with energy lower than 50 eV.

The present Monte Carlo simulation of the backscattering coefficients η as a function of the primary energy for several elemental solids is shown in Fig. 8.1. The presented results were obtained using the Mott theory for calculating elastic scattering cross-sections and the dielectric theory to calculate the stopping power (continuous-slowing-down approximation). In the examined – and here presented – incident electron energy range, the backscattering coefficient is a decreasing function of the primary energy for the elements whose atomic numbers are relatively small (Al, Si, Cu). For Au an increasing trend, as the incident electron energy increases, can be observed. Notice that the issue of the behavior of the backscattering coefficient at very low primary energy is quite controversial. The case of energies lower than 1000 eV has been experimentally investigated, but not many experimental results are available. Furthermore, not all the authors agree about the behavior of the low energy backscattering coefficient [75]. There are, in particular, no data concerning the case in which the electron energy approaches zero. Some investigators have suggested that the backscattering coefficient should approach 1 as the energy approaches 0 [76, 77]. The present Monte Carlo computations about elements with low atomic number are consistent with this suggestion.

In Tables 8.1, 8.2, 8.3, and 8.4 two sets of Monte Carlo simulated data (for the backscattering coefficient of Al, Si, Cu, and Au, respectively) – obtained using both the semi-empiric approach and the dielectric theory to calculate the stopping power – are compared with the available experimental data (taken from the Joy's database [75]).

8.2 Electrons backscatterd from over-layers

The main ingredient of the present approach is the evaluation, through experiment and modelling, of the backscattered electron emission coefficient – that results from the interplay between average atomic number and interaction volume – as compared to the actual thickness of the over-layer [37, 38]. The proposed approach is particularly interesting for the measure of semiconductor and electronic device thickness, where the requirement for non destructive characterization techniques is of fundamental importance.

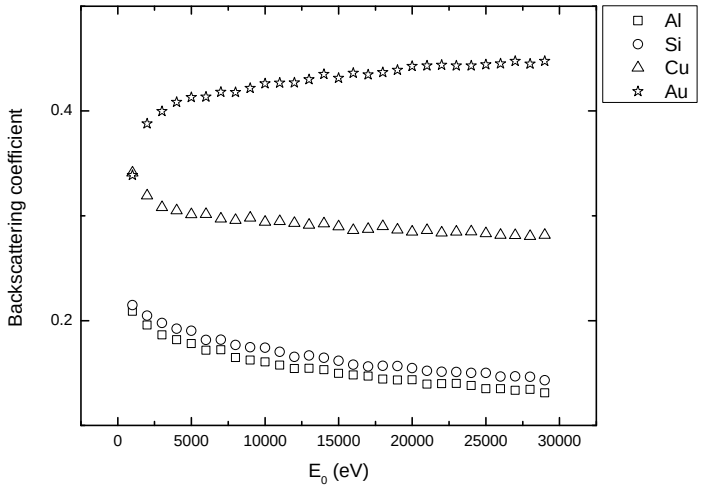

Figure 8.1: Present Monte Carlo simulation of the Monte Carlo backscattering coefficient for several elemental solids as a function of the primary energy. Continuous-slowing-down approximation. The stopping power was calculated using the Kanaya and Okayama semi-empiric theory [47].

Energy	Monte Carlo (semi-empiric)	Monte Carlo (dielectric)	Bronstein and Fraiman [78]	Reimer and Tolkamp [79]	Böngeler *et al.* [80]
1000	0.209	0.211	0.217	0.192	0.195
2000	0.196	0.176	0.200	-	0.170
3000	0.186	0.164	0.191	0.161	0.157
4000	0.182	0.159	0.185	-	0.151
5000	0.178	0.153	-	0.153	0.148

Table 8.1: Backscattering coefficient of Al as a function of the electron primary kinetic energy. Comparison between two sets of the present Monte Carlo simulated results (obtained, respectively, with the Kanaya and Okayama semi-empiric approach [47] and with the dielectric theory [17, 20, 24, 25, 81]) and the available experimental data (taken from the Joy's database [75]).

Energy	Monte Carlo (semi-empiric)	Monte Carlo (dielectric)	Bronstein and Fraiman [78]	Reimer and Tolkamp [79]
1000	0.215	0.224	0.228	0.235
2000	0.205	0.185	0.204	-
3000	0.198	0.171	0.192	0.212
4000	0.192	0.169	0.189	-
5000	0.190	0.162	-	0.206

Table 8.2: Backscattering coefficient of Si as a function of the electron primary kinetic energy. Comparison between two sets of the present Monte Carlo simulated results (obtained, respectively, with the Kanaya and Okayama semi-empiric approach [47] and with the dielectric theory [17, 20, 24, 25, 81]) and the available experimental data (taken from the Joy's database [75]).

Energy	Monte Carlo (semi-empiric)	Monte Carlo (dielectric)	Bronstein and Fraiman [78]	Koshikawa [82]	Reimer and Tolkamp [79]
1000	0.341	0.401	0.381	0.430	-
2000	0.319	0.346	0.379	0.406	-
3000	0.308	0.329	0.361	0.406	0.311
4000	0.305	0.317	0.340	-	-
5000	0.301	0.314	-	0.398	0.311

Table 8.3: Backscattering coefficient of Cu as a function of the electron primary kinetic energy. Comparison between two sets of the present Monte Carlo simulated results (obtained, respectively, with the Kanaya and Okayama semi-empiric approach [47] and with the dielectric theory [17, 20, 24, 25, 81]) and the available experimental data (taken from the Joy's database [75]).

Energy	Monte Carlo (semi-empiric)	Monte Carlo (dielectric)	Bronstein and Fraiman [78]	Reimer and Tolkamp [79]	Böngeler *et al.* [80]
1000	0.339	0.441	0.419	-	-
2000	0.388	0.456	0.450	-	0.373
3000	0.400	0.452	0.464	0.415	0.414
4000	0.408	0.449	0.461	-	0.443
5000	0.413	0.446	-	0.448	0.459

Table 8.4: Backscattering coefficient of Au as a function of the electron primary kinetic energy. Comparison between two sets of the present Monte Carlo simulated results (obtained, respectively, with the Kanaya and Okayama semi-empiric approach [47] and with the dielectric theory [17, 20, 24, 25, 81] for the stopping power calculation) and the available experimental data (taken from the Joy's database [75]).

8.2.1 The experimental approach

The experimental approach is represented in Fig. 7.1: the grey levels of the investigated samples (supported thin films of Pd and Au deposited on bulk of Si) were acquired simultaneously and under the same experimental conditions. The ratio of the values, at the same primary energy, between the grey levels of the Pd/Si (Au/Si) system and that of the bulk of Pd (Au) is equal to the ratio between the backscattering coefficient of the Pd/Si (Au/Si) system and that of the bulk of Pd (Au). For a description of a similar method of measurement of the thickness of thin films from backscattered electron image contrast, see Refs. [83, 84, 85].

8.2.2 Thickness of contamination layers

The variation of the BSE emission coefficient can be even used for the determination of the thickness of contamination layers that build up on the surface of SEM specimens under the effect of electron irradiation. Electron irradiation can indeed induce the cross linking of the surface adsorbed organic molecules [86]. The importance of a contamination layer on the BSE yield, particularly in the low energy (<5 keV) range, has been investigated with reference to several metallic specimens (Al, Cu, Au), having two differ-

Nominal thickness (Å)	Measured thickness (Å)
250	305
500	557
1000	1035
2000	2154

Table 8.5: Comparison between the nominal and the measured thicknesses of the gold thin films deposited on silicon.

ent surface finishing, resulting from the intereaction with outer atmosphere and after in situ plasma cleaning inside a high vacuum chamber [87]. In this latter condition, all adsorbed gas molecule, oxide layers and other possible contaminants were mostly eliminated and this clearly improved the BSE emission.

El Gomati *et al.* [88] have recently considered the presence of surface oxide layers as a possible reason for the discrepancies that one can observe in the literature among various experimental data concerning the measurement of the backscatering coefficient.

8.2.3 Possible source of uncertainties

In order to evaluate the possible source of uncertainties, in Tab. 8.5 the nominal thicknesses (i.e., the thicknesses corresponding to the nominal deposition parameters) are compared to the measured thicknesses relative to Au over-layers on Si substrates. Similar differences between nominal and measured thicknesses were observed for the Pd/Si samples as well.

The actual thicknesses were determined by measuring the weights of the wafers before and after deposition and assuming that the gold density for thin films was the same as bulk density (19.32 g/cm^3).

The pairs of thickness values show good agreement, within 10%, except that for the thinnest film, in which case the indetermination raise up to near 20%. To infer the effect of a 10% difference in thickness on the present Monte Carlo calculation, in Fig. 8.2, the backscattering coefficients calculated as a function of the primary energy, for 500 Å and 557 Å thin films of gold deposited on silicon, are comparatively displayed. As the relevant difference in the backscattering coefficient is always lower than 10%, this value can

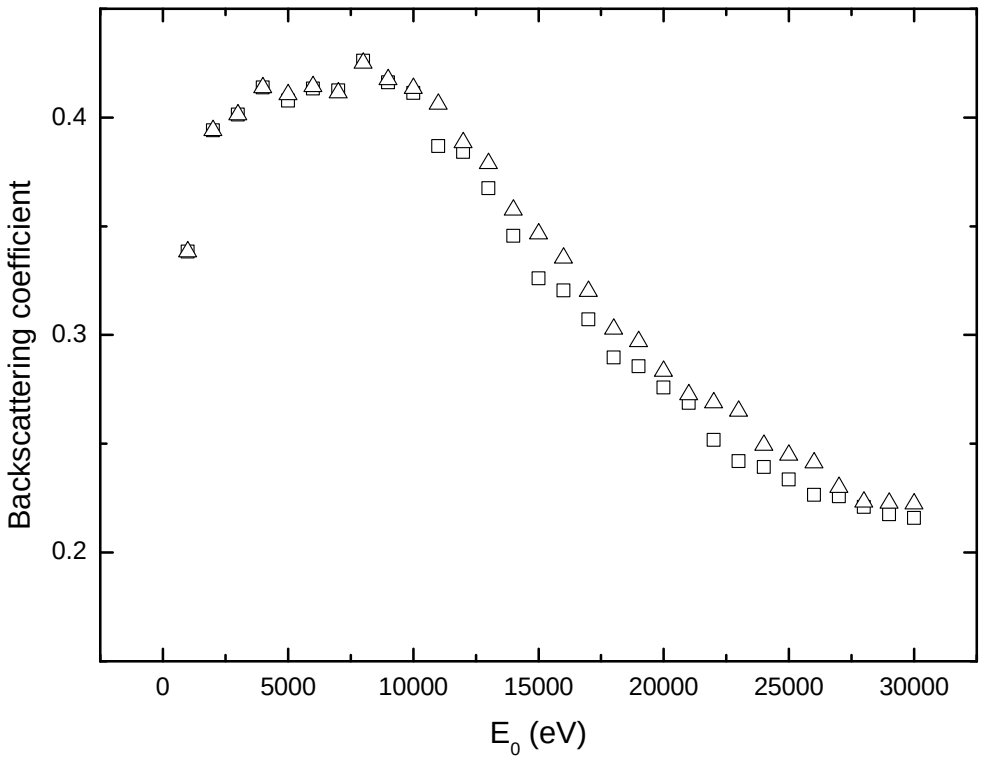

Figure 8.2: Comparison between the Monte Carlo trends of the backscattering coefficient as a function of the primary energy for two gold thin films deposited on silicon substrates. The film thicknesses are 500 Å (nominal thickness, squares) and 557 Å (measured thickness, triangles). The differences between the calculated backscattering coefficients of the two films are lower than 10% for each considered primary energy. Continuous-slowing-down approximation: stopping power was calculated using the semi-empiric approach [47]. Present calculation.

be taken as a reliable estimation of the indetermination affecting all Monte Carlo calculations concerning both Pd/Si and Au/Si systems. Therefore, all possible sources of uncertainties (not perfect uniformity of the thin films, defects, differences between bulk and thin film densities of gold, Monte Carlo statistical fluctuations, etc.) can be bracketed in this way [38].

8.2.4 Thin films of palladium deposited on silicon

Concerning the study of electron backscattering from over-layers, the Monte Carlo code – based on the stopping power calculated using the semi-empiric approach [47] – was firstly used to study the backscattering coefficient of two palladium supported thin films, whose nominal thicknesses were 1100 and 2700 Å respectively, deposited on silicon.

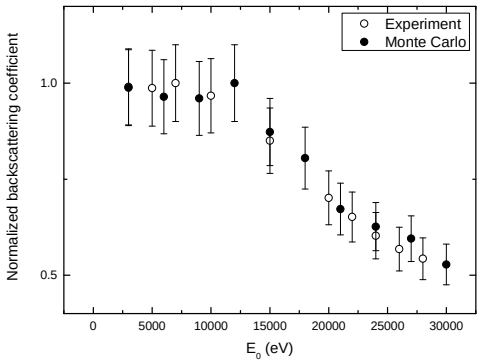

Figure 8.3: Comparison between the normalized experimental and present Monte Carlo backscattering coefficient as a function of the primary electron energy of a Pd thin film deposited on a Si substrate [37]. The Pd overlayer nominal thickness is 1100 Å. CSDA: stopping power was calculated by using the Kanaya and Okayama semi-empiric formula [47].

The primary energies considered in this study were in the range 3-30 keV. As the thickness of the substrate was, for all the electron primary energies, greater than the maximum range of penetration in silicon, the substrate can be considered as semi-infinite. The Pd layers were deposited and their thicknesses measured before their introduction in the analysis chamber. It was then possible to predict, using the Monte Carlo code, the behavior of

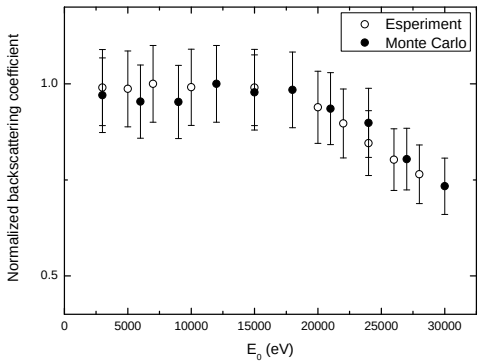

Figure 8.4: Comparison between the normalized experimental and present Monte Carlo backscattering coefficient as a function of the primary electron energy of a Pd thin film deposited on a Si substrate [37]. The Pd overlayer nominal thickness is 2700 Å. CSDA: stopping power was calculated by using the Kanaya and Okayama semi-empiric formula [47].

the backscattering coefficient as a function of the primary electron energy. Data were normalized by dividing the curves by their relevant maxima. As the selected thicknesses are in the range 1000-3000 Å, the backscattering coefficient should decrease from the value corresponding to a bulk of Pd (when the primary electron enerrgy is lower than 10-15 keV) toward the value of a bulk of Si. This prediction is confirmed by both the experimental data and the Monte Carlo results (see Figs. 8.3 and 8.4). Furthermore the Monte Carlo simulated data are in excellent agreemet with the experimental ones, also taking into account the experimental errors ($\sim 10\%$) [37].

8.2.5 Thin films of gold deposited on silicon

Figures 8.5-8.8 display the data points for the experimental backscattering coefficient and the relevant Monte Carlo results for four samples constituted by gold layers deposited on silicon [38]. The nominal thickness of the four gold films were, respectively, 250, 500, 1000, and 2000 Å. Data were normalized by dividing the curves by their relevant maxima, as for the case relative to palladium overlayers deposited on silicon described above. The experimental and the Monte Carlo approaches provide similar results, within the limits of

the quoted indetermination.

Also in this case, the backscattering coefficient of the system ranges from the value of the backscattering coefficient of gold (for very low primary energy) to the value of the backscattering coefficient of silicon (for very high primary energy). Actually, in the case of Au, the backscattering coefficient reaches a relative maximum and then it decreases to the silicon backscattering coefficient. The presence of the relative maximum was not observed for the case of the films of Pd. This difference between the behavior of the films of gold with respect to the films of Pd (in the same range of energies and thicknesses) is attributed to the different behavior of the backscattering coefficient as a function of primary energy of bulk of gold and palladium: indeed, in this energy range, the backscattering coefficient is an increasing function for gold while it is almost constant for palladium (see Fig. 8.1).

In general, the backscattering coefficient of the system should approach the behavior of the backscattering coefficient of the substrate for very thin films and, on the other hand, approach the energy dependence of the backscattering coefficient of the material constituting the overlayer for thick films. So, as the film thickness increases, the positions of the relative maxima shift towards higher energies while the peaks are broadening [38].

For a reliable and reproducible evaluation of the position of the Monte Carlo energy maximum, $E_{\max}$, the first derivative of the backscattering coefficient was calculated, as shown in Fig. 8.9. The position $E_{\max}$ as a function of the primary energy was calculated as the average of the energies corresponding to the derivative interval ranging from 0.00001 and -0.00001. The relevant error bar was estimated from the width of such an interval.

Monte Carlo simulations predict that the energy position of the maximum, $E_{\max}$, linearly depends on the gold overlayer thickness. The linear best fit of $E_{\max}$ as a function of the Au film thickness for Au/Si systems is presented in Fig. 8.10 demonstrating that with relatively simple SEM measurements of the grey levels of the backscattering images of an Au/Si system, it is possible measure the gold film thickness, with an uncertainty approximately of 20% (estimated from the statistical fluctuations in the energy maximum) [38].

In view of the non-destructiveness, the proposed approach is definitely adding new potentiality to SEM-based experimental methods.

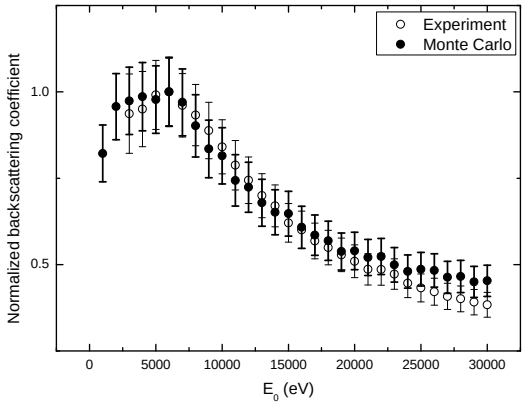

Figure 8.5: Comparison between normalized experimental and present Monte Carlo backscattering coefficient as a function of the primary electron energy of an Au thin film deposited on a Si substrate [38]. The Au overlayer nominal thickness is 250 Å. CSDA: stopping power was calculated by using the Kanaya and Okayama semi-empiric formula [47].

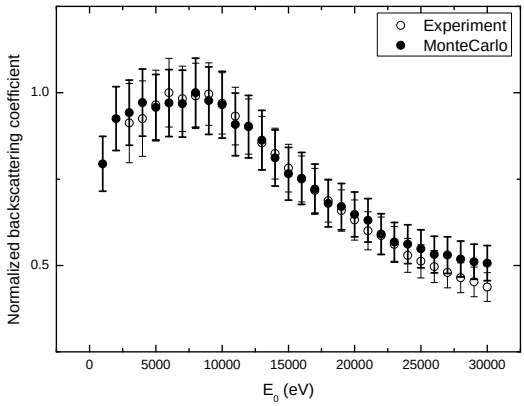

Figure 8.6: Comparison between normalized experimental and present Monte Carlo backscattering coefficient as a function of the primary electron energy of an Au thin film deposited on a Si substrate [38]. The Au overlayer nominal thickness is 500 Å. CSDA: stopping power was calculated by using the Kanaya and Okayama semi-empiric formula [47].

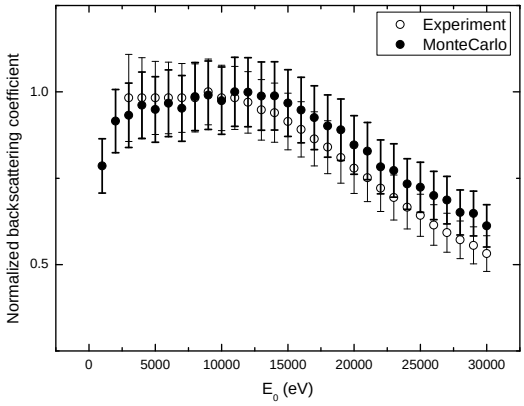

Figure 8.7: Comparison between normalized experimental and present Monte Carlo backscattering coefficient as a function of the primary electron energy of an Au thin film deposited on a Si substrate [38]. The Au overlayer nominal thickness is 1000 Å. CSDA: stopping power was calculated by using the Kanaya and Okayama semi-empiric formula [47].

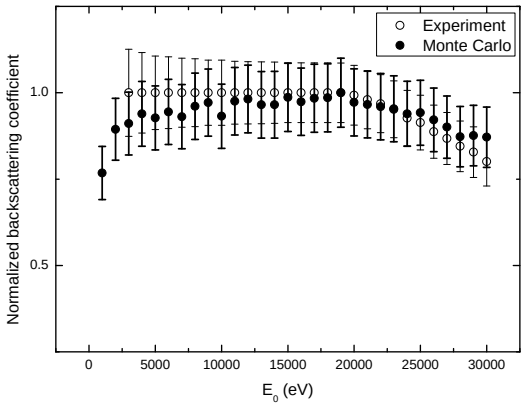

Figure 8.8: Comparison between normalized experimental and present Monte Carlo backscattering coefficient as a function of the primary electron energy of an Au thin film deposited on a Si substrate [38]. The Au overlayer nominal thickness is 2000 Å. CSDA: stopping power was calculated by using the Kanaya and Okayama semi-empiric formula [47].

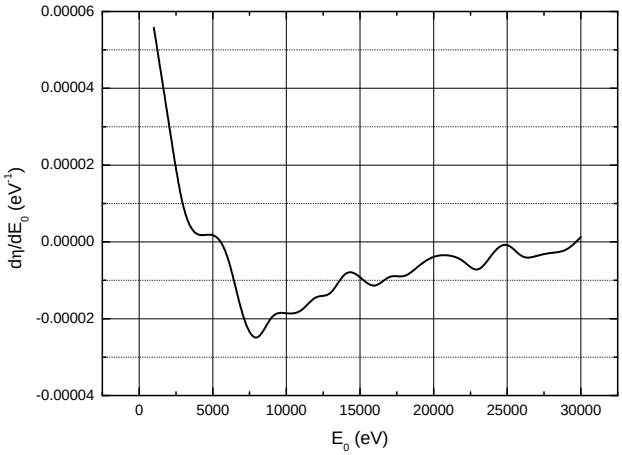

Figure 8.9: First derivative curve of the backscattered electron emission coefficient, $d\eta/dE_0$, as a function of the beam primary energy [38]. Au overlayer nominal thickness is 250 Å.

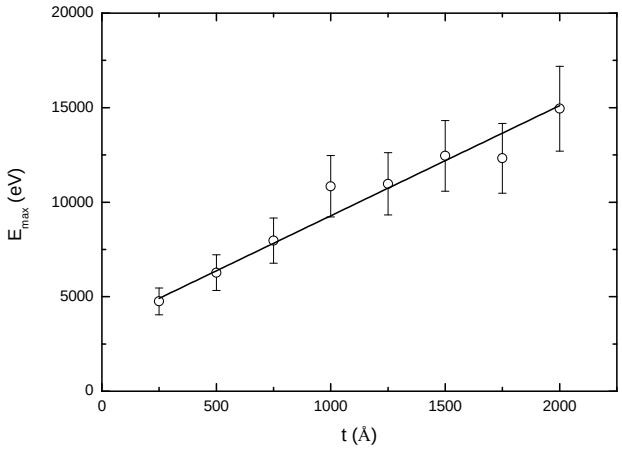

Figure 8.10: Linear best fit of Monte Carlo simulated $E_{\max}$ (in eV) as a function of the film thickness t (in Å) for Au thin films deposited on a Si substrates in the range 250 Å - 2000 Å [38]. $E_{\max} = m\,t + q$, where $m = 5.8$ eV/Å (standard error = 0.4 eV/Å) and $q = 3456$ eV (standard error = 373 eV).

8.2.6 Backscattered electrons from two layers deposited on semi-infinite substrates

The next step is represented by a comparison between the Kanaya and Okayama semi-empiric formula [47] and the dielectric approach [17, 20, 24, 25, 81] similar to that previously performed for bulk materials. As for the bulk data presented above, both the Monte Carlo codes describe the elastic scattering processes by using the Mott cross-section and, concerning the energy losses, the continuous-slowing-down approximation is utilized. We are interested now in the calculation of the backscattering coefficient from two-layers deposited on semi-infinite substrates. In particular, the backscattering from Cu/Au/Si and C/Au/Si systems will be investigated. The two different approaches for the stopping power calculations are applied to simulate the electron backscattering coefficient as a function of the thicknesses of the layers (in the range 250-2000 Å) and the electron primary energy.

In Fig. 8.11, Monte Carlo electron backscattering coefficient of Cu/Au/Si samples is represented. The Monte Carlo simulation code treats the Si substrate as a semi-infinite bulk, while the thickness of the intermediate Au layer is fixed to be 500 Å. The behavior of η as a function of the primary energy, in the range 1000-25000 eV, is represented for different values of the Cu first layer thickness, in the range 250-1000 Å. Stopping power is calculated using the dielectric response theory.

In Fig. 8.12 the same quantities are represented, obtained with the same conditions and calculated with the Monte Carlo code based on the Kanaya and Okayama semi-empiric formula.

The general trends obtained with the two codes are in good qualitative agreement: both the codes predict that the general structure of the curves presents a minimum and a maximum. Furthermore both the minimum and the maximum shift towards higher primary energies as the Cu first layer thickness increases. This features are thus characteristics of the particular combination of the selected materials and of their thicknesses.

In order to further investigate and better understand the effects of the thickness of the layers, in Figs. 8.13 and 8.14 the Monte Carlo backscattering coefficients, obtained with the dielectric response and the semi-empiric approach, respectively, have been represented for the case in which the thickness of the first Cu layer is fixed (500 Å) while the intermediate Au film thickness ranges in the 250-1000 Å interval. Also in this case the general behaviors obtained with the two approaches are in qualitative agreement.

The characteristic features present now a different trend: while the position of the maximum shifts toward higher primary energies as the intermediate film thickness increases, the position of the minimum remains practically unchanged.

In order to study the agreement between the two codes, Figs. 8.15 , 8.16, 8.17 compare the calculation of the backscattering coefficients for various combinations of materials and thicknesses, obtained using the two Monte Carlo programs. The codes give practically indistinguishable results for the cases corresponding to the C/Au/Si combination, while some difference can be observed, for the lowest energies, in the case of the Cu/Au/Si combinations.

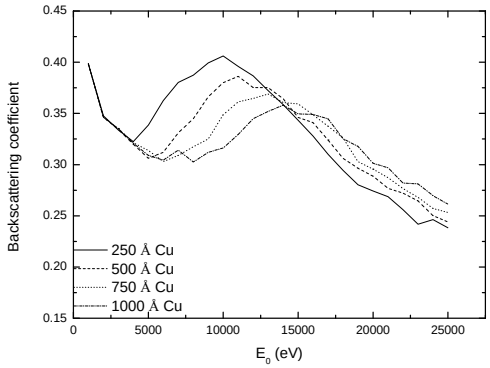

Figure 8.11: Present Monte Carlo simulation of electron backscattering coefficient η of Cu/Au/Si samples. The Si substrate is semi-infinite, while the thickness of the intermediate Au layer is 500 Å. The behavior of η as a function of the primary energy is represented for different values of the Cu first layer thickness. Stopping power is calculated using the dielectric response theory.

8.3 Concluding remarks about BSE

A very simple experimental procedure based on BSE imaging was used to validate a Monte Carlo code. The code is based on the Mott cross section for describing the elastic events [16] and on the Kanaya and Okayama semi-empiric formula for describing the inelastic processes [47]. The comparison

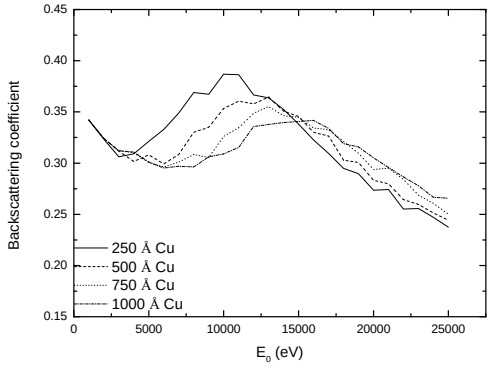

Figure 8.12: Present Monte Carlo simulation of electron backscattering coefficient η of Cu/Au/Si samples. The Si substrate is semi-infinite, while the thickness of the intermediate Au layer is 500 Å. The behavior of η as a function of the primary energy is represented for different values of the Cu first layer thickness. Stopping power is calculated using the Kanaya and Okayama semi-empiric formula.

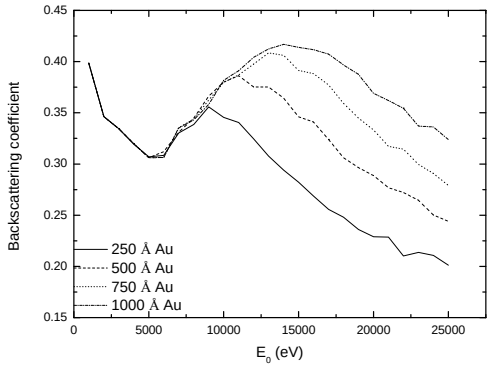

Figure 8.13: Present Monte Carlo simulation of electron backscattering coefficient η of Cu/Au/Si samples. The Si substrate is semi-infinite, while the thickness of the first Cu layer is 500 Å. The behavior of η as a function of the primary energy is represented for different values of the Au intermediate layer thickness. Stopping power is calculated using the dielectric response theory.

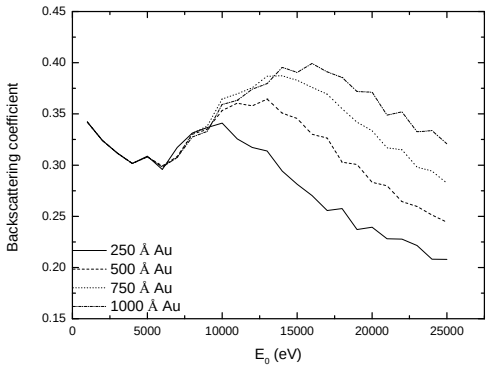

Figure 8.14: Present Monte Carlo simulation of electron backscattering coefficient η of Cu/Au/Si samples. The Si substrate is semi-infinite, while the thickness of the first Cu layer is 500 Å. The behavior of η as a function of the primary energy is represented for different values of the Au intermediate layer thickness. Stopping power is calculated using the Kanaya and Okayama semi-empiric formula.

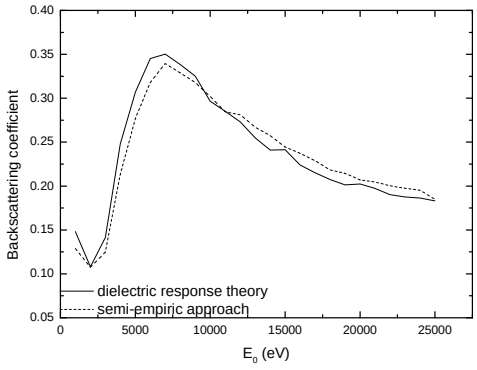

Figure 8.15: Present Monte Carlo simulation of electron backscattering coefficient η of C/Au/Si samples. The Si substrate is semi-infinite, the thickness of the first C layer is 500 Å, and that of the intermediate Au layer is 250 Å. Backscattering coefficients η obtained using the dielectric response theory and the semi-empiric Kanaya and Okayama approach, respectively, for calculating the stopping power, are compared.

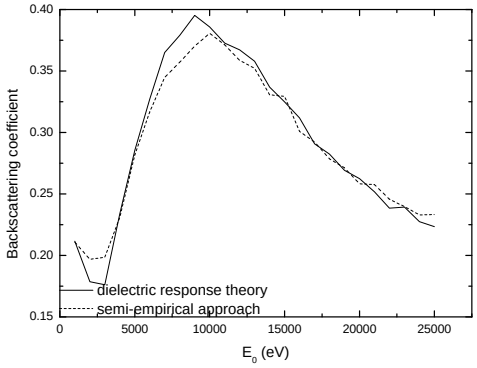

Figure 8.16: Present Monte Carlo simulation of electron backscattering coefficient η of Al/Au/Si samples. The Si substrate is semi-infinite, the thickness of the first Al layer is 500 Å, and that of the intermediate Au layer is 500 Å. Backscattering coefficients η obtained using the dielectric response theory and the semi-empiric Kanaya and Okayama approach, respectively, for calculating the stopping power, are compared.

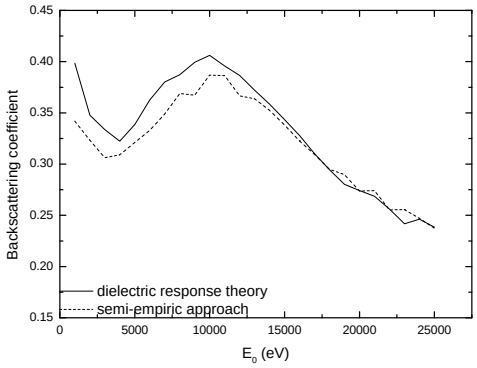

Figure 8.17: Present Monte Carlo simulation of electron backscattering coefficient η of Cu/Au/Si samples. The Si substrate is semi-infinite, the thickness of the first Cu layer is 250 Å, and that of the intermediate Au layer is 500 Å. Backscattering coefficients η obtained using the dielectric response theory and the semi-empiric Kanaya and Okayama approach, respectively, for calculating the stopping power, are compared.

between experiment and modeling was performed in the particular cases of Pd and Au surface films deposited on Si. Satisfactory agreement between experimental data and Monte Carlo results was observed. The proposed method, combining experimental observations with Monte Carlo simulations, allows to determine the thickness of metallic thin films – like those used for conductive pathways for microelectronic devices – deposited on silicon.

Two CSDA Monte Carlo codes, which differ in the utilized stopping powers, have then been used to simulate the electron backscattering coefficient from two-layer samples. In particular, the backscattering coefficient was calculated as a function of the thicknesses of the layers, their nature, and the electron primary energy. Both the codes use the Mott cross section for elastic scattering calculation and the continuous slowing down approximation for energy loss simulation. For the calculation of the stopping power, one of the programs utilizes the Ritchie dielectric response theory [17], while the other one uses the analytic semi-empirical formula proposed by Kanaya and Okayama [47]. Electron backscattering coefficients from several different combinations of layers and substrates were simulated using the two codes. The results of the codes show a general qualitative agreement. Furthermore the main features of the backscattering coefficient as a function of the electron primary energy, which are represented by a minimum and a maximum whose positions in energy depend on the particular combination of materials and thicknesses, are reproduced in similar ways by the two codes.

Chapter 9

Secondary electron yield

Electron beams impinging on solid targets stimulate the emission of secondary electrons (SE). They are the electrons extracted from the atoms bound in the solid due to the inelastic electron-atom interaction with electrons of the incident beam or with the other secondary electrons travelling in the solid. Some secondary electrons, after a number of elastic and inelastic interactions with the atoms of the solid, reach the surface of the solid satisfying the conditions to emerge from it. As we already know, the spectrum of the secondary electrons is contaminated by a contribution of the backscattered primary electrons. As this contamination can be safely neglected in the great majority of the practical situations that investigators encounter in the laboratory experiments, it is usual to ignore this effect, at least as a first approximation.

In this chapter the attention will be focused on the purely secondary electrons. The process of secondary-electron emission can be split into two phenomena. The first one concerns the generation of secondary electrons as a consequence of the interaction between the incident electron beam and electrons bound in the solid. The second one is represented by the *cascade*, where the secondary electrons diffusing in the solid extract new secondary electrons generating a shower of electrons. As each secondary electron loses energy while traveling in the solid, the whole process proceeds until the energy of the secondary electron is no more sufficient to extract further secondary electrons or until it reaches the surface with enough energy to emerge. The number of the emitted secondary electrons divided by the number of the incident electrons is the so-called *secondary electron emission yield*. The secondary electron emission yield is measured as the integral of the secondary

electron energy distribution over the energy range from 0 to 50 eV. Secondary electron emission plays a fundamental role in scanning electron microscope imaging.

9.1 Secondary electron emission

Secondary electron emission from Polymethyl Methacrylate (PMMA), silicon dioxide (SiO_2), and aluminum oxide (Al_2O_3) will be modeled quantitatively using the Monte Carlo code. The chapter is aimed at comparing with the available experimental data the computational approaches described in the chapter devoted to the main features of the transport Monte Carlo modeling, i.e., the scheme based on the energy-straggling strategy and the method based on the continuous-slowing-down approximation. In such a way, it will be possible to understand the limits of validity of the methods and to face the question of the CPU time costs in evaluating which approach is more convenient in the various circumstances. We shall learn that the use of the simple continuous-slowing-down approximation allows getting an agreement with the experiment similar to that we can obtain with the more accurate (but CPU time-consuming) energy-straggling strategy. If, on the other hand, energy distribution of the secondary electrons is required, energy-straggling strategy becomes mandatory.

Secondary-electron emission involves very complex phenomena and a numerical treatment requires the detailed knowledge of the main interactions of the electrons with the solid target.

The most important processes that occur in the target are related to the production of individual electron transitions from the valence to the conduction band, to plasmon generation and to the elastic collisions with the screened potentials of the ions in the solids. If its energy is high enough, the electron can be subject to inelastic collisions with inner-shell electrons so that ionization occurs. Secondary electrons of very low energy also interact losing (and gaining) energy with phonons. In insulating materials, they can be trapped in the solid (polaronic effect). Each secondary electron can produce further secondary electrons during its travel inside the solid and, in order to obtain quantitative results, it is therefore mandatory to follow the whole cascade [19, 71, 89].

9.2 Monte Carlo approaches to the study of secondary electron emission

The Monte Carlo calculation of the secondary electron emission yield can be performed either taking into account all the details of the many mechanisms of the electron energy loss [19, 89, 67, 40] or assuming a continuous-slowing-down approximation [90, 91, 92]. The use of the first approach has stronger physical basis but, due to the detailed description of all the collisions in the secondary electron cascade, it corresponds to a scheme very time consuming. The continuous-slowing-down approximation represents instead an approach which saves a lot of CPU time. Its physical foundation is, on the other hand, more questionable.

We reports about the MC simulations of the secondary electron emission from PMMA, silicon dioxide and aluminum oxide (all insulating materials with many technological applications) obtained with the two approaches. It demonstrates that, if we limit ourselves to the calculation of the yield as a function of the primary energy, the two Monte Carlo schemes give equivalent results for any practical purposes.

The secondary electron yields calculated using the two approaches are very close. What is more, the two MC schemes give results in satisfactory agreement with the experiment. This means that, for the calculation of the secondary electron yield, the continuous-slowing-down approximation should be preferred, being much faster (more than ten times) than the more detailed scheme. If, on the other hand, secondary electron energy distributions are required, the continuous-slowing-down approximation cannot be used – for it is not able describe in a realistic way all the energy loss processes – and the detailed scheme becomes mandatory, even if it is much more CPU time consuming [73, 74].

9.3 Specific MC methodologies for SE studies

9.3.1 Continuous-slowing-down approximation

In the case of CSDA, as we know, the step length is calculated according to the equation $\Delta s = -\lambda_{\mathrm{el}} \ln \mu$ – where μ is a random number uniformly distributed in the range [0, 1] – while the energy loss ΔE along the segment of trajectory Δs is approximated by the equation $\Delta E = (dE/ds)\,\Delta s$. With

respect to the description we gave in the chapter devoted to the Monte Carlo method, the secondary electron yield calculation using CSDA requires a few further information.

The secondary electron yield is calculated, according to Dionne [93], Lin and Joy [90], Yasuda *et al.* [91], and Walker *et al.* [92] assuming that (i) the number dn of secondary electrons generated along each step length ds, corresponding to the energy loss dE, is given by

$$dn \;=\; \frac{1}{\epsilon_{\rm s}}\,\frac{dE}{ds}\,ds \;=\; \frac{dE}{\epsilon_{\rm s}} \tag{9.1}$$

where $\epsilon_{\rm s}$ is the effective energy necessary to generate a single secondary electron and (ii) the probability $P(z)$ that a secondary electron generated at depth z reach the surface and emerge from it follows the exponential decay law

$$P(z) \;=\; e^{-z/\lambda_{\rm s}}\;, \tag{9.2}$$

where $\lambda_{\rm s}$ is the *effective* escape depth. Thus the secondary electron emission yield is given by

$$\delta \;=\; \int P(z)\,dn \;=\; \frac{1}{\epsilon_{\rm s}}\int e^{-z/\lambda_{\rm s}}\,dE\;. \tag{9.3}$$

9.3.2 Energy-straggling

We have described in a previous chapter the details of the enegy straggling strategy, so that we shall just treat here the features of the scheme specific for the study of secondary electron emission. For further information about the adopted simulation methods, also see Ganachaud and Mokrani [19], Dapor *et al.* [40], and Dapor [73, 74].

If μ is a random number uniformly distributed in the interval [0, 1], every step length Δs of each electron traveling in the solid is calculated assuming the Poisson statistics, so that $\Delta s = -\lambda \ln \mu$. In this equation, λ is the electron mean free path including all the scattering mechanisms involved. Its reciprocal, i.e., the so-called inverse inelastic mean free path, can be expressed as the sum of all the inverse mean free paths of the interactions of the electrons with the target: in particular it is necessary to take into account the

inverse mean free path relative to the elastic interactions among the incident electrons and the screened atomic nuclei, $\lambda_{\rm el}^{-1}$, that relative to the inelastic interactions among the incident electrons and the atomic ones, $\lambda_{\rm inel}^{-1}$, that relative to the electron-phonon interactions, $\lambda_{\rm phonon}^{-1}$, and that relative to the electron-polaron interaction, $\lambda_{\rm pol}^{-1}$, so that $\lambda^{-1} = \lambda_{\rm el}^{-1} + \lambda_{\rm inel}^{-1} + \lambda_{\rm phonon}^{-1} + \lambda_{\rm pol}^{-1}$. Using random numbers one establishes the kind of collision. If the collision is inelastic, the energy loss is calculated according to the specific inelastic scattering cross-section (electron-electron, electron-phonon, or electron-polaron). If the collision is elastic, the scattering angle is calculated according to the Mott cross-section. Notice that electron deflection mainly depends on the elastic scattering cross-section but even electron-electron inelastic interactions and electron-phonon quasi-elastic interactions are responsible for electron change of direction. The present Monte Carlo scheme takes into account the entire cascade of secondary electrons [67, 71, 44, 40, 41, 42, 73, 74]. The initial position of a secondary electron due to Fermi sea excitation is assumed to be where the inelastic collision took place. In the calculations presented in this chapter, the polar and azimuth angles of secondary electrons are calculated, according to Shimizu and Ding Ze-Jun [13], assuming a random direction of the secondary electrons. This hypothesis of random direction of the generates secondary electrons corresponds to the idea that slow secondary electrons should be generated with spherical symmetry [13]. As this assumption violates momentum conservation rules – within the classical binary-collision model – a study will be provided (see section 10.4.1) which compares with experimental data the results obtained assuming spherical symmetry with those obtained assuming momentum conservation within the classical binary-collision model. This study demonstrate that the determination of the energy distribution of the secondary electrons emitted by solid targets as well as the secondary emission yield are in better agreement with the experiment assuming that slow secondary electrons are generated with spherical symmetry [67].

9.4 Secondary electron yield: PMMA, SiO_2, Al_2O_3

The MC schemes described above, i.e., the energy straggling (ES) and the continuous-slowing-down approximation (CSDA) methods, account for the

main interactions occurring to the secondary electrons along their travel in insulating targets [19]. In the following, results obtained with the two schemes will be presented and comparison with the available experimental data will be provided.

9.4.1 Comparison between ES scheme and experiment

Even if the physical meaning of the parameters appearing in the empirical laws describing the interactions is clear – so that they are, at least in principle, measurable – practically they can be determined only through an analysis of their influence on the simulated results and a comparison to the available experimental data.

Using such a kind of analysis, the values of the parameters for PMMA were determined and, in Fig. 9.1, we have reported the comparison with the available experimental data [91, 94, 95] of the simulated results obtained using the detailed Monte Carlo scheme based on the energy-straggling strategy (ES scheme). We found out, for PMMA, the best fit – using a least square fitting procedure – with the following values of the parameters: χ=1.0 eV, $W_{\rm ph}$=0.1 eV, C=0.15 Å^{-1}, and γ=0.14 eV^{-1} [40, 73]. Following a similar procedure we found out, for SiO_2, χ=0.9 eV, $W_{\rm ph}$=0.1 eV, C=0.1 Å^{-1}, γ=0.085 eV^{-1} [96]. Notice that, performing a similar analysis, Ganachaud and Mokrani found out, for amorphous Al_2O_3, the following values of the not a priori known parameters: χ=0.5 eV, $W_{\rm ph}$=0.1 eV, C=0.1 Å^{-1}, and γ=0.25 eV^{-1} [19]. Also note that the yield strongly depends on all these parameters. While both the electron affinity, χ, and the electron energy loss due to phonon creation, $W_{\rm ph}$, are quantities that have been measured for many materials and whose values can be found in the scientific literature, less information are available today concerning the two parameters C and γ (relative to the electron-polaron interaction).

9.4.2 Comparison between CSDA and ES schemes

The Monte Carlo code based on the continuous-slowing-down approximation scheme, also depends on two not a priori known parameters: the effective escape depth, λ_s, and the effective energy necessary to generate a single secondary electron, ϵ_s. Using the ES curve determined by the comparison with the experimental data presented in Fig. 9.1, it is possible to determine

the values of λ_s and ϵ_s of PMMA which correspond to the least square best fit. The procedure is described in Figs. 9.2 and 9.3.

In Fig. 9.2, in particular, the value of λ_s was set to 10.0 Å. The comparison between the CSDA and ES results is shown, with ϵ_s ranging from 6 eV to 9 eV. As the best value of ϵ_s is 7.5 eV, Fig. 9.3 reports the comparison corresponding to ϵ_s=7.5 eV and allowing λ_s to range between 5.0 Å and 15.0 Å.

9.4.3 Comparison between CSDA scheme and experiment

The comparisons of the results of the CSDA code to the available experimental data [94, 95, 97, 75, 98] for PMMA, SiO_2, and Al_2O_3 are shown in Figs. 9.4, 9.5, and 9.6, respectively.

The values of the parameters, reasonably in agreement with other physics reference data [19, 90], were determined in order to get the least square best fit of the results of the CSDA code to the experimental data. They are collected in Tab. 9.1. In Tabs. 9.2, 9.3, and 9.4, the calculated values of the statistical distribution χ_s^2, considered to quantitatively evaluate the agreement between the CSDA Monte Carlo simulated data (obtained using the parameters in Tab. 9.1) and the examined experimental data are reported, along with the number ν of degrees of freedom utilized for each comparison. We have also reported the lower critical values of the χ_s^2 distribution for any given ν along with the corresponding probability (p=0.99) of exceeding these critical values. As all the calculated χ_s^2 are significantly smaller than the critical ones, this means that, in the hypothesis that the Monte Carlo data approximate the experimental ones (the so-called null hypothesis), there is a probability greater than the 99% that the observed discrepancies are due to statistical fluctuations. Similar results were found out also comparing the experimental results to the ES Monte Carlo simulated data.

9.4.4 Secondary emission yield as a function of the energy

As the primary energy increases, the yield increases until a maximum is reached. Then the yield decreases by increasing the primary energy. Indeed, at very low primary energy, few secondary electrons are generated, and

increasing the primary energy the number of secondary electrons emerging from the surface increases.

Furthermore, at very low primary energy, the average depth at which the secondary electrons escaping from the surface are generated also increases as the primary energy increases. When the energy becomes higher than a threshold which depends on the target (the turning point for SiO_2 being approximately at 250 eV, according to the mean value between experiment and simulation), the average depth of generation of the secondary electrons becomes so deep that just a small amount of the generated secondary electrons are able to reach the surface satisfying the condition necessary to emerge from the sample and to be detected.

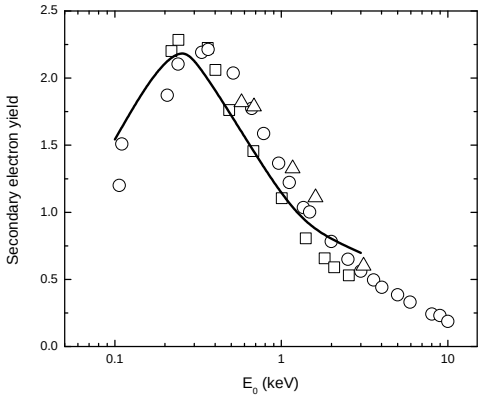

Figure 9.1: Comparison between present Monte Carlo calculations and experimental data of Polymethyl Methacrylate (PMMA) secondary electron yield as a function of the primary electron energy. Solid line represents Monte Carlo calculations based on the energy-straggling strategy and obtained with χ=1.0 eV, $W_{\rm ph}$=0.1 eV, C=0.15 Å^{-1}, and γ=0.14 eV^{-1}. Boxes are the Matskevich *et al.* experimental data, taken from Yasuda *et al.* [91]. Circles are the Boubaya and Blaise experimental data [94]. Triangles are the Rau *et al.* experimental data [95].

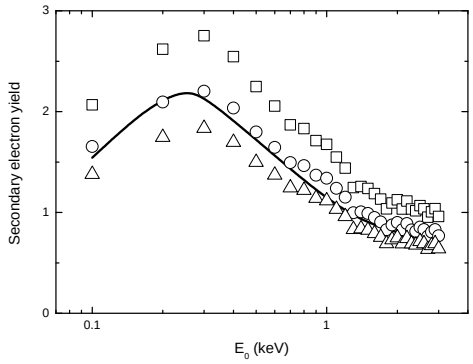

Figure 9.2: Comparison between present Monte Carlo calculations of PMMA secondary electron yield as a function of the primary electron energy. Solid line represents Monte Carlo calculations based on the energy-straggling strategy (see Fig. 9.1 for details). Symbols are Monte Carlo calculations based on the continuous-slowing-down approximation and obtained with λ_s=10.0 Å and ϵ_s=6.0 eV (squares), ϵ_s=7.5 eV (circles), ϵ_s=9.0 eV (triangles).

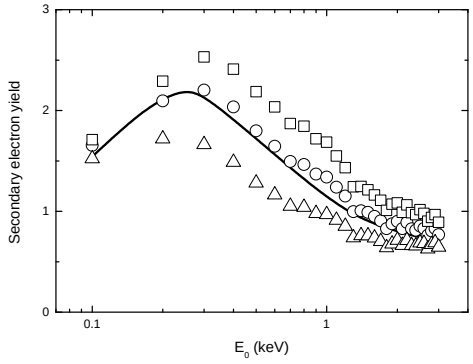

Figure 9.3: Comparison between present Monte Carlo calculations of PMMA secondary electron yield as a function of the primary electron energy. Solid line represents Monte Carlo calculations based on the energy-straggling strategy (see Fig. 9.1 for details). Symbols are Monte Carlo calculations based on the continuous-slowing-down approximation and obtained with ϵ_s=7.5 eV and λ_s=15.0 Å (squares), λ_s=10.0 Å (circles), λ_s=5.0 Å (triangles).

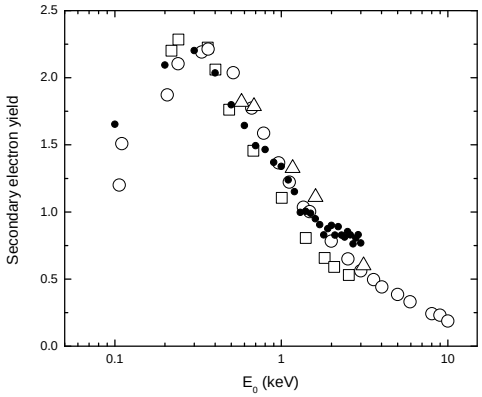

Figure 9.4: Comparison between present Monte Carlo calculations and experimental data of PMMA secondary electron yield as a function of the primary electron energy. Filled circles represent Monte Carlo calculations based on the continuous-slowing-down approximation and obtained with λ_s=10.0 Å and ϵ_s=7.5 eV. Empty boxes are the Matskevich *et al.* experimental data, taken from Yasuda *et al.* [91]. Empty circles are the Boubaya and Blaise experimental data [94]. Empty triangles are the Rau *et al.* experimental data [95].

Material	λ_s (Å)	ϵ_s (eV)
PMMA	10.0	7.5
SiO_2	5.0	12.0
Al_2O_3	15.0	6.0

Table 9.1: Values of the effective escape depth, λ_s, and of the effective energy necessary to generate a single secondary electron, ϵ_s, obtained in order to get the best fit of the Monte Carlo code, based on the continuous-slowing-down approximation, to the available experimental data concerning the secondary electron emission yield.

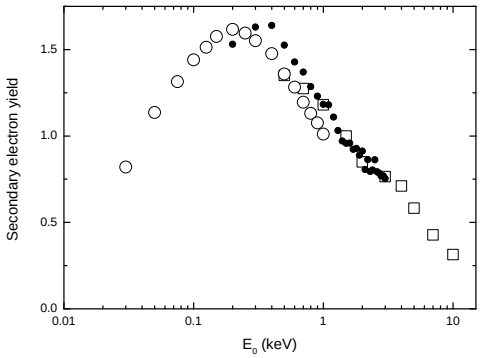

Figure 9.5: Comparison between present Monte Carlo calculations and experimental data of SiO_2 secondary electron yield as a function of the primary electron energy. Filled circles represent Monte Carlo calculations based on the continuous-slowing-down approximation and obtained with λ_s=5.0 Å and ϵ_s=12.0 eV. Empty circles are the Dionne experimental data [97]. Empty boxes are the Joy and Joy experimental data, taken from the Joys database [75].

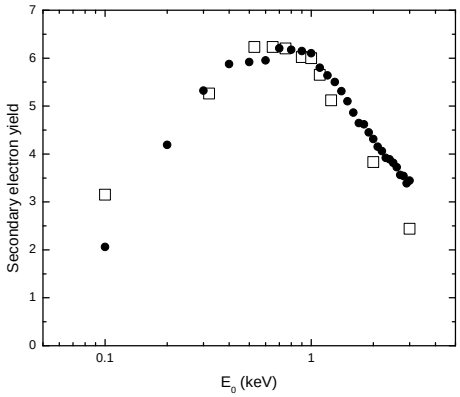

Figure 9.6: Comparison between present Monte Carlo calculations and experimental data of Al_2O_3 secondary electron yield as a function of the primary electron energy. Filled circles represent Monte Carlo calculations based on the continuous-slowing-down approximation and obtained with λ_s=15.0 Å and ϵ_s=6.0 eV. Empty boxes are the Dawson experimental data [98].

	χ^2_s (calculated)	ν	p	χ^2_s (critical value)
Matskevich *et al.* [91]	0.476	11	0.99	3.053
Boubaya and Blaise [94]	0.466	16	0.99	5.812
Rau *et al.* [95]	0.111	4	0.99	0.297

Table 9.2: PMMA: comparison between the calculated χ^2_s and the lower critical value of χ^2_s distribution corresponding to a probability of 99% for three sets of experimental data [91, 94, 95]. As the calculated χ^2_s is in all the cases significantly smaller than the lower critical value of the statitical χ^2_s distribution, the discrepancies between CSDA Monte Carlo data and experimental results can be attributed with high probability (greater than 99%) to statistical fluctuations, so that we can conclude that the CSDA Monte Carlo data corresponding to the parameters in Tab. 9.1 for PMMA very well approximate the considered experimental data.

	χ^2_s (calculated)	ν	p	χ^2_s (critical value)
Dionne [97]	0.0366	6	0.99	0.872
Joy and Joy [75]	0.164	11	0.99	3.053

Table 9.3: SiO_2: comparison between the calculated χ^2_s and the lower critical value of χ^2_s distribution corresponding to a probability of 99% for two sets of experimental data [97, 75]. As the calculated χ^2_s is in all the cases significantly smaller than the lower critical value of the statitical χ^2_s distribution, the discrepancies between CSDA Monte Carlo data and experimental results can be attributed with high probability (greater than 99%) to statistical fluctuations, so that we can conclude that the CSDA Monte Carlo data corresponding to the parameters in Tab. 9.1 for SiO_2 very well approximate the considered experimental data.

	χ^2_s (calculated)	ν	p	χ^2_s (critical value)
Dawson [98]	0.905	11	0.99	3.053

Table 9.4: Al_2O_3: comparison between the calculated χ^2_s and the lower critical value of χ^2_s distribution corresponding to a probability of 99% for a set of experimental data [98]. As the calculated χ^2_s is significantly smaller than the lower critical value of the statitical χ^2_s distribution, the discrepancies between CSDA Monte Carlo data and experimental results can be attributed with high probability (greater than 99%) to statistical fluctuations, so that we can conclude that the CSDA Monte Carlo data corresponding to the parameters in Tab. 9.1 for Al_2O_3 very well approximate the considered experimental data.

9.4.5 CPU time

The time of computation necessary to the ES code is much higher than the time of computation necessary to the CSDA code. For a typical simulation (1 keV electrons impinging on PMMA), the CSDA scheme is more than ten times faster than the ES one. The reason of this great difference in CPU time is related to the secondary electron cascade. The ES MC strategy requires that the entire cascade is followed. The CSDA MC code, on the other hand, is able to establish the number of secondary electrons produced at each step of every primary electron trajectory. Notice that a further advantage of the CSDA MC strategy is the reduced number of not *a priori* known physical parameters (only two against the four quantities required by the energy-straggling strategy).

Of course the ES MC code is based on a stronger physical background and allows one to calculate other important properties such as the secondary electron energy distribution and the lateral, angular, and depth distributions which are not accessible using the CSDA approximation.

The advantage in using the CSDA code, in practical terms, with respect to just performing an empirical fit to the experimental data is related, of course, to other predictive capabilities of the Monte Carlo simulations. If it is true that, at the moment, the CSDA model requires a fit to existing data or to the results of the detailed simulation to calculate its free parameters, one should take into account that if the parameters were known for a large

number of materials, they could be used for investigating many problems, different from the one we have used to find out the values of the parameters; such as, for example, the dependence of the secondary electron yield on the angle of incidence for any given primary energy, or the secondary electron emission from unsupported thin films (on both sides of the film), or the secondary electron emission yield from thin films deposited on bulk of different materials, and so on. Of course, all these possibilities are not accessible to a simple empirical fit to the experimental data.

In conclusion, the very fast CSDA MC code can be used for the calculation of the secondary electron yield. If secondary electron energy, lateral, and depth distributions, or detailed descriptions of the physics involved in the process are required, the ES MC strategy should be preferred, even if it requires much longer CPU time.

9.5 Linewidth measurement in critical dimension SEM

A very important application of the secondary electron yield MC calculations is related to nanometrology and linewidth measurement in critical dimension SEM [42, 99, 100, 101, 102]. In Refs. [41] and [42] we have recently investigated this problem using an approach based on the energy-straggling strategy, described above in this work, and on the detailed description of all the main mechanisms of scattering (elastic electron-atom, quasi-elastic electron-phonon, and inelastic electron-plasmon and electron-polaron interactions) [19, 40, 73]. The corresponding energy straggling Monte Carlo module has been included in the PENELOPE code [12], which provides benefits in term of 3D management and ray tracing capabilities. The original physics of PENELOPE [103, 104] has been completely replaced by the energy-straggling module described in this work with the aim to implement a simulation scheme working down to electron energies of 0.1 eV.

9.5.1 Nanometrology and linewidth measurement in CD SEM

In order to provide a metrics and to avoid yield loss in the most advanced CMOS technologies, critical dimensions (CD) measurements with sub-nanometer

uncertainty must be performed during the manufacturing process: this is the case, in particular, of the linewidth measurement of photoresist lines (e.g. PMMA) utilized in optical and electron beam lithography for device integration. In order to extract information about critical dimensions for accurate nanometrology in CMOS processes, modeling of the physics of image formation in scanning electron microscopy is required. Modern CD-SEM mainly operate at very low primary energies (down to 200 eV), and Monte Carlo simulation of the generation and transport of secondary electrons – generated by low primary energy electrons – is the most reliable method for extracting accurate results. The Monte Carlo scheme easily keeps track of the hundreds of secondary electrons that are generated per primary electron in a typical cascade process.

Typical structures of interest for CMOS technologies are dielectric lines (PMMA lines, for example) on silicon substrates with trapezoidal cross-section (see Figure 9.7). In SEM measurements with sub-nanometer uncertainty, the critical dimensions to be investigated are the bottom line width, the top line width, the slope of the rising edge, and the slope of the falling edge.

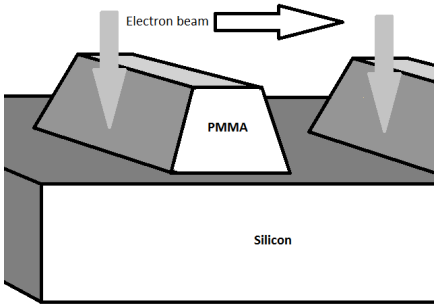

Figure 9.7: Dielectric material (e.g. PMMA) with trapezoidal cross-section on silicon substrate. Linescans are acquired perpendicularly to the structures.

9.5.2 Lateral and depth distributions

The lateral and depth resolutions of secondary electron imaging are related to the diffusion of the secondary electrons in the solid. Before proceeding, it seems therefore important to investigate the extent of lateral and depth distributions of the emerging electrons. Fig. 9.8 shows the lateral distribution of the secondary electrons emerging from PMMA, for a primary energy of 1000 eV, assuming a delta-shaped beam spot. Fig. 9.9 presents, for the same energy, the depth distribution of the sites where the secondary electrons that were able to emerge from the sample surface have originated. Both Figs. 9.8 and 9.9 together provide a general idea of the lateral and depth resolution which can be attained at a given primary energy. In accordance with the theoretical model, the lateral and depth distributions of emerging secondary electrons have a rather small and limited extent (less than ∼50 Å).

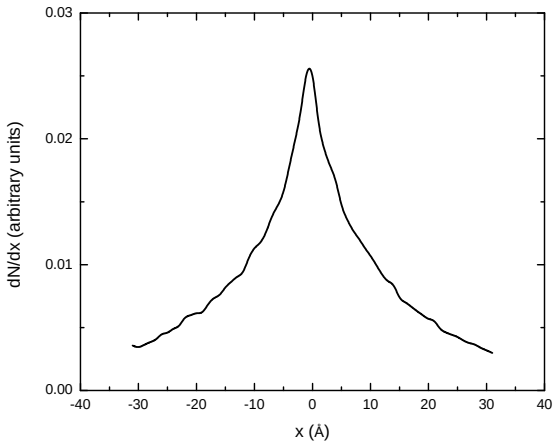

Figure 9.8: Present Monte Carlo calculation of the lateral distribution dN/dx of the secondary electrons emerging from PMMA. The electron primary energy E_0 was set to 1000 eV.

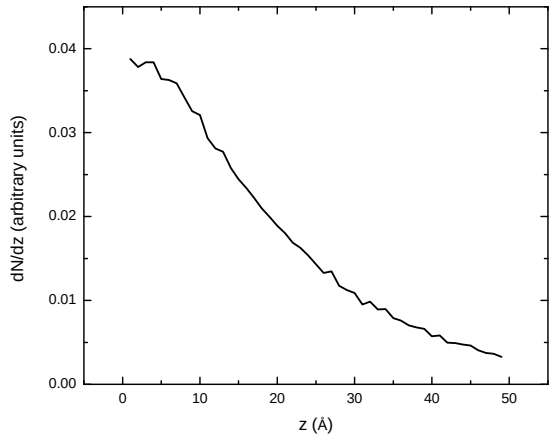

Figure 9.9: Present Monte Carlo calculation of the depth distribution dN/dz of the sites where the secondary electrons that were able to emerge from the PMMA sample surface have originated. The electron primary energy E_0 was set to 1000 eV.

9.5.3 Secondary electron yield as a function of the angle of incidence

Figure 9.10 shows the Monte Carlo simulation of the integral secondary electron yield of PMMA as a function of the angle of incidence α, with respect to the normal to the surface, for a primary energy of 300 eV, 1000 eV, and 3000 eV. The proposed Monte Carlo code predicts correctly the dependency both on the angle of incidence and on the primary energy. In fact, the depth of penetration into the sample of primary electrons impinging at grazing angles is quite small, turning into a reduced generation of secondary electrons. As α decreases, the secondary electron yield increases, due to the increase of the interaction volume in close vicinity of the surface of the sample. This applies until a critical angle is reached, where the secondary yield decreases due to the fact that the average generation depth of the secondary electrons increases resulting into a lower number of secondary electrons emerging from the surface. The turning point, as predicted by the Monte Carlo code for a primary energy of 300 eV, is at about 60°.

Figure 9.10 shows that, as the primary energy increases, the position of

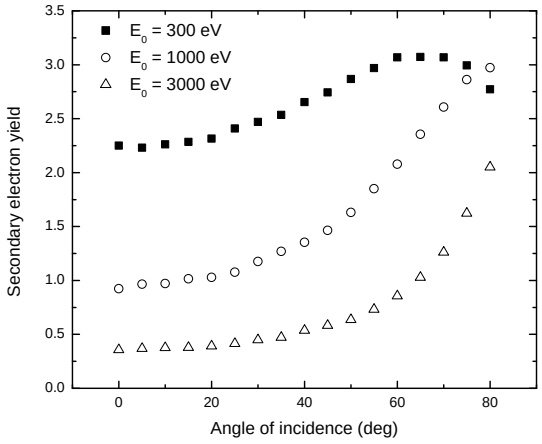

Figure 9.10: Present Monte Carlo calculation of the secondary electron yield of PMMA as a function of the angle of incidence α with respect to the normal to the surface. The electron primary energy E_0 was set to 300 eV (squares), 1000 eV (circles), and 3000 eV (triangles).

the maximum shifts toward higher angles, and eventually, when the primary energy becomes high enough (e.g., higher than 1000 eV), the maximum disappears and the function becomes monotonically increasing. The observed dependency on the primary energy is consistent with the results already reported in Joy [14]. In fact, in this publication, the secondary yield has been shown to decrease as the energy decreases and as the primary energy is less than 750 eV.

9.5.4 Linescan of a silicon step

The behavior of the secondary electron yield as a function of the angle of incidence discussed above, partially explains the shape of the line scans in secondary electron imaging performed on a given material through an edge of a step. Fig. 9.11 describes the situation for a single step in silicon.

The linescan signal presents the expected behavior. Far away from the step, where the surface is flat, the secondary electron emission yield corresponds to that of normal incidence. Approaching the step on the negative x positions, an increasing shadowing effect is observed. The reason of the

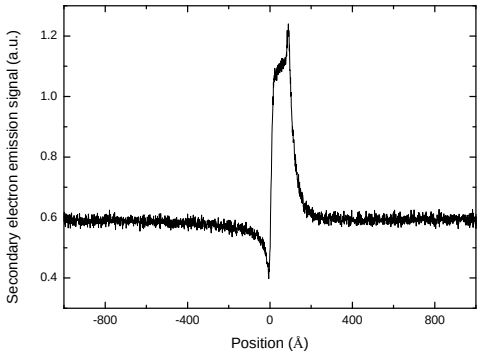

Figure 9.11: Present MC included in PENELOPE: simulation of a linescan from a silicon step with side wall angle equal to 10° and incident electron energy equal to 700 eV. The shape of the signal is determined by the angle of incidence of the primary electrons, their energy, positions of incidence, and geometry. The simulation has been performed by a pencil beam. Courtesy of Mauro Ciappa and Emre Ilgüsatiroglu, ETH, Zurich.

shadowing is the interception of the trajectories of the emerging secondary electrons by the step. At the step, the signal becomes discontinuous. At the bottom edge position, the emerging secondary electrons experience the maximum geometric shadowing, corresponding to the signal minimum. Close to the top edge, on the other hand, the generation and escape probabilities of the secondary electrons reach, for a pencil beam, their maximum values, so that the signal maximum is observed at top edge. An additional intermediate level within the transition can be noted in Fig. 9.11 whose value is, according to the Monte Carlo predictions for the secondary electron yield, a function of angle of incidence of the beam on the surface of the side wall.

9.5.5 Linescan of PMMA lines on a silicon substrate

Figure 9.12 shows linescans obtained by simulating three adjacent PMMA lines, respectively, on a silicon substrate. Adjacent structures cause additional geometry shadowing effects. This can be clearly seen from the outermost edges of the three lines. The outermost edges provide indeed the highest edge peak signal, corresponding to the step geometry case. The in-

ternal edge peak signals, on the other hand, are reduced due to additional shadowing effects produced by the neighbouring lines. Note that the yield levels depend on the individual yield levels of the materials involved in the shadowing process.

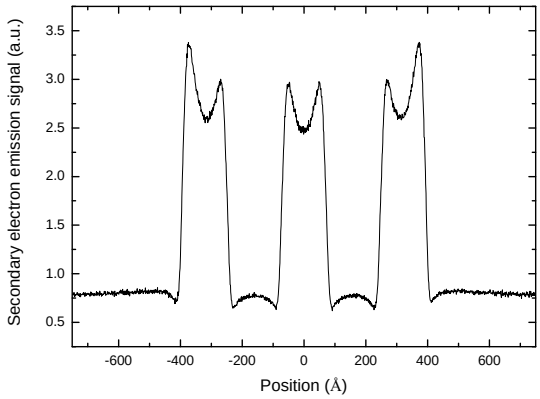

Figure 9.12: Present MC included in PENELOPE: simulation of a linescan from PMMA lines (height: 200 Å , bottom width: 160 Å , top width: 125 Å , side wall angle: 5°) on a Si substrate scanned with a pencil-like electron beam at 500 eV. Courtesy of Mauro Ciappa and Emre Ilgüsatiroglu, ETH, Zurich.

9.6 Concluding remarks about secondary electron yield

In this chapter the transport Monte Carlo method has been applied to the evaluation of the secondary electron emission from insulating materials (PMMA, SiO_2, and Al_2O_3) . The code has been validated by comparing the secondary electron yield obtained by Monte Carlo simulation to the available experimental data. In particular, an analysis of the results of two different approaches (energy-straggling scheme and continuous-slowing-down approximation scheme) for the determination of the yield of the secondary electrons emitted by insulating targets was presented. We have demonstrated that the two approaches give similar results concerning the secondary electron emission yield as a function of the electron primary energy. Furthermore

the simulated results are in good agreement with the available experimental data. Some fundamental aspects related to a possible use of the code for line width measurements by secondary electron imaging at very low primary beam energy have been discussed.

Chapter 10

Electron energy distributions

As we know, the study of the electronic and optical properties of the matter is paramount for our comprehension of physical and chemical processes which occur in nanoclusters and solids [105]. Radiation damage, investigation of chemical composition, and electronic structure study, represent a few examples of the role played by the electron-matter interaction mechanisms. Electron spectroscopy and electron microscopy are fundamental tools to examine how electrons interact with the matter [106].

Electron spectroscopy includes a wide range of techniques. Low energy reflection electron energy loss spectroscopy and Auger electron spectroscopy, in particular, uses electron beams to analyze the surface of materials.

Both reflection electron energy loss spectroscopy and Auger electron spectroscopy are applications of the scattering theory [107]. They are based on scattering processes in which the initial state consists of electrons impinging on solid-state targets, and final states are characterized by few non-interacting fragments. The analysis of the energy distribution of the fragments constitutes the main feature of these spectroscopies, as the energy distribution of the fragments provides insights about the properties of the examined system.

The spectrum, i.e., the plot of the intensity of the emitted electrons as a function of either the kinetic energy or the energy loss, represents a fingerprint of the investigated material.

10.1 Monte Carlo simulation of the spectrum

The numerical results we are going to present were obtained with a detailed modeling which takes into account all the described mechanisms of energy loss (electron-electron, electron-plasmon, electron-phonon, electron-polaron) and treats the elastic scattering events using the Mott cross-section. Furthermore, the entire cascade of secondary electrons is followed. The whole Monte Carlo spectrum representing the energy distribution of electrons emerging from a SiO_2 sample due to a 250 eV electron beam irradiation is presented in Fig. 10.1. Similar spectra have been observed for metals as well [76, 77]. For the present calculation the target is considered as semi-infinite. (Notice that the case of thin films requires special attention, in particular when the samples are thinner than the mean free path).

Many electrons of the primary electron beam can be backscattered, after having interacted with the atoms and electrons of the target. A fraction of them conserves the original kinetic energy, having suffered only elastic scattering collisions with the atoms of the target. We already know that these electrons constitute the so-called elastic peak, or zero-loss peak, whose maximum is located at the energy of the primary beam. In the simulation presented in Fig. 10.1 it is the narrow peak located at 250 eV.

The plasmon peak in Fig. 10.1, located at $\approx$227 eV, represents the electrons of the primary electron beam that emerge from the surface after having suffered a single inelastic collision with a plasmon. Multiple collisions with plasmons are also present in the spectrum, but they are of very low intensity so that they are not visible on this scale. In the following sections, this region of the spectrum will be expanded in order to study the shape of the plasmon losses for a few selected examples.

Electron-phonon energy losses are also not visible in Fig. 10.1, for (i) their intensities are much lower than that of the elastic peak and (ii) they are very close to the much more intense elastic peak whose width is, on the other hand, rather wide (of the order of 1 eV): then they are not resolved.

The spectrum includes also Auger electron peaks, due to the presence of doubly ionized atoms. They also are not visible on this scale. A zoom of an Auger peak (the oxygen K-LL Auger peak of the SiO_2 spectrum) with its background, obtained with an ab-initio method included in the present Monte Carlo code, will be shown in the following together with a comparison with experimental data.

In the end, as we already know, the secondary electrons produced by a

cascade process are those electrons which have been extracted from the atoms by inelastic electron-electron collisions and are able to emerge from the target surface. Their Monte Carlo energy distribution presents a pronounced peak in the very low energy region of the spectrum, typically below 50 eV, and it is clearly visible in the simulated spectrum in Fig. 10.1. Also the secondary electron energy distributions of selected materials will be presented in the following.

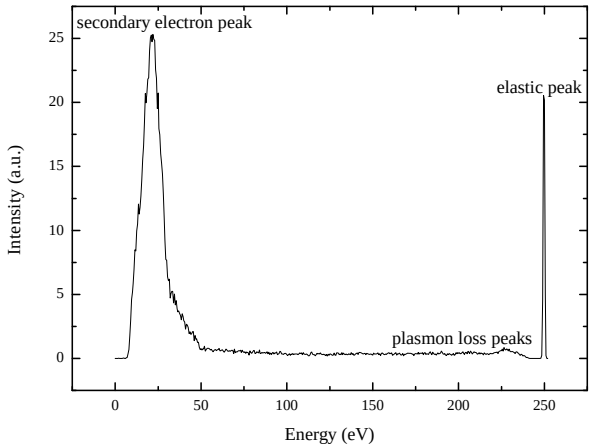

Figure 10.1: Present MC calculation of the spectrum representing the energy distribution of electrons emerging from a SiO_2 sample due to a 250 eV electron beam irradiation. The elastic peak, or zero loss peak, whose maximum is located at the energy of the primary beam, represents the electrons which suffered only elastic scattering collisions. The plasmon peak represents the electrons of the primary electron beam that emerge from the surface after having suffered a single inelastic collision with a plasmon. Multiple collisions with plasmons are also present in the spectrum, but they are of very low intensity so that they are not visible on this scale. The secondary electrons energy distribution presents a pronounced peak in the very low energy region of the spectrum, typically below 50 eV. χ=0.9 eV, $W_{\rm ph}$=0.1 eV, C=0.1 Å^{-1}, γ=0.085 eV^{-1} [96].

10.2 Plasmon losses

In order to present and briefly discuss the main features of the plasmon losses, a numerical simulation concerning SiO_2 will be firstly presented. In this particular case, use has been made of experimental data taken from the literature to calculate the dielectric function and, hence, the energy loss function [54, 55, 56]. Note that similar semi-empiric approaches to the calculation of the plasmon losses can be performed for other materials as well. In fact, experimental data concerning the energy loss function can be found in the literature for many materials. The case of carbon, for example, can be similarly treated using the experimental data in Refs. [108, 109, 110].

10.2.1 Plasmon losses in silicon dioxide

Let us now consider the Monte Carlo simulation of the SiO_2 electron energy-loss spectrum (see Fig. 10.2) when incident electron energy is given by E_0=2000 eV. For the present simulation, dielectric function utilized in the present calculation was taken by Buechner experimental data for energies lower than 33.6 eV [56] and obtained by the Henke *et al.* optical data for higher energies [54, 55].

The Monte Carlo simulated spectrum presents two plasmon loss peaks at ≈23 eV and at ≈46 eV corresponding, respectively, to to the single inelastic scattering and to the double inelastic scattering [111].

The main peak and its shoulders in the present calculations can be interpreted as interband transitions from the valence bands and the conduction band. The main peak at energy-loss at ≈23 eV and the shoulder located at ≈19 eV are attributed to excitations of the bonding bands, while the shoulders located at ≈15 eV and ≈13 eV are due to excitations of a nonbonding band [112].

In Fig. 10.2 an energy range is also shown, located between the main energy loss peak and the elastic peak, in which no backscattered electrons can be observed. Indeed, as the target is an insulator, electrons cannot transfer to the atomic electrons energies smaller than the value of the energy gap E_G between the valence and the conduction bands. As a consequence no electrons of the primary beam can emerge from the target surface with energy between $E_0 - E_G$ and E_0 (energy losses between 0 and E_G) [111].

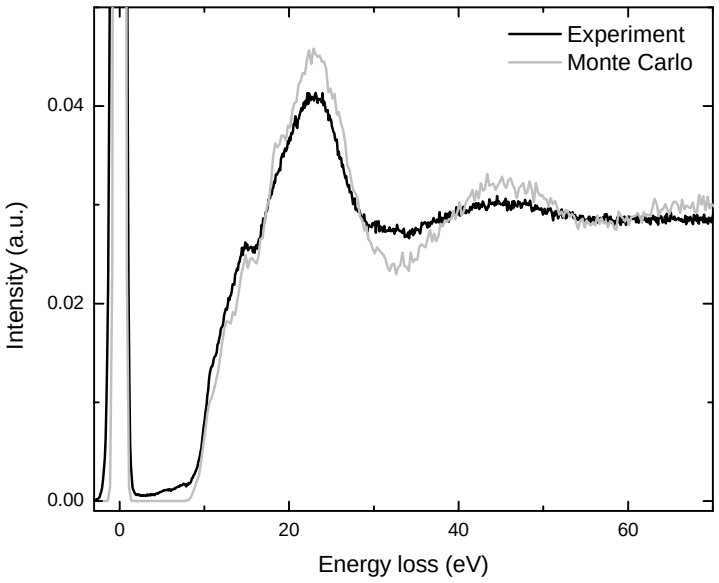

Figure 10.2: Experimental (black line) and present Monte Carlo simulated (gray line) energy-loss spectrum of 2000 eV electrons incident on SiO_2 [111]. The experimental and Monte Carlo spectra are normalized to a common area of the elastic peak. The optical data were taken from Henke *et al.* [54, 55], while the Buechner experimental energy loss function [56] was utilized for energies lower than 40 eV.

10.2.2 Bulk and surface plasmon losses: Werner *et al.* approximation

Electron energy loss spectroscopy for medium-low primary energy (lower than 2000 eV) has been extensively studied and it is well known that features due to surface plasmon excitations appear in spectra acquired either in reflection mode or in transmission mode from very thin samples (see, for example, Refs. [20, 10, 26, 113, 114]). On the other hand, quantitative applications of reflection electron energy loss spectroscopy are made difficult by the whole range of scattering events (elastic-inelastic, single-multiple, surface-bulk) contributing to the spectra, thus requiring reliable approaches to properly account for all contributions to electron backscattering.

We are here interested in investigating the interplay between surface and bulk features for incident electrons of variable energy. Electron energy, together with the angle of surface crossing, is in fact the main parameter affecting the relative intensity of surface and bulk excitations. Aluminum and silicon are chosen as case studies, because they exhibit well-resolved surface and bulk plasmon peaks [39].

We already know that, within the framework of the dielectric theory, the spectral response of a solid in inelastic scattering experiments is described by the energy loss function, which, in turn, depends on the dielectric function. Within the Drude-Lorentz model, and using the Ritchie and Howie [20] prescription to extend the optical case to non-zero momentum transfer, the dielectric function is given, as a function of the energy loss $\hbar\omega$ and the momentum transfer $\hbar\vec{k}$, by:

$$\varepsilon(\omega,\vec{k}) \;=\; 1 \;-\; \frac{\omega_P^2}{\omega^2-\omega_g^2-\omega_k^2-i\Gamma\omega}\;, \tag{10.1}$$

where $\hbar\omega_p$ is the plasma energy for a free electron gas and $\hbar\omega_g$ is the average excitation energy for valence electrons. We have chosen 0.0 eV for Al and 2.0 eV for Si. The damping coefficient $\hbar\Gamma$ is selected in order to get a reasonable agreement with the experimental width of the bulk plasmon peak (1.8 eV for Al, 3.7 eV for Si). The energy $\hbar\omega_k$ describes the momentum transfer dispersion relation and approaches the free particle limit for high values of the transferred momentum $\vec{k}$, calculated according to Ritchie and Howie [20].

For both Al and Si, the measured position of the bulk plasmon peak differs

from the position derived for a free electron gas, though for different reasons. For Al, the measured value, $\hbar\omega_p$=15 eV is smaller than the calculated one, $\hbar\omega_p$=15.8 eV, because the electron density in the surface region is reduced by sputter amorphization. To compare simulated and experimental spectra, we have therefore chosen $\hbar\omega_p$=15 eV in Eq. (10.1). For Si, the measured value, $\hbar\omega_p$=16.9 eV, is slightly greater than the calculated one, $\hbar\omega_p$=16.6 eV, due to a combination of factors acting in different directions (the electron density reduced by sputter amorphization in the surface region would decrease the energy of the plasmon peak, while the presence of a non-zero band-gap would increase it). The value $\hbar\omega_g$=2 eV was chosen in order to reproduce the measured bulk peak position in the simulated spectrum.

Bulk $f_B(\omega,\vec{k})$ and surface $f_S(\omega,\vec{k})$ energy loss functions, describing bulk and surface plasmon peaks, are given, respectively, by [22]:

$$f_B(\omega,\vec{k}) \;=\; \mathrm{Im}\left[\frac{1}{\varepsilon(\omega,\vec{k})}\right] \,, \tag{10.2}$$

$$f_S(\omega,\vec{k}) \;=\; \mathrm{Im}\left[\frac{1}{\varepsilon(\omega,\vec{k}) \;+\; 1}\right] \,. \tag{10.3}$$

We know that the differential inverse inelastic mean free path (DIIMFP) can be obtained from f_B integrating, over the momentum transfer k, the function $f_B/(\pi E a_0 k)$ (see Eqs. (4.21) and (4.22)). In turn, integration of the DIIMFP over all possible energy losses results in the inverse inelastic mean free path (IIMFP, i.e., the probability for bulk excitations), while integration of the DIIMFP up to a given energy loss (divided by the IIMFP) results in the probability distribution function for bulk excitations [36]:

$$P(W,E) \;=\; \frac{\int_0^W \mathrm{DIIMFP}(w,E)\,dw}{\mathrm{IIMFP}(E)} \,, \tag{10.4}$$

where E is the incident electron energy and W the electron energy loss. $P(W,E)$ is used to sample the energy loss in each bulk inelastic collision, hence it determines the shape of the bulk plasmon peak.

Similarly, integrating the properly weighted function f_S over the momentum provides us with the differential surface excitation probability (DSEP) accounting for surface plasmon excitation [113, 115]. Integrating the differential surface excitation probability [divided by the surface excitation probability (SEP)] up to a given energy loss, we obtained the probability distribution

function for surface plasmon excitation, used to sample the energy loss for each surface inelastic collision, and hence determining the shape of the surface plasmon peak.

The total surface excitation probability was obtained using the semi-empiric expression proposed by Werner [113] for the average number of excitations in a single surface crossing:

$$n_s = \frac{1}{1 + a_s \cos\alpha\sqrt{E}} . \tag{10.5}$$

Here α is the polar angle of surface crossing and a_s is a parameter depending on the target atomic number that can be found, for many elements, in Ref. [33].

Thus, while the probability for bulk excitations is ruled by the IIMFP, the probability for surface excitations is ruled by n_s: whenever an electron crosses the surface, we assign it probability n_s to excite a surface plasmon. Then, the particular approach taken here to model surface effects consists in ruling the surface to bulk plasmon ratio via the empirical SEP, Eq. (10.5), on the one hand and the bulk IIMFP on the other hand. The energy and shape of surface and bulk plasmon losses are obtained by the respective differential functions, i.e., the DSEP and the DIIMFP.

Figs. 10.3 and 10.4 show the comparison between experimental and MC simulated data for aluminum and silicon, respectively (E_0=2000 eV). The spectra are normalized to a common area of the zero loss peak. The data have been presented as a function of the energy loss. The range of energy loss have been selected in order to include both the first and the second plasmon loss peaks. We see that the intensity of the energy loss features with respect to the zero loss peak is not far from the experimental results, though with some overestimation, especially in the bulk plasmon. The surface plasmon loss peaks are located at an energy $\hbar\omega_p$ which is, approximately, given by $\hbar\omega_s \approx \hbar\omega_p/\sqrt{2}$ (10.6 eV for Al, 12.0 eV for Si). In spite of the simplified model taken here to account for surface effects, the relative intensity between surface and bulk features is reasonably well described (see, for further details, see Dapor *et al.* [39]).

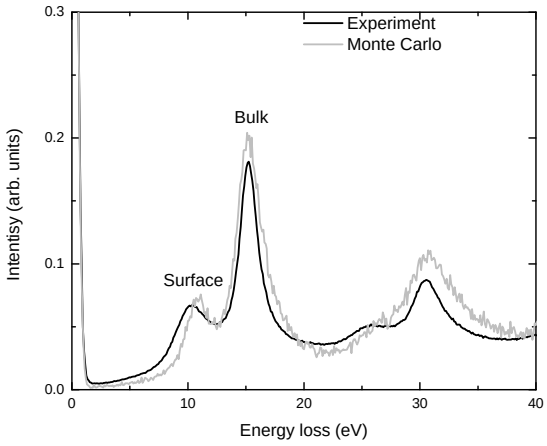

Figure 10.3: Experimental (black line) and present MC simulated (gray line) Al REEL spectra excited by 2000 eV electrons [39]. The MC code is based on the Werner approximation [113], Eq. (10.5). The spectra are normalized to a common area of the zero loss peak.

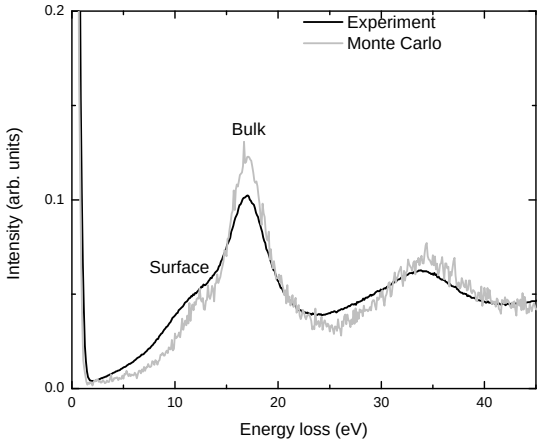

Figure 10.4: Experimental (black line) and present MC simulated (gray line) Si REEL spectra excited by 2000 eV electrons [39]. The MC code is based on the Werner approximation [113], Eq. (10.5). The spectra are normalized to a common area of the zero loss peak.

10.2.3 Bulk and surface plasmon losses: Chen and Kwei theory

Another approach to calculate the energy dependence of the interplay between surface and bulk features for incident electrons of variable energy has been proposed by Chen and Kwei [27] for outgoing projectiles. The theory was generalized by Li *et al.* [28] for incoming projectiles. See appendix D for details about the Chen and Kwei theory and about the Li *et al.* generalization. The application of the Chen and Kwei theory to the calculation of the plasmon loss spectra of Al and Si – assuming a V-type trajectory modeling [116] (i.e., under the hypothesis that the spectra arise from electrons undergoing a single large angle elastic scattering event) – has been recently proposed by Dapor *et al.* [72].

Chen and Kwei theory with V-type trajectory

We have shown in the previous section that Werner approximation gives a good description of the bulk and surface plasmon peaks when the kinetic energy of the incident electrons is 2000 eV. When the kinetic energy of the incident electrons is lower than 2000 eV, other approaches are required. Surface to bulk plasmon intensity ratio depends on the primary kinetic electron energy. In order to study the dependence of the bulk to surface plasmon losses intensity ratio on the primary energy, we introduce a numerical modeling based on the Chen and Kwei theory [27, 28] and on the assumption that spectra arise from electrons undergoing a single large angle elastic scattering event [72] (so-called V-type trajectories [116]). We focus on understanding the behavior of the bulk and surface plasmon loss intensities as the primary electron energy changes. To this end, spectra measured at various energies are compared to calculated spectra. Inelastic scattering is described by the Chen and Kwei differential inverse inelastic mean free path, dependent on the distance from the surface (in the solid and in the vacuum) and on the angle of surface crossing.

Chen and Kwei used the dielectric theory to show that the differential inverse inelastic mean free path for electrons emerging from a solid surface can be split up into two terms. The first one is the differential inverse inelastic mean free path in an infinite medium. The second one is the so-called surface term which is related to a surface layer extending on both sides of the vacuum-solid interface. As a consequence electrons can interact inelasti-

cally with the solid even if outside, if close enough to the surface. Spectra of electrons originating near to the surface are therefore influenced by these surface effects.

Using the Chen and Kwei theory, one can calculate the dependence on z of the inverse inelastic mean free path, for any given electron kinetic energy. In Figs. 10.5 and 10.6 the inverse inelastic mean free path of Al and Si, respectively, are presented as a function of the electron energy and depth (both outside and inside the solid). Notice that the theory predicts different trends for the IIMFP for electrons incoming and outgoing, in particular when electrons are close to the surface: in particular the inverse inelastic mean free path of the incoming electrons is found to slightly oscillate around the mean value, i.e., the bulk inverse inelastic mean free path. This phenomenon is attributed to the behavior of the electrons passing through the surface.

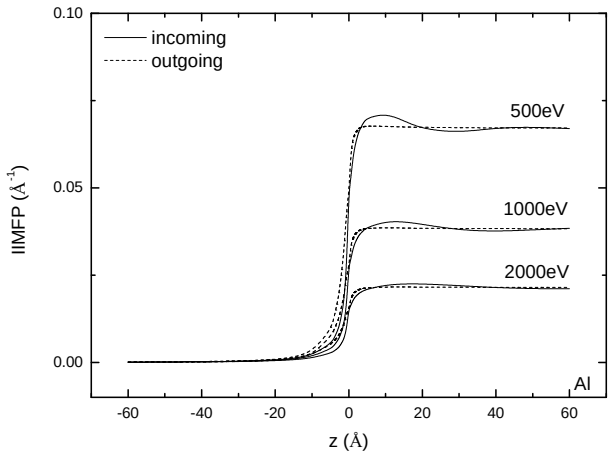

Figure 10.5: Inverse inelastic mean free path (IIMFP) electrons in Al as a function of the distance from the surface (in the solid and in the vacuum) for several kinetic energies of both the incoming and outgoing electrons. Present calculation.

In the calculations, the angles of surface crossing are $\alpha = \alpha_{\rm in}$ for incoming electrons and the average of $\alpha = \alpha_{\rm out}$ over the azimuth for outgoing electrons. Spectra are computed by integrating over z functions $P_{\rm outside}$ and $P_{\rm inside}$ representing the DIIMFP outside and inside the material, respectively

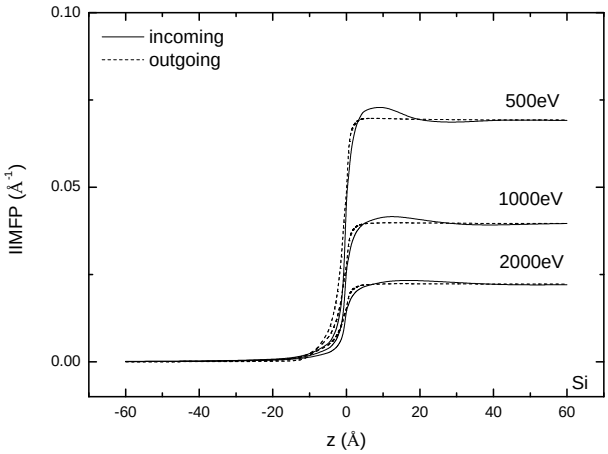

Figure 10.6: Inverse inelastic mean free path (IIMFP) electrons in Si as a function of the distance from the surface (in the solid and in the vacuum) for several kinetic energies of both the incoming and outgoing electrons. Present calculation.

(see appendix D for details of calculation of the DIIMFPs in the Chen and Kwei theory).

The surface is located at $z = 0$ Å and z is positive inside the material. For outside electrons (incoming and outgoing), we integrate from $z = 0$ Å up to -15 Å. Beyond this value, $P_{\rm outside}$ becomes very small and can be safely neglected. For inside electrons (incoming and outgoing), we integrate from 0 Å up to $z_{\rm max}$, where $z_{\rm max}$ results from a V-type trajectory [116, 117] of total length λ_V, i.e.,:

$$\lambda_{\rm V} \;=\; z_{\rm max}\left(\frac{1}{\cos\alpha_{\rm in}}+\frac{1}{\cos\alpha_{\rm out}}\right)\,. \tag{10.6}$$

In this eqaution, $\lambda_{\rm V}$ is given by:

$$\lambda_{\rm V}^{-1} \;=\; \lambda_{\rm inel}^{-1} \;+\; \lambda_{\rm tr}^{-1}\,, \tag{10.7}$$

where $\lambda_{\rm inel}$ is the electron inelastic mean free path (Ritchie theory [17, 20, 24, 26, 25]) and $\lambda_{\rm tr}$ is the transport mean free path (Mott theory [16, 48]).

Z	E (eV)	λ_V (Å)
13	500	9.5
13	1000	17.2
13	2000	31.4
14	500	11.6
14	1000	21.0
14	2000	38.7

Table 10.1: λ_V as a function of energy for Al and Si in the electron energy range 500-2000 eV.

Values of λ_V depend on the electron energy and on the target atomic number. In Tab. 10.1 selected values of λ_V in the electron energy range 500-2000 eV for Al and Si are shown.

In Figs. 10.7 to 10.11, our calculations for Al and Si are compared to experimental data for 500, 1000 and 2000 eV electron energies. After linear background subtraction, calculated and experimental spectra were normalized to a common height of the bulk plasmon peak. No free parameters were included in the calculation, the value of z_{max} being given by the Tanuma *et al.* inelastic mean free paths [60] and the Mayol and Salvat transport mean free paths [118], as described above (see Eqs. (10.6) and (10.7)). The agreement between theory and experiment is good and, in particular, the change in the relative intensities of surface and bulk plasmons as a function of electron energy is very well described [72].

It thus seems that combining the Chen and Kwei theory [27] with a single V-type trajectory modeling gives excellent results, at least in the electron energy range investigated here. On the other hand, the limit of the present calculation is that it requires linear background subtraction and normalization to a common height of the bulk plasmon peak. Furthermore multiple scattering peaks are not described by the theory. The inclusion of the Chen and Kwei theory in the Monte Carlo code should solve all these problems, while maintaining the proven accuracy of the description of changes in the line shape of the plasmonic peaks. We shall show that the Monte Carlo realistic description of all the electron-matter interactions will avoid the background subtraction and the normalization to a common height of the bulk plasmon

peak. Furthermore it will be able to predict the behavior of the multiple inelastic scattering processes. This will be the subject of the next section, which we have dedicated to the inclusion of the Chen and Kwei theory in the Monte Carlo modeling.

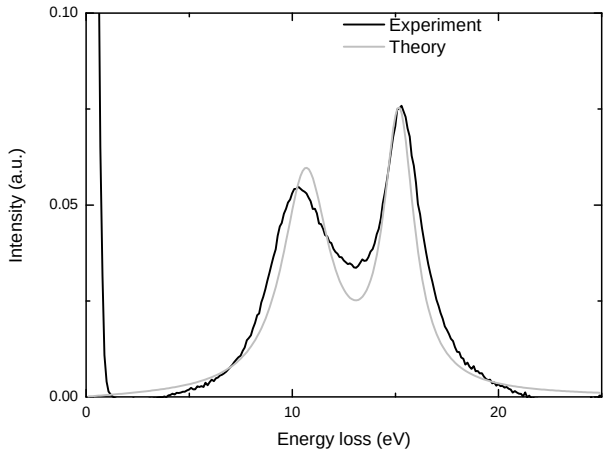

Figure 10.7: Comparison between the experimental (black line) and the present theoretical calculation (gray line) of electron energy loss spectra for 500 eV electrons impinging on Al [72].

Chen and Kwei theory included in the Monte Carlo code

The main feature of the theory of Chen and Kwei is represented by the fact that the inelastic scattering depends on the distance from the surface (in the solid and in vacuum) and on the angle of surface crossing (see Figs. 10.5 and 10.6). The consequence is that, in the Monte Carlo simulation, the sampling of the energy loss previously discussed (see Fig. 6.2) is no longer sufficient if we wish to describe the surface phenomena. Cumulative probabilities for inelastic collisions of electrons have to be calculated not only as a function of the energy loss W but also as a function of the distance from the surface. Furthermore, since in the Chen and Kwei theory also the vacuum (close to the surface) contributes to inelastic scattering, cumulative probabilities have to be calculated in the vacuum as well. In Fig. 10.13 the cumulative

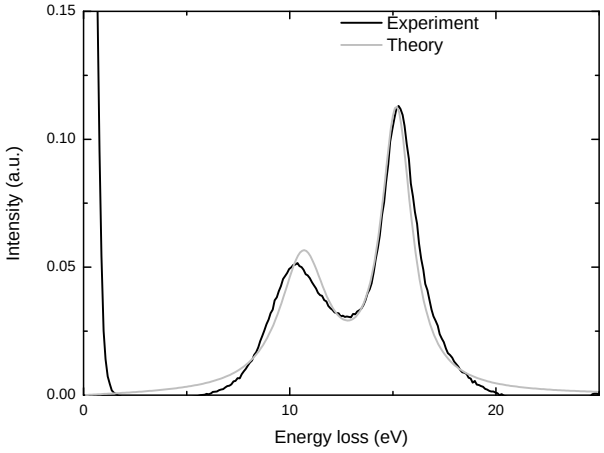

Figure 10.8: Comparison between the experimental (black line) and the present theoretical calculation (gray line) of electron energy loss spectra for 1000 eV electrons impinging on Al [72].

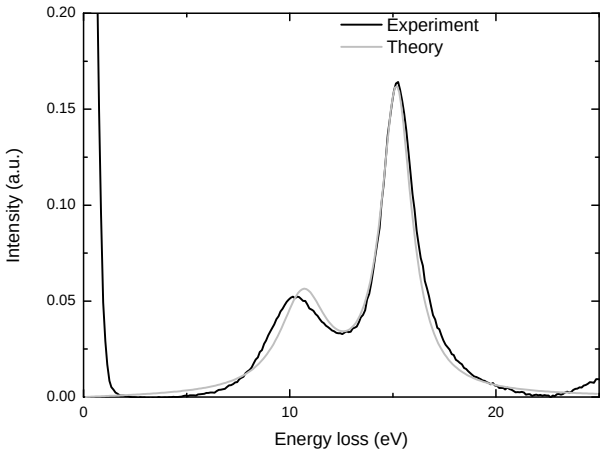

Figure 10.9: Comparison between the experimental (black line) and the present theoretical calculation (gray line) of electron energy loss spectra for 2000 eV electrons impinging on Al [72].

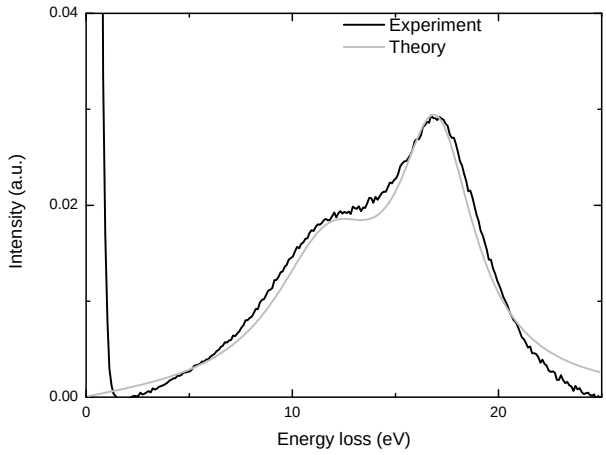

Figure 10.10: Comparison between the experimental (black line) and the present theoretical calculation (gray line) of electron energy loss spectra for 500 eV electrons impinging on Si [72].

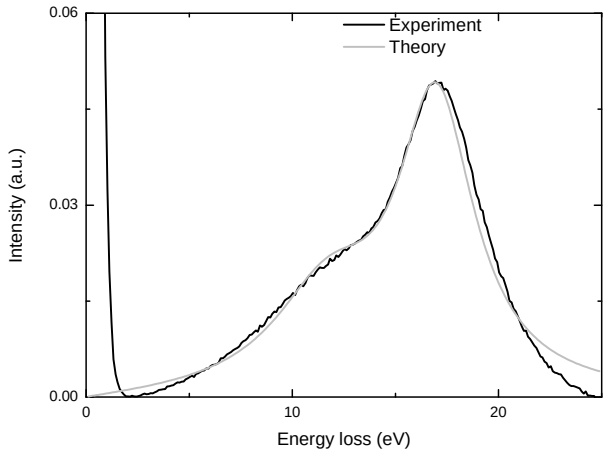

Figure 10.11: Comparison between the experimental (black line) and the present theoretical calculation (gray line) of electron energy loss spectra for 1000 eV electrons impinging on Si [72].

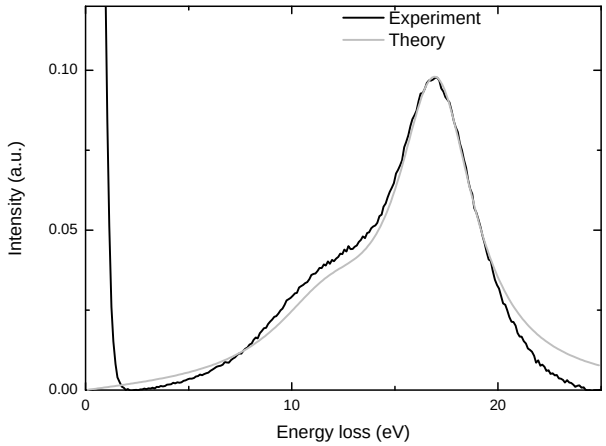

Figure 10.12: Comparison between the experimental (black line) and the present theoretical calculation (gray line) of electron energy loss spectra for 2000 eV electrons impinging on Si [72].

probability for inelastic collisions of electrons in Si is represented as a function of the energy loss for few selected distances from the surface – for the case of incoming electrons inside the solid. In order to simulate the spectra that we shall present in this section, similar curves have been calculated for incoming electrons outside the solid, outgoing electrons inside the solid, and outgoing electrons outside the solid. Notice that, as z approaches ∞, the curves presented in Fig. 10.13 approach the "bulk" curve in Fig. 6.2.

In order to include in the Monte Carlo code the Chen and Kwei theory, or any other theory which takes into account that the electron inelastic mean free path explicitly depends on z, also the sampling procedure for the electron length between the successive scattering events – that we described in the chapter devoted to the Monte Carlo method – has to be accordingly modified. According to Ding and Shimizu [31] and Ding *et al.* [31], let us assume that the distribution function, $p_\chi(s)$, has the form:

$$p_\chi(s) = \frac{1}{\lambda(s)} \exp\left[-\int_0^s \frac{ds'}{\lambda(s')}\right] , \tag{10.8}$$

For a comparison, see Eq. (5.7) where λ was assumed to be independent of

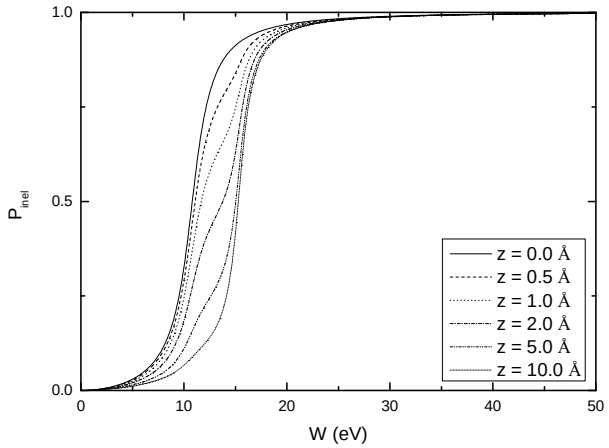

Figure 10.13: Sampling of the energy loss for electrons in silicon. $P_{\rm inel}$ is the present calculation of the cumulative probability for inelastic collisions of electrons in Si (calculated according to the Chen and Kwei theory [27]) causing energy losses less than or equal to W. The cumulative probability is represented as a function of the energy loss for few selected distances from the surface for the case of incoming electrons inside the solid. Similar curves have been calculated for incoming electrons outside the solid, outgoing electrons inside the solid, and outgoing electrons outside the solid. E_0=1000 eV. See also, for a comparison, Fig. 6.2.

the depth.

Since this equation is difficult to solve in practice, according to Ding and Shimizu [31] the following procedure can be followed to calculate z. The first step is to put $z = z_{\rm i}$, where $z_{\rm i}$ is the z component of the electron present position. If $\lambda_{\rm min}$ represents the minimum value of the mean free path (the inelastic one when the particle is in vacuum and, when it is in the material, calculated taking also into account the elastic mean free path), the second step is constituted by the generation of two independent random numbers, μ_1 and μ_2, uniformly distributed in the range [0, 1], and in calculating a new value of z by the equation:

$$z = z_{\rm i} - \cos\theta \, \lambda_{\rm min} \ln \mu_1 \, . \tag{10.9}$$

If $\mu_2 \leq \lambda_{\rm min}/\lambda$, then the new value of z is accepted; else we put $z = z_{\rm i}$ (i.e., z is now considered as the new z component of the inital position), two new random numbers μ_1 and μ_2 are generated, and a new value of z is calculated according to Eq. (10.9).

The comparison between experimental and MC simulated data is shown for 500, 1000, and 2000 eV electron energies in Figs. 10.14-10.16 for Al and in Figs. 10.17-10.19 for Si. The spectra are normalized to a common area of the zero loss peak and presented as a function of the energy loss. The Monte Carlo results are directly compared to the experimental data: nor background subtraction neither normalization to a common height of the bulk plasmon peak were needed for the comparison. The range of energy loss have been selected in order to include both the first and the second plasmon loss peaks. We see that the intensity of the energy loss features with respect to the zero loss peak is in good agreement to the experimental results. Also the observed increase of the surface to bulk ratio of the plasmon loss peaks as the energy decreases is well reproduced by the simulation.

A slight discrepance can be observed in the shape of the peaks: indeed while the experimental shape of the peaks is not symmetric, the Monte Carlo simulated data are quite symmetric. To understand the discrepancy in the shape of the plasmon peaks, we should notice that dispersion is neglected in the Chen and Kwei theory and, as a consequence, in the present Monte Carlo calculation as well. It is clear that the shape of simulated spectra depends on whether dispersion is taken into account or not. Dispersion is known to cause a slight displacement of peaks to high loss energy and, above

all, the appearance of a tail at high loss energy. Figs. 10.14-10.19 show that the region on the high energy side of loss peaks is exactly where the major disagreement between experimental and simulated spectra occurs. It is thus clear that a theory which includes dispersion is needed if the asymmetric experimental spectra have to be properly reproduced.

The Werner approximation described above allows to the Monte Carlo code to take into account dispersion, providing as a consequence a better description of the asymmetric shape of the peak (see Figs. 10.3-10.4 for the case of 2000 eV).

Chen and Kwei theory is based on a strong physical background and very well describes the energy dependence of the surface to bulk intensity ratio of the plasmon peaks, so that an improved version of the Chen and Kwei theory also able to properly take into account spatial dispersion should be very useful. An excellent review and discussion about this topics – applied to multi-walled carbon nanotubes – has been recently provided by Kyriakou *et al.* [114] .

In conclusion, we found that using a depth-dependent DIIMFP enables us to accurately describe the relative intensity of surface and bulk losses in REEL spectra. The agreement between Monte Carlo ad experimental data is very good in the electron energy range from 500 to 2000 eV, even if the Chen and Kwei theory – neglecting dispersion and using a local dielectric function $\varepsilon(\omega)$ to compute the response of the material – cannot reproduce the observed asymmetry of the peaks. A better description of the line-shape of loss peaks requires that dispersion (neglected in the Chen and Kwei theory) be included in the model [114].

10.3 Energy losses of Auger electrons

The present Monte Carlo code can be used to model the energy losses occuring to the Auger electrons during their travel in the solid – before emerging from the surface. In this context, the Monte Carlo code can be used to calculate the changes caused to the original electron energy distribution by energy losses suffered by the Auger electron on its way out of the solid. The original electron distribution was calculated using *ab initio* calculations of non-radiative decay spectra obtained by the program suite *SURface PhotoelectRon and Inner Shell Electron Spectroscopy* (SURPRISES). The physics of SURPRISES can be found in Refs. [34, 35, 36]. It is a program which

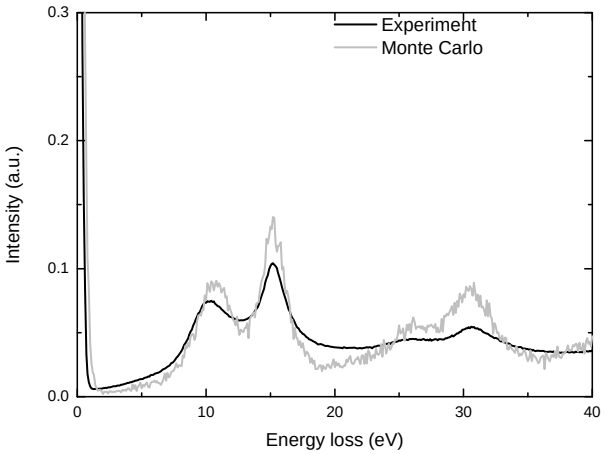

Figure 10.14: Comparison between the experimental (black line) and the present Monte Carlo (gray line) electron energy loss spectra for 500 eV electrons impinging on Al. The spectra are normalized to a common area of the zero loss peak.

performs *ab initio* calculations of photoionization and non-radiative decay spectra in nanoclusters and solid state systems.

The comparison between simulated and experimental Auger spectra requires to properly take into account the changes caused, to the Auger electron energy distribution, by the energy losses which the Auger electrons suffer along their travel in the solid toward the surface. Do to that, we use previously calculated *ab initio* Auger probability distribution as a source of electrons suffering inelastic processes. The theoretical Auger spectrum previously calculated using *ab initio* calculations is assumed to describe the initial energy distribution of the escaping electrons.

Auger electron generation is calculated assuming a constant depth distribution whose thickness, according to Ref. [119], was set to 40 Å. A plot of the calculation compared to the original experimental data – i.e., the experimental data presented without any deconvolution of energy losses – is given in Fig. 10.20. The original theoretical spectrum (*ab initio* calculation) is also provided.

One can see that the Monte Carlo energy loss calculation increases and

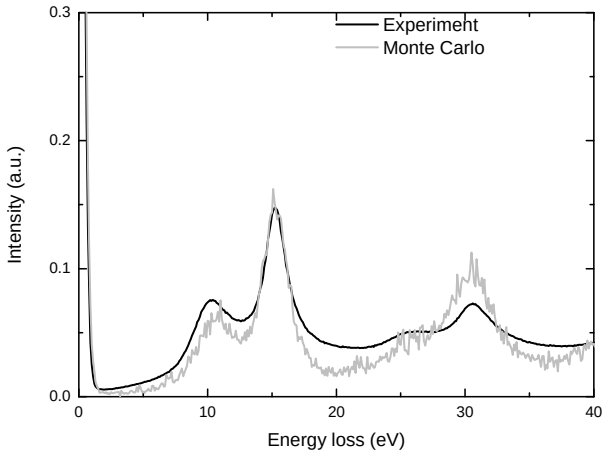

Figure 10.15: Comparison between the experimental (black line) and the present Monte Carlo (gray line) electron energy loss spectra for 1000 eV electrons impinging on Al. The spectra are normalized to a common area of the zero loss peak.

broadens the Auger probability. The large broadening of the K-L_1L_{23} peak after Monte Carlo treatment is due to the main plasmon of SiO_2 whose distance from the zero loss peak ($\approx$23 eV: see Fig. 10.2) is the same as the distance between the K-$L_{23}L_{23}$ and K-L_1L_{23} features in the Auger spectrum.

A satisfactory agreement between the experiment and the combination of the *ab initio* calculation with the Monte Carlo simulation can be found: in particular a good accordance can be recognized in the energy position, in the relative intensities of the peaks, and in the background contribution over the entire investigated energy range.

10.4 Secondary electron spectrum

Another important feature of the electron energy spectrum is represented by the secondary-electron emission distribution, i.e., the energy distribution of those electrons which, once extracted from the atoms by inelastic collisions and having travelled in the solid, reach the surface with the energy sufficient to emerge. The energy distribution of the secondary electrons is confined in

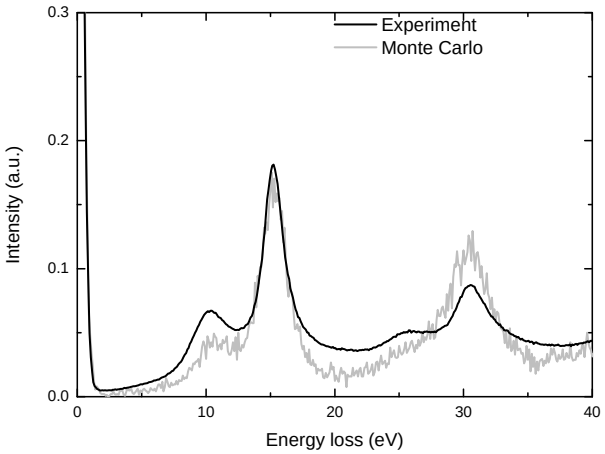

Figure 10.16: Comparison between the experimental (black line) and the present Monte Carlo (gray line) electron energy loss spectra for 2000 eV electrons impinging on Al. The spectra are normalized to a common area of the zero loss peak.

the low energy region of the spectrum, typically well below 50 eV. A very pronounced peak characterizes it, which is due to a cascade process in which every secondary electron generates, along its trajectory, further secondary electrons, so that a kind of shower of secondary electrons is created.

The first question is whether secondary electrons due to Fermi sea excitations are generated with spherical symmetry – violating in such a case momentum conservation – or if they are emitted conserving the momentum, as prescribed by the classical binary-collision theory (see section 6.2.3). Since the energy distributions resulting from these two processes are different, two versions of the Monte Carlo code were considered. One of the two versions assumes spherical symmetry for the angular distribution of the secondary electron emission at the site of generation, while the other one is based on the assumption of momentum conservation. The results of the two Monte Carlo codes will be compared to experimental data, in order to decide which one better describes the phenomena. We shall show that the hypothesis of spherical symmetry provides results in better agreement with the experimental evidences than that of momentum conservation. This is in agreement

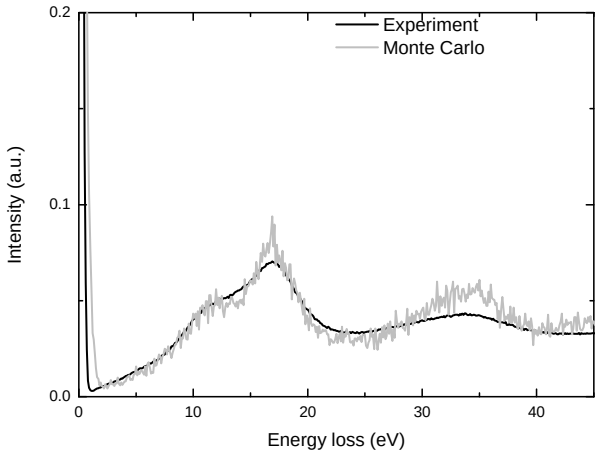

Figure 10.17: Comparison between the experimental (black line) and the present Monte Carlo (gray line) electron energy loss spectra for 500 eV electrons impinging on Si. The spectra are normalized to a common area of the zero loss peak.

with the suggestion given by Shimizu and Ding Ze Jun [13] to use spherical symmetry in Monte Carlo simulation of secondary electron generation.

Once solved this problem, we shall apply the Monte Carlo code based on the assumption of spherical symmetry to Monte Carlo modeling of the so-called energy selective scanning electron microscopy, an important application of which is related to the study of the dopant distributions with high spatial resolution in semiconductor materials and devices.

10.4.1 Initial polar and azimuth angle of the SEs

The initial polar angle θ_s and the initial azimuth angle ϕ_s of each secondary electron can be calculated in two different ways. In the first one, assuming that the secondary electrons emerge with spherical symmetry, their initial polar and azimuth angles are randomly determined as [13]

$$\theta_s \, = \, \pi \, \mu_1 \, , \tag{10.10}$$

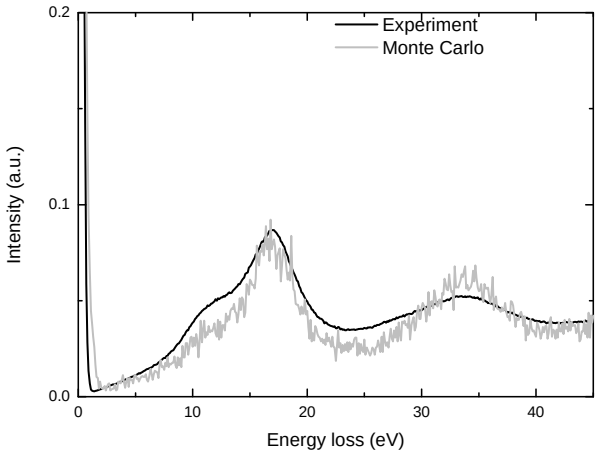

Figure 10.18: Comparison between the experimental (black line) and the present Monte Carlo (gray line) electron energy loss spectra for 1000 eV electrons impinging on Si. The spectra are normalized to a common area of the zero loss peak.

$$\phi_s \, = \, 2\,\pi\,\mu_2 \tag{10.11}$$

where μ_1 and μ_2 are random numbers uniformly distributed in the range $[0, 1]$. Even if such an approach violates momentum conservation and it is therefore questionable, Shimizu and Ding noticed that, as slow secondary electrons are actually generated with spherical symmetry [13], it should be used and preferred when Fermi sea excitations are involved in the process of generation of secondary electrons. Notice that we assumed spherical symmetry also in the previous Monte Carlo calculations devoted to the study of secondary electron yields.

MCSS is the name attributed, in the present context, to the Monte Carlo code based on this method.

Since a comparison with calculations where momentum conservation is taken into account was missing, a second code was proposed in which momentum conservation was taken into account by using the classical binary-collision model so that, if θ and ϕ are, respectively, the polar and azimuth

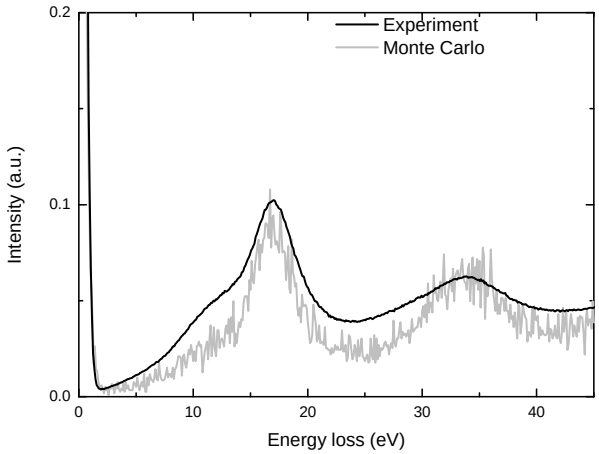

Figure 10.19: Comparison between the experimental (black line) and the present Monte Carlo (gray line) electron energy loss spectra for 2000 eV electrons impinging on Si. The spectra are normalized to a common area of the zero loss peak.

angle of the incident electron, then [13]

$$\sin\theta_s \;=\; \cos\theta\,, \tag{10.12}$$

$$\phi_s \;=\; \pi \,+\, \phi\,. \tag{10.13}$$

We shall indicate, in the present context, with MCMC the Monte Carlo code corresponding to this second approach. The results of the MCSS and MCMC codes will be compared to theoretical and experimental data [67].

10.4.2 Comparison to theoretical and experimental data

In Fig. 10.21 and in Fig. 10.22 the energy distributions of the secondary electrons emitted by silicon and copper targets, respectively, have been presented. The energy of the primary electron beam is E_0=1000 eV for the case of silicon, while it is E_0=300 eV for copper. The Monte Carlo calcula-

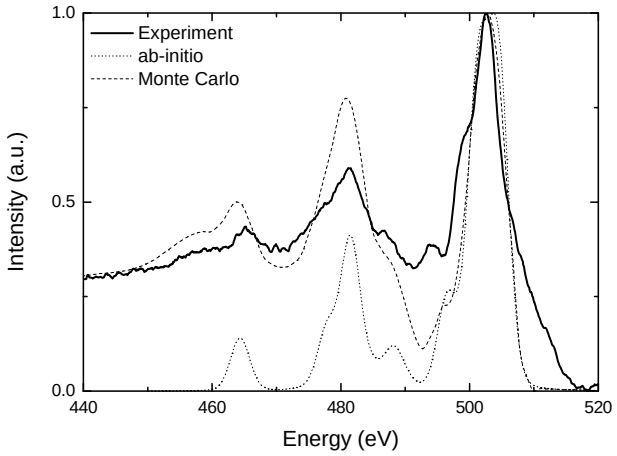

Figure 10.20: O K-LL Auger spectrum in SiO_2. Comparison between the quantum mechanical theoretical data (dotted line), the present Monte Carlo results (dashed line), and the original experimental data (continuous line) [36].

tions obtained with the two different methods described above (MCSS and MCMC) are compared to the Amelio theoretical results [120].

Using the theory of Amelio for the comparison, the MCSS scheme gives results that show a much better agreement than the MCMC code. Indeed, in the range of primary energies examined and for both the materials considered, it is clear that, using the MCSS code, the position of the maxima and the general trend of the energy distributions are in excellent agreement with the Amelio data. On the other hand, the use of the MCMC code generates electron energy distributions which are not in so good agreement with the Amelio data: the position of the maxima are shifted to higher energies and the shapes of the distributions are quite different from the Amelio energy distributions. Notice that experimental data concerning secondary electron energy distributions were reported by Amelio as well. In Tab. 10.2 and in Tab. 10.3 the main features regarding the energy distributions [i.e., the Most Probable Energy (MPE) and the Half Width at Half Maximum (FWHM)] obtained with MCSS and MCMC are compared to the experimental data reported by Amelio.

Concerning the secondary electron yields, namely the measures of the

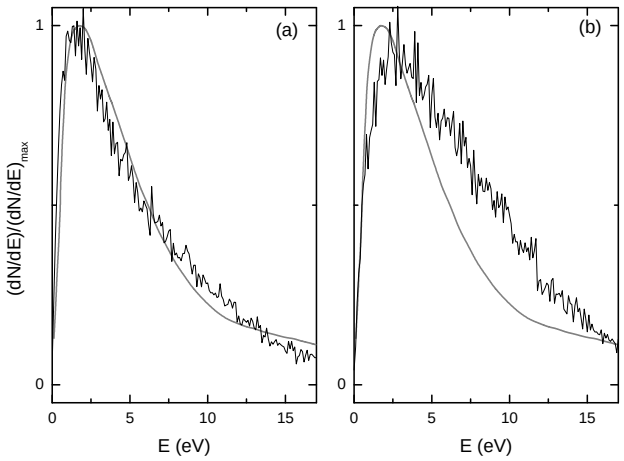

Figure 10.21: Energy distribution of the secondary electrons emitted by a silicon target. E_0=1000 eV. The present Monte Carlo calculations (black lines) [67] are compared to the Amelio theoretical results (gray lines) [120]. Panel (a): MCSS code. Panel (b): MCMC code (see details in the text).

areas under the energy distributions before performing normalization, they are summarized in Tab. 10.4 and in Tab. 10.5. The secondary electron yields both experimentally determined by Dionne [97] and by Shimizu [121] and calculated with the MCSS code are considerably higher than the same quantities computed with the MCMC code. The comparison demonstrates as well that the MCSS code should be preferred to the MCMC code, in the primary energy range examined (300-1000 eV), because MCSS gives results in better agreement with the experimental ones than MCMC.

The agreement of the MCSS results with the Amelio [120], Dionne [97], and Shimizu [121] theoretical and experimental data (and the disagreement between the MCMC and experimental results) can be attributed to the isotropy of the low-energy secondary electron emission due to:

(i) post-collisional effects and consequent random energy and momentum transfer among secondary electrons;

(ii) interactions with the conduction electrons, just after secondary electrons are emitted.

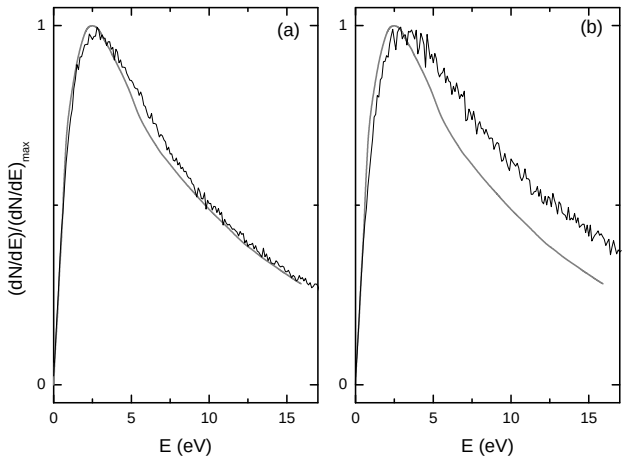

Figure 10.22: Energy distribution of the secondary electrons emitted by a copper target. E_0=300 eV. The present Monte Carlo calculations (black lines) [67] are compared to the Amelio theoretical results (gray lines) [120]. Panel (a): MCSS code. Panel (b): MCMC code (see details in the text).

In conclusion, the results of the present investigation suggest that slow secondary electrons should be generated with spherical symmetry in order to get agreement with experimental and theoretical data.

10.4.3 Application to energy selective scanning electron microscopy

Monte Carlo simulations of secondary electron energy distribution and yield have important applications in the design and characterization of semiconductor devices: in the field, in particular, of investigation of the distribution of dopant atom concentrations at the nanometer scale. This application is known as *two-dimensional dopant mapping*. Two-dimensional dopant mapping based on the secondary electron emission is a technique which allows a fast investigation of dopant distributions in semiconductors. By taking into account the electron affinity in Monte Carlo simulations to calculate the secondary electron emission from doped silicon, the dopant contrast can be

Si (1000eV)	MCSS	MCMC	Experiment
MPE (eV)	1.8	2.8	1.7
FWHM (eV)	5.3	8.5	5.0

Table 10.2: Monte Carlo Most Probable Energy (MPE) and Half Width at Half Maximum (FWHM) of secondary electron energy distributions obtained with two different schemes (MCSS and MCMC: see details in the text). The experimental data were reported by Amelio [120]. Material on which the calculations and the measurements were carried out was bulks of Si irradiated by streams of electrons in the $+z$ direction. The primary energy of the incident electron beam was 1000 eV.

Cu (300eV)	MCSS	MCMC	Experiment
MPE (eV)	2.8	3.5	2.8
FWHM (eV)	9.2	12	10

Table 10.3: Monte Carlo Most Probable Energy (MPE) and Half Width at Half Maximum (FWHM) of secondary electron energy distributions obtained with two different schemes (MCSS and MCMC: see details in the text). The experimental data were reported by Amelio [120]. Material on which the calculations and the measurements were carried out was bulks of Cu irradiated by streams of electrons in the $+z$ direction. The primary energy of the incident electron beam was 300 eV.

E_0 (eV)	MCSS	MCMC	Dionne [97]
300	1.26	0.58	1.17
500	1.15	0.54	1.12
1000	0.91	0.46	0.94

Table 10.4: Monte Carlo secondary electron yield calculations performed with two different schemes (MCSS and MCMC: see details in the text). Material on which the calculations and the measurements were carried out was bulks of Si irradiated by streams of electrons in the $+z$ direction. E_0 represents the primary energy of the incident electron beam.

E_0 (eV)	MCSS	MCMC	Shimizu [121]
300	1.09	0.71	–
500	1.02	0.65	1.01
1000	0.81	0.53	0.89

Table 10.5: Monte Carlo secondary electron yield calculations performed with two different schemes (MCSS and MCMC: see details in the text). Material on which the calculations and the measurements were carried out was bulks of Cu irradiated by streams of electrons in the $+z$ direction. E_0 represents the primary energy of the incident electron beam.

explained [71].

Doping contrast

A reliable method to map quantitatively the distribution of dopant atom concentrations at the nanometre scale is the use of secondary-electron contrast in the SEM [122, 123, 124, 125, 126, 127, 128]. Secondary-electron yield changes across a p-n junction [129]. The p-type region emits more secondary electrons than n-type region. As a consequence, the p-type is brighter in the SEM image.

The contrast C_{pn} can be calculated by

$$C_{\mathrm{pn}} \;=\; 200\frac{I_{\mathrm{p}} - I_{\mathrm{n}}}{I_{\mathrm{p}} + I_{\mathrm{n}}}\;, \tag{10.14}$$

where I_{p} and I_{n} represent the secondary electron emission yields of the p-type and n-type regions, respectively.

Increasing the affinity has the effect to truncate the lower end of the secondary electron emission spectrum. Indeed, electrons approaching the surface from the bulk meet an increased potential barrier, so that the conditions to emerge become more difficult to be satisfied. Since the integral of secondary electron emission spectrum provides the secondary-electron emission yield, we expect it decreases as the electron affinity increases. As the Fermi levels equilibrate at the p-n junction, the p-type region has lower electron affinity than the n-type region. Thus the p-type region emits more sec-

ondary electrons than the n-type region, as confirmed by our Monte Carlo simulation.

Actually, in a p-n junction, it is the difference in the electron affinities, or the so-called *built-in* potential $eV_{\rm bi}$, rather than the absolute values of the electron affinities, which matters in the determination of the contrast. The bulk built-in potential can be easily calculated for a simple p-n junction. Assuming full ionisation, it is given by [130]:

$$eV_{\rm bi} \;=\; k_{\rm B}\,T\;\ln\frac{N_{\rm a}N_{\rm d}}{N_{\rm i}^2}\;, \tag{10.15}$$

where $k_{\rm B}$ is the Boltzmann constant, T is the absolute temperature, and $N_{\rm a}$, $N_{\rm d}$, and $N_{\rm i}$ are, respectively, the acceptor dopant carrier concentration, the donor dopant carrier concentration, and the intrinsic carrier concentration. Notice that Eq. (10.15) allows one to calculate the built-in potential if the doping levels of n- and p- regions in contact are known.

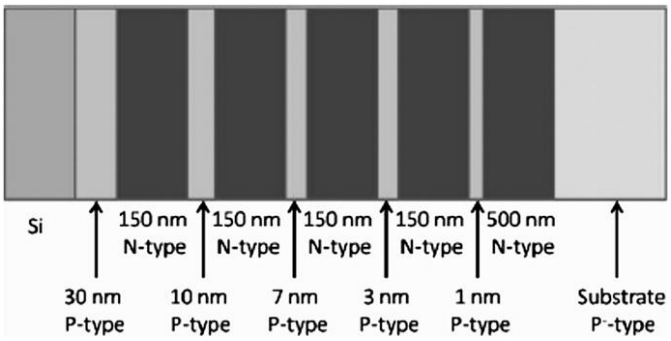

Figure 10.23: Schematic drawing of resolution test structure. Courtesy of Cornelia Rodenburg, University of Sheffield.

The value of the electron affinity of pure (un-doped) Si was reported to be 4.05 eV [68]. The Monte Carlo calculations (ES strategy, MCSS) were performed with χ=3.75 eV for the p-type sample and χ=4.35 eV for the n-type sample, and for an electron energy E_0 =1000 eV. Using a specimen with

doping levels of p and n consistent with these values of the electron affinities, and the same electron energy, a contrast of $C_{\rm pn}$=(16±3)% was reported by Elliott *et al.* [128]. The Monte Carlo simulated contrast is $C_{\rm pn}$ =(17±3)% [71], in reasonable agreement with the Elliott *et al.* experimental observation.

Energy selective scanning electron microscopy

Rodenburg *et al.* [44] experimentally demonstrated that the image contrast in p-n junctions, obtained considering only the low energy electrons, is significantly higher than that obtained under standard conditions (where secondary electrons of all energies contribute to the formation of the image). As a consequence, selecting secondary electrons in a given (low) energy window, instead of permitting to all the secondary electrons to form the image, improves the potentiality of electron microscopy. This technique of selecting the energy of the emitted secondary electrons is known as energy selective SEM (ESSEM). ESSEM improves the quality of the measurement of two dimensional dopant atom distributions in the SEM, allowing more accurate quantification of the contrast. Due the presence of surface states and the corresponding *surface band bending*, the built-in potential is reduced close to the surface with respect to the value that one can calculate using Eq. 10.15 [131]. Thus secondary electrons emitted from the surface region, where surface band bending reduces the built-in potential, will not see the full built-in voltage of the bulk. For a pure silicon specimen, our Monte Carlo simulated spectra are presented in Fig. 10.24. The maximum of the distribution of the secondary electrons that are generated at a depth of 1 Å is located at ≈10 eV. On the other hand, we can observe that the distribution of the secondary electrons generated within a depth of up to 20 Å presents a maximum located at an energy ≈2 eV. Thus, secondary electrons leaving the material with lower kinetic energy have been generated deeper in the specimen than those with higher energy. Our Monte Carlo results, relative to Si, are similar to those published by other authors relative to Cu [132] and to SiO_2 [133]. According to the experimental observations, the larger the V_{bi}, the higher the contrast. Since the high energy electrons are generated close to the surface, where the built-in potential is lower, selecting secondary electrons of low energy should enhance the dopant contrast: this is in perfect agreement with the experimental observations provided by Rodenburg *et al.* [44]. This enhanced contrast can be understood through the knowledge of the Monte Carlo simulated secondary electron spectrum, which helps to adjust the ex-

perimental energy cut-off needed for getting best dopant contrast.

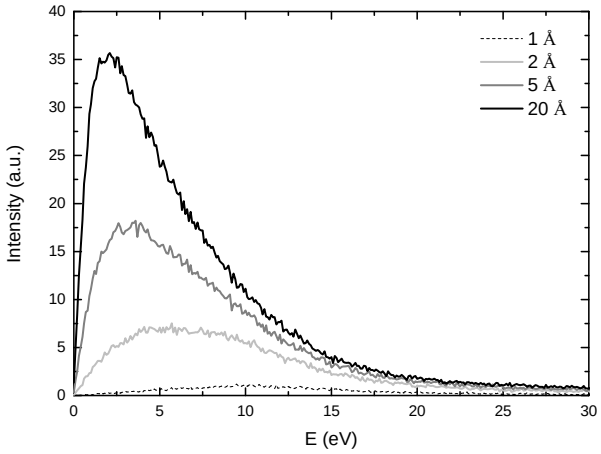

Figure 10.24: Present Monte Carlo calculated contributions of secondary electron originating from different depths to secondary electron spectrum in Si [44].

10.5 Concluding remarks about energy distributions

Experimental reflection electron energy loss spectra, acquired at variable electron energy were simulated by the Monte Carlo method. Different electron energies were considered to obtain different relative intensities of surface and bulk features in the spectra. Reasonable agreement was found between simulated and experimental spectra, both in the intensity of loss features compared with the zero loss peak and in the relative intensity of surface and bulk features.

Secondary electron emission spectra were simulated as well. Our Monte Carlo simulations demonstrate, in particular, that secondary electrons leaving the material with lower kinetic energy are generated deeper in the specimen than those with higher energy. As a consequence, as the built-in potential is reduced close to the surface, selecting low energy secondary electrons,

instead of permitting to all the secondary electrons to form the image, enhance the contrast, improving the quality of the measurement of two dimensional dopant atom distributions. Dopant mapping using secondary electrons of low energy presents then significant advantages over standard secondary electron imaging and Monte Carlo simulated secondary electron spectra are paramount to adjust the experimental energy cut-off needed for getting best dopant contrast.

Chapter 11

Conclusions

The Monte Carlo method has been demonstrated to be a powerful tool for an accurate description of many physical phenomena occurring when electron beams interact with solid targets. It permits to predict the behavior of both the backscattered and the secondary electrons. The backscattering coefficient and the secondary electron yield were calculated for various materials and in a wide electron energy range. Furthermore, energy distributions (of both backscattered and secondary electrons) were simulated and compared to experimental data, showing a satisfactory agreement in all the examined cases.

Concerning the methods, CSDA and ES strategies were compared in several conditions. The physically more correct and realistic ES strategy has been demonstrated to provide results more accurate than the CSDA strategy. On the other hand, the CSDA strategy is faster than the ES strategy, so that in the conditions in which both provide similar results (e.g., backscattering coefficient and secondary electron emission yield) it can be safely utilized. Of course, the study of the energy distributions, for which the accurate description of energy loss statistical fluctuations are needed, requires the use of the ES strategy.

Thickness of surface films was demonstrated, both numerically and experimentally, to be related to the backscattering coefficient. Electron backscattering coefficient of Pd and Au thin films deposited on Si was simulated for various primary electron energies and over-layer thicknesses. Monte Carlo results were compared to experimental data. Monte Carlo electron backscattering coefficient of two-layer systems deposited on Si was presented as well. Monte Carlo simulations allowed to quantitatively establish a relationship be-

tween backscattering and thickness (we have investigated the particular case of gold thin films), so that a measurement of the backscattering coefficient allows to get the over-layer thickness.

The simulation of secondary electron yield allowed us to investigate the line-scan of resist materials (e.g. PMMA) with given geometrical cross-sections deposited on Si substrates. The chemical analysis of the surfaces and the interfaces of materials (SEM, TEM, REELS) and the energy selective SEM for image contrast in Si p-n junctions, represent other examples of the present applications of the Monte Carlo method.

Concerning electron spectra, we have demonstrated that Monte Carlo simulation well describes both the plasmon losses and the secondary electron energy distributions. We have demonstrated, in particular, that the Chen and Kwei theory very well describes, in the electron energy range from 500 to 2000 eV, the energy dependence of the surface to bulk intensity ratio of the plasmon peaks. On the other hand, since this theory does not take properly into account dispersion, for it neglects the dependence of the dielectric function on the momentum transfer, the experimentally observed asymmetries of the plasmon peaks is not well reproduced. This open problem has been recently approached by Kyriakou *et al.* [114]. Further investigations are required in this field.

Part V

Appendices

Appendix A

Mott theory

Relativistic partial wave expansion method

The original version of the Mott theory (also known as the relativistic partial wave expansion method, RPWEM) can be found in Ref. [16]. Also see Refs. [48, 34, 35, 36] for further details and applications.

According to Mott, the elastic scattering process can be treated by calculating the so-called phase shifts. If we indicate with r the radial coordinate, since the large-r asymptotic behavior of the radial wave function is known, the phase shifts can be computed by solving the Dirac equation for a central electrostatic field up to a large radius where the atomic potential can be neglected.

The Mott theory is thus based on the solution of the Dirac equation in a central filed. Lin, Sherman, and Percus [134] and Bunyan and Schönfelder [135] demonstrated that the Dirac equation in a central field can be transformed in the following first-order differential equation:

$$\frac{d\phi_{\mathrm{l}}^{\pm}(r)}{dr} = \frac{k^{\pm}}{r}\sin[2\phi_{\mathrm{l}}^{\pm}(r)] - \frac{mc^2}{\hbar c}\cos[2\phi_{\mathrm{l}}^{\pm}(r)] + \frac{E - V(r)}{\hbar c}\ , \tag{A.1}$$

where $V(r)$ is the atomic potential (see below), c the speed of light, $k^{+} = -l-1$, $k^{-} = l$, and $l = 0, 1, \cdots, \infty$. The numerical solution of this equation allows to calculate $\phi_{\mathrm{l}}^{\pm}$, defined as the limit of $\phi_{\mathrm{l}}^{\pm}(r)$ as r goes to ∞:

$$\phi_{\mathrm{l}}^{\pm} = \lim_{r\to\infty} \phi_{\mathrm{l}}^{\pm}(r)\ . \tag{A.2}$$

The Mott theory predicts that the differential elastic scattering cross-section is given by

$$\frac{d\sigma_{\rm el}}{d\Omega} = \mid f(\vartheta) \mid^2 + \mid g(\vartheta) \mid^2 \ . \tag{A.3}$$

The functions $f(\vartheta)$ and $g(\vartheta)$ are the so-called scattering amplitudes. According to Mott [16], the scattering amplitudes can be calculated by

$$f(\vartheta) = \frac{1}{2iK} \sum_{l=0}^{\infty} \{(l+1)[\exp(2i\eta_{\rm l}^-) - 1] + l[\exp(2i\eta_{\rm l}^+) - 1]\} P_{\rm l}(\cos\vartheta) \ , \tag{A.4}$$

$$g(\vartheta) = \frac{1}{2iK} \sum_{l=1}^{\infty} [-\exp(2i\eta_{\rm l}^-) + \exp(2i\eta_{\rm l}^+)] \ P_{\rm l}^1(\cos\vartheta) \ , \tag{A.5}$$

where, indicated with E the electron kinetic energy and with m the electron mass, K is calculated by

$$K^2 = \frac{E^2 - m^2c^4}{\hbar^2 c^2} \ . \tag{A.6}$$

The quantities $\eta_{\rm l}^-$ and $\eta_{\rm l}^+$ are the phase shifts, the functions $P_{\rm l}$ are the Legendre's polynomials, and

$$P_{\rm l}^1(x) = (1-x^2)^{1/2} \frac{dP_{\rm l}(x)}{dx} \ . \tag{A.7}$$

The phase shifts can be obtained by the solution of the equation

$$\tan\eta_{\rm l}^{\pm} = \frac{Kj_{l+1}(Kr) - j_{\rm l}(Kr)[\xi \tan\phi_{\rm l}^{\pm} + (1+l+k^{\pm})/r]}{Kn_{l+1}(Kr) - n_{\rm l}(Kr)[\xi \tan\phi_{\rm l}^{\pm} + (1+l+k^{\pm})/r]} \ , \tag{A.8}$$

where

$$\xi = \frac{E + mc^2}{\hbar c} \ . \tag{A.9}$$

In Eq. (A.8), j_l and n_l are the regular- and the irregular-spherical Bessel functions, respectively.

If, in the previous equations, we impose that

$$\eta_l^- = \eta_l^+ \; = \; \eta_l \tag{A.10}$$

we obtain the non-relativistic equation. Indeed, in such a case,

$$\begin{aligned} f(\theta) \quad &= \frac{1}{2iK}\sum_{l=0}^{\infty}(2l+1)[\exp(2i\eta_l)-1]P_l(\cos\theta) \\ &= \frac{1}{K}\sum_{l=0}^{\infty}(2l+1)\exp(i\eta_l)\sin\eta_l P_l(\cos\theta)\;, \end{aligned} \tag{A.11}$$

while the function $g(\theta)$ is identically null:

$$g(\theta) = 0\;. \tag{A.12}$$

Thus the elastic scattering cross-section is given by the simple equation

$$\frac{d\sigma_{\rm el}}{d\Omega} \; = \; |f|^2 \; = \; \left|\frac{1}{K}\sum_{l=0}^{\infty}(2l+1)\exp(i\eta_l)\sin\eta_l P_l(\cos\theta)\right|^2 \;. \tag{A.13}$$

This result, of course, can also be directly obtained by solving the Schrödinger equation in a central field. This is done by following a procedure known as partial wave expansion method. Notice that both the partial wave expansion method and the relativistic partial wave expansion method require numerical approaches, as they do not provide any analytic formula for calculating the differential elastic scattering cross-section. Furthermore, in both cases, Dirac-Hartree-Fock-Slater numerical methods are typically utilized for the calculation of the screened nuclear potential. As a very useful alternative, Salvat *et al.* [136] proposed an simple formula for the screened nuclear potential – valid for all the elements of the periodic table – which represents the best fit of the numerically calculated Dirac-Hartree-Fock-Slater potential (see below).

Notice that, in molecular solids, the differential elastic scattering cross-section can be approximated as the sum of the atomic differential elastic scattering cross-sections of the atoms in the molecule.

Analytic approximation of the Mott cross-section

Taking advantage of the simple closed form of the equations deduced starting by the Rutherford cross-section, it is sometimes possible to look for an approximation where similar equations are used for the Mott cross-section [103, 137]. For low atomic number elements and for some oxides, the Mott differential elastic scattering cross-section can be roughly approximated by the following equation:

$$\frac{d\sigma_{\mathrm{el}}}{d\Omega} \;=\; \frac{\Phi}{(1-\cos\theta+\Psi)^2}\;, \tag{A.14}$$

where the unknown parameters Φ and Ψ are calculated with the aim to get the best fit of the total and the first transport elastic scattering cross-section previously calculated using the RPWEM. With

$$\Phi \;=\; \frac{Z^2e^2}{4E^2} \tag{A.15}$$

and

$$\Psi \;=\; \frac{me^4\pi^2Z^{2/3}}{h^2E} \tag{A.16}$$

Eq. (A.14) become the screened Rutherford formula.

The knowledge of the total elastic scattering cross-section and of the transport elastic scattering cross-section previously calculated using the Mott theory allow us, on the other hand, to calculate Φ and Ψ in order to approximate the the Mott theory [103]. From Eq. (4.2) it follows that:

$$\sigma_{\mathrm{el}} \;=\; \frac{4\pi\Phi}{\Psi(\Psi+2)}\,. \tag{A.17}$$

As a consequence the differential elastic scattering cross-section can be rewritten as:

$$\frac{d\sigma_{\rm el}}{d\Omega} \;=\; \frac{\sigma_{\rm el}}{4\,\pi}\frac{\Psi(\Psi+2)}{(1-\cos\theta+\Psi)^2} \tag{A.18}$$

Using Eqs. (4.3) and (A.18) it is possible to obtain the ratio Ξ between the transport and the total elastic scattering cross-sections:

$$\Xi \;\equiv\; \frac{\sigma_{\rm tr}}{\sigma_{\rm el}} \;=\; \Psi\,\left[\frac{\Psi+2}{2}\,\ln\left(\frac{\Psi+2}{\Psi}\right)-1\right]\,. \tag{A.19}$$

Once the values of the total and transport elastic scattering cross-sections have been numerically calculated using the RPWEM, the ratio Ξ is determined as a function of the electron kinetic energy E. In such a way it is possible to get the screening parameter Ψ as a function of E (using a bisection algorithm).

The atomic potential

To calculate the atomic potential, the self-consistent Dirac-Hartree-Fock-Slater field should be used. In order to reduce the computer calculation time, the analytic approximation proposed by Salvat *et al.* [136] for the Dirac-Hartre-Fock-Slater field can be utilized instead. The Salvat *et al.* atomic potential is a superposition of Yukawa's potentials depending on a number of parameters which have been determined by looking for the best fit of the numerical calculated self-consistent Dirac-Hartree-Fock-Slater fields. The atomic potential is expressed by a pure Coulomb potential multiplied by a function $\psi(r)$ approximating the screening of the nucleus by the orbital electrons. The Salvat *et al.* screening function is given by:

$$\psi(r) = \sum_{i=1}^{3} A_i \exp(-\alpha_i r)\;, \tag{A.20}$$

where A_i and α_i are parameters whose values can be found in Ref. [136] for all the elements of the periodic table.

Electron exchange

As electrons are identical particles, exchange effect have to be taken into account, since it can occur that the incident electron is captured by an atom

and a new electron is emitted. Exchange effects are well described by adding, to the atomic potential described above, the Furness and McCarthy exchange potential [138]:

$$V_{ex} = \frac{1}{2}(E - V) - \frac{1}{2}[(E - V)^2 + 4\pi\rho e^2\hbar^2/m]^{1/2} \; . \tag{A.21}$$

In this equation, E is the electron energy, V the electrostatic potential, ρ the atomic electron density (obtained by Poisson's equation), and e the electron charge.

Solid-state effects

For atoms bound in solids, the outer orbitals are modified, so that solid-state effects should be introduced. In the so-called *muffin-tin* model, the potential of every atom in the solid is changed by the nearest-neighbor atoms. If we assume that the nearest-neighbor atoms are located at distances equal to $2r_{ws}$, where r_{ws} is the radius of the Wigner-Seitz sphere [130], then the potential can be calculated as follows, for $r \leq r_{ws}$,

$$V_{solid}(r \leq r_{ws}) = V(r) + V(2r_{ws} - r) - 2V(r_{ws}) \; . \tag{A.22}$$

It is on the other hand equal to zero outside the Wigner-Seitz sphere, i.e.,

$$V_{solid}(r \geq r_{ws}) = 0 \; . \tag{A.23}$$

The term $2V(r_{ws})$ was introduced in Eq. (A.22) to shift the energy scale so that $V_{solid}(r = r_{ws}) = 0$. According to Salvat and Mayol, it has also to be subtracted from the kinetic energy of the incident electrons [139].

Appendix B

Fröhlich theory

The original version of the Fröhlich theory can be found in Ref. [18]. Also see Ref. [51] for further details.

In his theory of the electron-phonon interaction, Fröhlich [18] considered, in particular, the interaction of free conduction electrons with the longitudinal optical mode lattice vibrations. The interaction was treated considering both phonon creation and phonon annihilation, corresponding to electron energy loss and to electrons energy gain, respectively. As the phonon generation probability is much higher than the phonon absorption probability, the last is often neglected in Monte Carlo simulations. Furthermore, since, according to Ganachaud and Mokrani [19], the dispersion relation of the longitudinal phonons can be neglected in the optical branch, one can use a single phonon frequency.
If we indicate with ω the angular frequency of the longitudinal optical vibrations of the lattice, then the average number of phonons at temperature T is given by the occupation function

$$n(T) \;=\; \frac{1}{\exp\left(\hbar\,\omega/k_{\mathrm{B}}T\right) \;-\; 1}\;, \tag{B.1}$$

where k_{B} is the Boltzmann constant. Fröhlich theory [18] uses the perturbation approach, assuming that the electron-lattice coupling is weak. If the electron energy, measured with respect to the bottom of the conduction band, is given by

$$E_k \;=\; \frac{\hbar^2\,k^2}{2\,m^*}\;, \tag{B.2}$$

where m^* is the electron effective mass and $\mathbf{k}$ the electron wavenumber, then the unperturbed electron wavefunction can be written as

$$| \mathbf{k}\rangle \;=\; \frac{\exp\left(i\,\mathbf{k}\cdot\,\mathbf{r}\right)}{V^{1/2}}\;, \tag{B.3}$$

where we have indicated with V a cubic volume containing the electron. According to Fröhlich [18] and to Llacer and Garwin [51], the interaction Hamiltonian is given by

$$\mathcal{H} \;=\; 4\,\pi\,i\,\sqrt{\frac{e^2\,\hbar}{2\,\gamma\,\omega\,V}}\sum_{\mathbf{q}}\frac{1}{q}[a_{\mathrm{q}}^*\,\exp\left(-i\,\mathbf{q}\cdot\mathbf{r}\right)\;-\;a_{\mathrm{q}}\,\exp\left(i\,\mathbf{q}\cdot\mathbf{r}\right)]\;, \tag{B.4}$$

where $\mathbf{q}$ is the phonon wavenumber, a_{q}^* and a_{q} are, respectively, the operators of creation and annihilation of phonons, and γ is related to the static dielectric constant ε_0 and to the high frequency dielectric constant ε_∞ by the following expression:

$$\frac{1}{\gamma} \;=\; \frac{\omega^2}{4\,\pi}\left(\frac{1}{\varepsilon_\infty}\;-\;\frac{1}{\varepsilon_0}\right)\;. \tag{B.5}$$

In order to calculate the transition rate $W_{kk'}$ from the state $| \mathbf{k}\rangle$ to the state $| \mathbf{k}'\rangle$, Llacer and Garwin [51] used the standard result of the perturbation theory. In the case of phonon annihilation, corresponding to an electron energy gain, once should consider the frequency

$$\beta \;=\; \frac{E_{\mathrm{k}'}\;-\;E_{\mathrm{k}}\;-\;\hbar\,\omega}{2\,\hbar}\;, \tag{B.6}$$

while, for phonon creation (electron energy loss), the frequency to be considered is the following

$$\beta \;=\; \frac{E_{\mathrm{k}'}\;-\;E_{\mathrm{k}}\;+\;\hbar\,\omega}{2\,\hbar}\;. \tag{B.7}$$

The rate is given by

$$W_{\mathrm{kk'}} \;=\; \frac{|M_{\mathrm{kk'}}|^2}{\hbar^2}\frac{\partial}{\partial t}\left(\frac{\sin^2\beta t}{\beta^2}\right) \tag{B.8}$$

where M'_{kk} is the matrix element for the transition from the state $\mathbf{k}$ to the state $\mathbf{k'}$. Notice that, for the case of annihilation of a phonon of wavenumber $\mathbf{q}$, $\mathbf{k'} \;=\; \mathbf{k} \;+\; \mathbf{q}$ and

$$M_{\mathrm{kk'}} \;=\; 4\,\pi\,i\,\sqrt{\frac{e^2\,\hbar}{2\,\gamma\,\omega\,V}}\frac{\sqrt{n(T)}}{q}\;, \tag{B.9}$$

while, in the case of the creation of a phonon of wavenumber $\mathbf{q}$, $\mathbf{k'} \;=\; \mathbf{k} \;-\; \mathbf{q}$ and

$$M_{\mathrm{kk'}} \;=\; -\,4\,\pi\,i\,\sqrt{\frac{e^2\,\hbar}{2\,\gamma\,\omega\,V}}\frac{\sqrt{n(T)+1}}{q}\;. \tag{B.10}$$

The total scattering rate from a state $\mathbf{k}$ to all the available states $\mathbf{k'}$ can be obtained integrating over $\mathbf{q}$. Let us first perform the integration for the case of phonon annihilation:

$$W^{-}_{\mathrm{k}} \;=\; \int_{q_{\min}}^{q_{\max}} dq \int_0^{2\,\pi} d\phi \int_0^{\pi} \frac{16\,\pi^2\,e^2}{2\,\hbar\,\gamma\,\omega\,V}\,\frac{n(T)}{q^2}\frac{\partial}{\partial\,t}\,\frac{\sin^2\,\beta\,t}{\beta^2}\,\frac{V}{8\,\pi^3}\,q^2\,\sin\alpha\,d\alpha\;. \tag{B.11}$$

Notice that α represents in this context the angle between the direction of $\mathbf{k}$ and that of $\mathbf{q}$, while we shall use the symbol θ to indicate the angle between $\mathbf{k}$ and $\mathbf{k'}$. As

$$k'^2 \;=\; k^2 \;+\; q^2 \;-\; 2\,k\,q\,\cos\alpha\;, \tag{B.12}$$

some simple algebraic manipulations allow as to to see that

$$\beta \;=\; \frac{\hbar}{4\,m^*}\,q^2 \;-\; \frac{\hbar}{2\,m^*}\,k\,q\,\cos\alpha \;-\; \frac{\omega}{2}\;, \tag{B.13}$$

so that

$$\sin\alpha\,d\alpha \;=\; \frac{2\,m^*}{\hbar}\frac{1}{k\,q}\,d\beta\;. \tag{B.14}$$

As a consequence

$$W_{\rm k}^{-} \;=\; \int_{q_{\rm min}}^{q_{\rm max}} dq \int_{\beta_{\rm min}}^{\beta_{\rm max}} \frac{4\,m^*\,e^2\,n(T)}{\hbar^2\,\gamma\,\omega}\frac{1}{k\,q}\,\frac{\partial}{\partial\,t}\frac{\sin^2\beta\,t}{\beta^2}\,d\beta\;, \tag{B.15}$$

where

$$\beta_{\rm min} \;=\; \frac{\hbar}{4\,m^*}\,q^2 \;-\; \frac{\hbar}{2\,m^*}\,k\,q \;-\; \frac{\omega}{2}\;, \tag{B.16}$$

and

$$\beta_{\rm max} \;=\; \frac{\hbar}{4\,m^*}\,q^2 \;+\; \frac{\hbar}{2\,m^*}\,k\,q \;-\; \frac{\omega}{2}\;, \tag{B.17}$$

Now

$$\begin{aligned}
&\int_{\beta_{\rm min}}^{\beta_{\rm max}} \frac{\partial}{\partial\,t}\frac{\sin^2\beta\,t}{\beta^2}\,d\beta \;=\; \int_{\beta_{\rm min}}^{\beta_{\rm max}} \frac{\sin\,2\,\beta\,t}{\beta}\,d\beta \;=\\
&=\; \int_{\beta_{\rm min}}^{\beta_{\rm max}} \frac{\sin(\,2\,\beta\,t)}{(2\,\beta\,t)}\,2\,t\,d\beta \;=\int_{2\,\beta_{\rm min}\,t}^{2\,\beta_{\rm max}\,t} \frac{\sin x}{x}\,dx \;=\\
&=\; \int_0^{2\,\beta_{\rm max}\,t} \frac{\sin x}{x}\,dx \;-\; \int_0^{2\,\beta_{\rm min}\,t} \frac{\sin x}{x}\,dx\;.
\end{aligned}$$

In order to carry out the calculation, we need to know the limits of integration, $q_{\rm min}$ and $q_{\rm max}$. They can be obtained by using the law of conservation of energy, $E'_{\rm k} \;=\; E_{\rm k} \;+\; \hbar\,\omega$, which corresponds to $\beta \;=\; 0$.
As $\cos\alpha$ can assume all the values between -1 and $+1$, the limits of integration satisfy the following equations

$$q^2 \;+\; 2\,k\,q \;-\; \frac{k^2\,\hbar\,\omega}{E_{\rm k}} \;=\; 0\;, \tag{B.18}$$

$$q^2 \;-\; 2\,k\,q \;-\; \frac{k^2\,\hbar\,\omega}{E_{\rm k}} \;=\; 0\;, \tag{B.19}$$

so that, as q is positive,

$$q_{\min} \;=\; k\;\left(\sqrt{1+\frac{\hbar\,\omega}{E_{\rm k}}}\;-\;1\right)\;, \tag{B.20}$$

$$q_{\max} \;=\; k\;\left(\sqrt{1+\frac{\hbar\,\omega}{E_{\rm k}}}\;+\;1\right)\;. \tag{B.21}$$

Inserting these limits of integration in the definition of $\beta_{\min}$ and $\beta_{\max}$, we see that $\beta_{\min} \leq 0$ and $\beta_{\max} \geq 0$. Therefore,

$$\begin{aligned}
&\lim_{t\to\infty}\int_{\beta_{\min}}^{\beta_{\max}}\;\frac{\partial}{\partial\,t}\frac{\sin^2\beta\,t}{\beta^2}\;d\beta\;= \\
&=\;\lim_{t\to\infty}\left(\int_0^{2\,\beta_{\max}\,t}\frac{\sin x}{x}\;dx\;-\;\int_0^{2\,\beta_{\min}\,t}\frac{\sin x}{x}\;dx\right)\;= \\
&=\;\int_0^{+\infty}\frac{\sin x}{x}\;dx\;-\;\int_0^{-\infty}\frac{\sin x}{x}\;dx\;= \\
&=\;{\rm si}(+\infty)\;-\;{\rm si}(-\infty)\;=\;\frac{\pi}{2}\;-\;\left(-\,\frac{\pi}{2}\right)\;=\;\pi\;,
\end{aligned}$$

so that

$$W_{\rm k}^{-}\;=\;\int_{q_{\min}}^{q_{\max}}\;\frac{4\,\pi\,m^*\,e^2\,n(T)}{\hbar^2\,\gamma\,\omega}\frac{1}{k\,q}\;dq\;. \tag{B.22}$$

As a consequence, we conclude that the total scattering rate for the phonon annihilation (electron energy gain) is given by

$$W_{\rm k}^{-}\;=\;\frac{4\,\pi\,e^2\,m^*\,n(T)}{\hbar^2\,\gamma\,\omega\,k}\;\ln\left(\frac{\sqrt{1\;+\;\hbar\,\omega/E_{\rm k}}\;+\;1}{\sqrt{1\;+\;\hbar\,\omega/E_{\rm k}}\;-\;1}\right)\;. \tag{B.23}$$

The treatment of the case of phonon creation (electron energy loss) is similar. Remember that, in this case, we have to use $\sqrt{n(T)\;+\;1}$ instead of $\sqrt{n(T)}$ in the matrix element of the transition of electron in state $\mathbf{k}$ to $\mathbf{k}'$. Furthermore, in this case,

$$\beta \;=\; \frac{1}{2\,\hbar}\,[E_{\mathrm{k}'} \;-\; (E_{\mathrm{k}} \;+\; \hbar\,\omega)] \;=\; \frac{\hbar}{4\,m^*}\,q^2 \;-\; \frac{\hbar}{2\,m^*}\,k\,q\,\cos\alpha \;+\; \frac{\omega}{2}\,, \quad \text{(B.24)}$$

so that

$$q_{\mathrm{min}} \;=\; k\,\left(1 \;-\; \sqrt{1 \;-\; \frac{\hbar\,\omega}{E_{\mathrm{k}}}}\right)\,, \quad \text{(B.25)}$$

$$q_{\mathrm{max}} \;=\; k\,\left(1 \;+\; \sqrt{1 \;-\; \frac{\hbar\,\omega}{E_{\mathrm{k}}}}\right)\,. \quad \text{(B.26)}$$

Therefore,

$$W^{+}_{\mathrm{k}} \;=\; \frac{4\,\pi\,e^2\,m^*\,[n(T) \;+\; 1]}{\hbar^2\,\gamma\,\omega\,k}\,\ln\left(\frac{1 \;+\; \sqrt{1 \;-\; \hbar\,\omega/E_{\mathrm{k}}}}{1 \;-\; \sqrt{1 \;-\; \hbar\,\omega/E_{\mathrm{k}}}}\right)\,. \quad \text{(B.27)}$$

Concerning the angular distribution of the scattering, let us consider the angle θ between $\mathbf{k}$ and $\mathbf{k}'$, so that

$$q^2 \;=\; k^2 \;+\; k'^2 \;-\; 2\,k\,k'\,\cos\theta \quad \text{(B.28)}$$

and, hence,

$$q\,dq \;=\; k\,k'\,\sin\theta\,d\theta\,. \quad \text{(B.29)}$$

The probability of scattering between θ and $\theta \;+\; d\theta$ can be calculated by considering the integrand of Eq.(B.22):

$$A\,\frac{dq}{k\,q} \;=\; A\,\frac{q\,dq}{k\,q^2} \;=\; A\,\frac{k\,k'\,\sin\theta\,d\theta}{k\,(k^2 \;+\; k'^2 \;-\; 2\,k\,k'\,\cos\theta)} \;=$$
$$=\; A\,\frac{k'\,\sin\theta\,d\theta}{k^2 \;+\; k'^2 \;-\; 2\,k\,k'\,\cos\theta}\,,$$

where, for the case of phonon annihilation,

$$A \;=\; \frac{4\,\pi\,e^2\,m^*\,n(T)}{\hbar^2\,\gamma\,\omega}\;. \tag{B.30}$$

Similar considerations hold for the case of phonon creation, so that we conclude that the angular distribution is proportional, in both cases, to

$$d\eta \;=\; \frac{E_{\mathrm{k}'}^{1/2}\sin\theta\;d\theta}{E_{\mathrm{k}}\;+\;E_{\mathrm{k}'}\;-\;2\,(E_{\mathrm{k}}\,E'_{\mathrm{k}})^{1/2}\;\cos\theta} \tag{B.31}$$

After an electron-phonon collision, the new angle θ' is obtained inverting this distribution. Indicating with μ the cumulative probability, we have

$$\begin{aligned}\mu \;&=\; \frac{\int_0^{\theta'}\;d\eta}{\int_0^{\pi}\;d\eta} \;= \\ &= \int_0^{\theta'}\;\frac{E_{\mathrm{k}'}^{1/2}\sin\theta\;d\theta}{E_{\mathrm{k}}\;+\;E_{\mathrm{k}'}\;-\;2\,(E_{\mathrm{k}}\,E'_{\mathrm{k}})^{1/2}\;\cos\theta}\Bigg/\int_0^{\pi}\;\frac{E_{\mathrm{k}'}^{1/2}\sin\theta\;d\theta}{E_{\mathrm{k}}\;+\;E_{\mathrm{k}'}\;-\;2\,(E_{\mathrm{k}}\,E'_{\mathrm{k}})^{1/2}\;\cos\theta}\;,\end{aligned} \tag{B.32}$$

and, as a consequence,

$$\cos\;\theta' \;=\; \frac{E_{\mathrm{k}}\;+\;E_{\mathrm{k}'}}{2\,\sqrt{E_{\mathrm{k}}\;E_{\mathrm{k}'}}}\;(1\;-\;B^{\mu})\;+\;B^{\mu}\;, \tag{B.33}$$

$$B \;=\; \frac{E_{\mathrm{k}}\;+\;E_{\mathrm{k}'}\;+\;2\,\sqrt{E_{\mathrm{k}}\;E_{\mathrm{k}'}}}{E_{\mathrm{k}}\;+\;E_{\mathrm{k}'}\;-\;2\,\sqrt{E_{\mathrm{k}}\;E_{\mathrm{k}'}}}\;. \tag{B.34}$$

The relationship between the mean free path $\lambda_{\mathrm{phonon}}$ and the total scattering rate from a state $\mathbf{k}$ to all the other available states $\mathbf{k}'$ is

$$\lambda_{\mathrm{phonon}} \;=\; \left(\frac{1}{v}\;\frac{dP}{dt}\right)^{-1}\;, \tag{B.35}$$

where v is the electron velocity before the electron-phonon collision

$$v \;=\; \frac{\hbar\, k}{m^*} \tag{B.36}$$

and

$$\frac{dP}{dt} \;=\; W_{\rm k}^{-} \;+\; W_{\rm k}^{+}\;. \tag{B.37}$$

The electron-phonon mean free path can then be written as

$$\lambda_{\rm phonon} \;=\; \frac{\hbar\, k/m^*}{W_{\rm k}^{-} \;+\; W_{\rm k}^{+}} \;=\; \frac{\sqrt{2\; E_k/m^*}}{W_{\rm k}^{-} \;+\; W_{\rm k}^{+}}\;, \tag{B.38}$$

and, as a consequence,

$$\begin{aligned}\lambda_{\rm phonon}^{-1} \;=\; & \frac{1}{a_0}\;\left[\frac{\varepsilon_0 \;-\; \varepsilon_\infty}{\varepsilon_0\;\;\varepsilon_\infty}\right]\;\frac{\hbar\,\omega}{E_{\rm k}}\;\frac{1}{2}\;\times \\ \times\;\left\{[n(T)\;+1]\;\ln\left[\frac{1\;+\;\sqrt{1\;-\;\hbar\,\omega/E_{\rm k}}}{1\;-\;\sqrt{1\;-\;\hbar\,\omega/E_{\rm k}}}\right]\;+\;n(T)\;\ln\left[\frac{\sqrt{1\;+\;\;\hbar\,\omega/E_{\rm k}}\;+\;1}{\sqrt{1\;+\;\hbar\,\omega/E_{\rm k}}\;-\;1}\right]\right\}\;,\end{aligned} \tag{B.39}$$

where we have assumed that the electron effective mass m^* is equal to that of a free electron, $m^* = m$.

The probability of phonon creation is much higher than that of phonon annihilation [19, 51, 40], so that one can safely ignore the electron energy gain due to the phonon annihilation. As a consequence we can write

$$\lambda_{\rm phonon} \;=\; \frac{\hbar\, k/m^*}{W_{\rm k}^{+}}\;, \tag{B.40}$$

so that, indicating with $E \;= E_k$ the energy of the incident electron and with $W_{\rm ph} \;=\; \hbar\omega$ the energy of the created phonon (and assuming that $m^* = m$) we conclude that the inverse inelastic mean free path for electron energy loss due to phonon creation can be written as [51]

$$\lambda_{\text{phonon}}^{-1} = \frac{1}{a_0} \frac{\varepsilon_0 - \varepsilon_\infty}{\varepsilon_0 \ \varepsilon_\infty} \frac{W_{\text{ph}}}{E} \frac{n(T) + 1}{2} \ln \left[\frac{1 + \sqrt{1 - W_{\text{ph}}/E}}{1 - \sqrt{1 - W_{\text{ph}}/E}} \right] . \tag{B.41}$$

This equation was used in Monte Carlo simulation of secondary electron emission from insulating materials [19, 40, 73].

Appendix C

Ritchie theory

The original version of the Ritchie theory can be found in Ref. [17]. Also see Ref. [36] for further details.

The response of the ensemble of conduction electrons to the electromagnetic disturbance due to electrons passing through a solid and losing energy in it, is described by a complex dielectric function $\varepsilon(\vec{k},\omega)$, where $\vec{k}$ is the wave vector and ω is the frequency of the electromagnetic field. If, at the time t, the electron position is $\vec{r}$ and its speed is $\vec{v}$, then, once indicated with e the electron charge, it can be represented by a charge distribution given by

$$\rho(\vec{r},t) \;=\; -e\;\delta(\vec{r}-\vec{v}t)\;, \tag{C.1}$$

so that the electric potential φ generated in the medium can be calculated as

$$\varepsilon(\vec{k},\omega)\;\vec{\nabla}^2\varphi(\vec{r},t) \;=\; -4\pi\;\rho(\vec{r},t) \;=\; 4\pi\;e\;\delta(\vec{r}-\vec{v}t)\;. \tag{C.2}$$

In the Fourier space we have

$$k^2\;\varepsilon(\vec{k},\omega)\;\varphi(\vec{k},\omega) \;=\; 4\pi\rho(\vec{k},\omega)\;, \tag{C.3}$$

so that

$$\varphi(\vec{k},\omega) \;=\; -\frac{8\pi^2 e}{\varepsilon(\vec{k},\omega)}\frac{\delta(\vec{k}\cdot\vec{v}\;+\;\omega)}{k^2}\;. \tag{C.4}$$

We are interested in calculating the energy loss $-dE$ of an electron due to its interaction with the electric field $\vec{\mathcal{E}}$ generated by the electrons passing through the solid. Let us indicate with $\mathcal{F}_z$ the z component of the electric force, so that

$$-dE \;=\; \vec{\mathcal{F}} \;\cdot\; d\vec{r} \;=\; \mathcal{F}_z \; dz \; . \tag{C.5}$$

Notice that in the last equation and in the following, the electric force (and the electric field $\vec{\mathcal{E}} \;=\; \vec{\mathcal{F}}/e$) are considered at $\vec{r} \;=\; \vec{v}\, t$. Since

$$\mathcal{E}_z \; dz \;=\; \frac{dz}{dt} \; dt \; \mathcal{E}_z \;=\; \frac{d\vec{r}}{dt} \cdot \vec{\mathcal{E}} \; dt \;=\; \frac{\vec{v} \cdot \vec{\mathcal{E}}}{v} \; dz \tag{C.6}$$

the energy loss $-dE$ per unit path length dz, $-dE/dz$, is given by

$$-\frac{dE}{dz} \;=\; \frac{e}{v} \; \vec{v} \;\cdot\; \vec{\mathcal{E}} \; . \tag{C.7}$$

As, on the other hand,

$$\vec{\mathcal{E}} \;=\; -\vec{\nabla} \; \varphi(\vec{r}, t) \tag{C.8}$$

and $\varphi(\vec{k}, \omega)$ is the Fourier transform of $\varphi(\vec{r}, t)$, so that

$$\varphi(\vec{r}, t) \;=\; \frac{1}{(2\,\pi)^4} \int \; d^3 \; \vec{k} \; \int_{-\infty}^{+\infty} \; d\omega \; \exp[i(\vec{k} \;\cdot\; \vec{r} \;+\; \omega \; t)] \; \varphi(\vec{k}, \omega) \; , \tag{C.9}$$

then

$$\vec{\mathcal{E}} \;=\; -\vec{\nabla} \left\{ \; \frac{1}{(2\,\pi)^4} \int \; d^3 \; \vec{k} \; \int_{-\infty}^{+\infty} \; d\omega \; \exp[i(\vec{k} \;\cdot\; \vec{r} \;+\; \omega \; t)] \; \varphi(\vec{k}, \omega) \right\} \; . \tag{C.10}$$

As a consequence

$$
\begin{aligned}
-\frac{dE}{dz} &= \\
&= \mathrm{Re}\left\{ -\frac{8\pi^2 e^2}{(2\pi)^4 v} \int d^3k \int_{-\infty}^{+\infty} d\omega (-\vec{\nabla}) \exp[i(\vec{k}\cdot\vec{r} + \omega\, t)] \cdot\ \vec{v}\, \frac{\delta(\vec{k}\cdot\vec{v} + \omega)}{k^2\ \varepsilon(\vec{k},\omega)} \right|_{\vec{r}\,=\,\vec{v}\,t} \Bigg\} \ = \\
&= \mathrm{Re}\left\{ -\frac{8\pi^2 e^2}{(2\pi)^4 v} \int d^3k \int_{-\infty}^{+\infty} d\omega (-i\vec{k})\cdot\vec{v} \exp[i(\vec{k}\cdot\vec{r} + \omega\, t)]\ \ \frac{\delta(\vec{k}\cdot\vec{v} + \omega)}{k^2\ \varepsilon(\vec{k},\omega)} \right|_{\vec{r}\,=\,\vec{v}\,t} \Bigg\} \ = \\
&= \mathrm{Re}\left\{ \frac{i8\pi^2 e^2}{16\pi^4 v} \int d^3k \int_{-\infty}^{+\infty} d\omega (\vec{k}\cdot\vec{v}) \exp[i(\vec{k}\cdot\vec{r} + \omega\, t)]\ \frac{\delta(\vec{k}\cdot\vec{v} + \omega)}{k^2\ \varepsilon(\vec{k},\omega)} \right|_{\vec{r}\,=\,\vec{v}\,t} \Bigg\} \ . \quad \text{(C.11)}
\end{aligned}
$$

Taking into account (i) that the electric field has to be calculated at $\vec{r}\ =\ \vec{v}\,t$ and (ii) of the presence in the integrand of the $\delta(\vec{k}\ \cdot\ \vec{v}\ +\ \omega)$ distribution, we have

$$
\begin{aligned}
-\frac{dE}{dz} &= \\
&= \mathrm{Re}\left\{ \frac{i\ e^2}{2\ \pi^2\ v} \int\ d^3k\ \int_{-\infty}^{+\infty}\ d\omega\ \vec{k}\ \cdot\ \vec{v}\ \exp[i(\vec{k}\ \cdot\ \vec{v}\,t\ +\ \omega\, t)]\ \frac{\delta(\vec{k}\ \cdot\ \vec{v}\ +\ \omega)}{k^2\ \varepsilon(\vec{k},\omega)} \right\} \ = \\
&= \mathrm{Re}\left\{ \frac{i\ e^2}{2\ \pi^2\ v} \int\ d^3k\ \int_{-\infty}^{+\infty}\ d\omega\ \vec{k}\ \cdot\ \vec{v}\ \exp[i(-\omega\, t\ +\ \omega\, t)]\ \frac{\delta(\vec{k}\ \cdot\ \vec{v}\ +\ \omega)}{k^2\ \varepsilon(\vec{k},\omega)} \right\} \ = \\
&= \mathrm{Re}\left\{ \frac{i\ e^2}{2\ \pi^2\ v} \int\ d^3k\ \int_{-\infty}^{+\infty}\ d\omega\ (-\omega)\ \exp[i(-\omega\, t\ +\ \omega\, t)]\ \frac{\delta(\vec{k}\ \cdot\ \vec{v}\ +\ \omega)}{k^2\ \varepsilon(\vec{k},\omega)} \right\} \ = \\
&= \mathrm{Re}\left\{ \frac{-i\ e^2}{2\ \pi^2\ v} \int\ d^3k\ \int_{-\infty}^{+\infty}\ d\omega\ \omega\ \frac{\delta(\vec{k}\ \cdot\ \vec{v}\ +\ \omega)}{k^2\ \varepsilon(\vec{k},\omega)} \right\} \ . \quad \text{(C.12)}
\end{aligned}
$$

Since

$$
\mathrm{Re}\left\{ i\ \int_{-\infty}^{+\infty}\ d\omega\ \omega\ \frac{\delta(\vec{k}\ \cdot\ \vec{v}\ +\ \omega)}{\varepsilon(\vec{k},\omega)} \right\} \ = 2\ \mathrm{Re}\left\{ i\ \int_{0}^{+\infty}\ d\omega\ \omega\ \frac{\delta(\vec{k}\ \cdot\ \vec{v}\ +\ \omega)}{\varepsilon(\vec{k},\omega)} \right\} \ ,
$$

we conclude that [17]

$$-\frac{dE}{dz} \;=\; \frac{e^2}{\pi^2\; v}\int\; d^3k \int_0^\infty\; d\omega\; \omega\; \mathrm{Im}\left[\frac{1}{\varepsilon(\vec{k},\omega)}\right]\; \frac{\delta(\vec{k}\;\cdot\;\vec{v}\;+\omega)}{k^2}\;, \qquad \text{(C.13)}$$

or

$$-\frac{dE}{dz} \;=\; \int_0^\infty\; d\omega\; \omega\; \tau(\vec{v},\omega)\;, \qquad \text{(C.14)}$$

where

$$\tau(\vec{v},\omega) \;=\; \frac{e^2}{\pi^2\; v}\;\int\; d^3k\; \mathrm{Im}\left[\frac{1}{\varepsilon(\vec{k},\omega)}\right]\; \frac{\delta(\vec{k}\;\cdot\;\vec{v}\;+\;\omega)}{k^2} \qquad \text{(C.15)}$$

is the probability of an energy loss ω per unit distance traveled by a non-relativistic electron of velocity $\vec{v}$.

Let us assume now that the solid is homogeneous and isotropic, and ε is a scalar just depending on the magnitude of $\vec{k}$ and not on its direction

$$\varepsilon(\vec{k},\omega) \;=\; \varepsilon(k,\omega) \qquad \text{(C.16)}$$

so that

$$\begin{aligned}
&\tau(v,\omega) \;= \\
&=\; \frac{e^2}{\pi^2\; v}\;\int_0^{2\pi}\; d\phi\;\int_0^{\pi}\; d\theta\;\int_{k_-}^{k_+}\; dk\; k^2\;\sin\theta\;\;\mathrm{Im}\left[\frac{1}{\varepsilon(k,\omega)}\right]\;\frac{\delta(k\;v\;\cos\theta\;+\;\omega)}{k^2}\;= \\
&=\; \frac{2\;e^2}{\pi\;v}\int_0^{\pi}\; d\theta\;\int_{k_-}^{k_+}\; dk\;\sin\theta\;\;\mathrm{Im}\left[\frac{1}{\varepsilon(k,\omega)}\right]\;\delta(k\;v\;\cos\theta\;+\;\omega) \qquad \text{(C.17)}
\end{aligned}$$

where

$$\hbar\; k_\pm \;=\; \sqrt{2\;m\;E}\;\pm\;\sqrt{2\;m\;(E\;-\;\hbar\;\omega)}\;. \qquad \text{(C.18)}$$

and $E \;=\; m\;v^2\;/\;2$. These limits of integration comes from conservation of momentum. Let us introduce the new variable $\omega^{'}$ defined as

$$\omega^{'} \;=\; -k\;v\;\cos\theta\;, \tag{C.19}$$

so that

$$d\omega^{'} \;=\; k\;v\;\sin\theta\;d\theta \tag{C.20}$$

and, hence,

$$\begin{aligned}\tau(v,\omega) \;&=\; \frac{2\;e^2}{\pi\;v}\;\int_{-k\,v}^{k\,v}\;d\,\omega^{'}\;\int_{k_-}^{k_+}\;\frac{dk}{k\;v}\,\mathrm{Im}\left[\frac{1}{\varepsilon(k,\omega)}\right]\;\delta(-\omega^{'}\;+\;\omega) \\ &=\; \frac{2\;m\;e^2}{\pi\;m\;v^2}\;\int_{k_-}^{k_+}\;\frac{dk}{k}\,\mathrm{Im}\left[\frac{1}{\varepsilon(k,\omega)}\right]\;.\end{aligned} \tag{C.21}$$

In conclusion, we can write that

$$\tau(E,\omega) \;=\; \frac{m\;e^2}{\pi\;E}\int_{k_-}^{k_+}\;\frac{dk}{k}\,\mathrm{Im}\left[\frac{1}{\varepsilon(k,\omega)}\right]\;, \tag{C.22}$$

Indicating with W the energy loss and with $W_{\max}$ the maximum energy loss, the inverse electron inelastic mean free path, $\lambda_{\mathrm{inel}}^{-1}$, can be calculated as

$$\lambda_{\mathrm{inel}}^{-1} \;=\; \frac{m\;e^2}{\pi\;\hbar^2\;E}\;\int_0^{W_{\max}}\;dW\;\int_{k_-}^{k_+}\;\frac{dk}{k}\,\mathrm{Im}\left[\frac{1}{\varepsilon(k,\omega)}\right]\;. \tag{C.23}$$

Appendix D

Chen and Kwei theory

The original version of the Chen and Kwei theory can be found in Ref. [27] for outgoing projectiles. It was generalized by Li *et al.* [28] for incoming projectiles. According to Dapor *et al.* [72], in the following the Chen and Kwei and the Li *et al.* formulas are rewritten in terms of angular variables.

Let us consider the component q_{x} and q_{y} of the momentum transfer parallel to the surface. For outgoing electrons,

$$q_{\mathrm{x}} \;=\; \frac{mv}{\hbar}(\theta\;\cos\phi\;\cos\alpha\;+\;\theta_{\mathrm{E}}\;\sin\alpha)\;, \tag{D.1}$$

while, for incoming electrons,

$$q_{\mathrm{x}} \;=\; \frac{mv}{\hbar}(\theta\;\cos\phi\;\cos\alpha\;-\;\theta_{\mathrm{E}}\;\sin\alpha)\;. \tag{D.2}$$

For both outgoing and incoming electrons we have

$$q_{\mathrm{y}} \;=\; \frac{mv}{\hbar}\;\theta\;\sin\phi\;. \tag{D.3}$$

In these equations, α is the angle of the electron trajectory with respect to the normal to the target surface, θ and ϕ indicate, as usual, the polar and azimuth angles, and

$$\theta_{\mathrm{E}} \;=\; \frac{\hbar\,\omega}{2\;E}\,, \tag{D.4}$$

where E is the electron energy and $\hbar\,\omega$ the energy loss.

If z is the coordinate along the normal to the surface target, the probability for inelastic scattering (the differential inverse inelastic mean free path, DIIMFP) will be:

$$P_{\rm outside}(z,\alpha) \;=\; \frac{1}{2\pi^2 a_0 E}\,\int_0^{\theta_{\rm cutoff}} \frac{\theta\;d\theta}{\theta^2\;+\;\theta_{\rm E}^2}\,\int_0^{2\pi} d\phi\;f(z,\theta,\phi,\alpha) \tag{D.5}$$

in the vacuum, and

$$P_{\rm inside}(z,\alpha) \;=\; \frac{1}{2\pi^2 a_0 E}\,\int_0^{\theta_{\rm cutoff}} \frac{\theta\;d\theta}{\theta^2\;+\;\theta_{\rm E}^2}\,\int_0^{2\pi} d\phi\;g(z,\theta,\phi,\alpha) \tag{D.6}$$

inside the material. The cutoff angle is taken to be the Bethe ridge angle [10]

$$\theta_{\rm cutoff} \;=\; \sqrt{\frac{\hbar\omega}{E}}\,. \tag{D.7}$$

It should be noted that in the Chen and Kwei approach, [27] there is no proper limit for the high-momentum cutoff, while there exists a maximum angle, known as the Bethe ridge angle,only up to which electron excitation is allowed [140].

For outgoing electrons, functions $f(z,\theta,\phi,\alpha)$ and $g(z,\theta,\phi,\alpha)$ can be written as:

$$f(z,\theta,\phi,\alpha) \;=\; {\rm Im}\left(\frac{2}{\varepsilon+1}\right)\;h(z,\theta,\phi,\alpha)\;[p(z,\theta,\phi,\alpha)-h(z,\theta,\phi,\alpha)]\;, \tag{D.8}$$

$$g(z,\theta,\phi,\alpha) \;=\; {\rm Im}\left(\frac{2}{\varepsilon+1}\right)\;h^2(z,\theta,\phi,\alpha)\;+\;{\rm Im}\left(\frac{1}{\varepsilon}\right)\;[1-h^2(z,\theta,\phi,\alpha)]\;. \tag{D.9}$$

For incoming electrons, the same functions $f(z,\theta,\phi,\alpha)$ and $g(z,\theta,\phi,\alpha)$ are given by:

$$f(z,\theta,\phi,\alpha) \;=\; \mathrm{Im}\left(\frac{2}{\varepsilon+1}\right)\; h^2(z,\theta,\phi,\alpha)\;, \tag{D.10}$$

$$\begin{aligned} & g(z,\theta,\phi,\alpha) \;= \\ & =\; \mathrm{Im}\left(\frac{2}{\varepsilon+1}\right)\; h(z,\theta,\phi,\alpha)\;[p(z,\theta,\phi,\alpha)-h(z,\theta,\phi,\alpha)]\;+ \\ & +\,\mathrm{Im}\left(\frac{1}{\varepsilon}\right)\;[1-h(z,\theta,\phi,\alpha)p(z,\theta,\phi,\alpha)+h^2(z,\theta,\phi,\alpha)]\;. \end{aligned} \tag{D.11}$$

Functions $h(z,\theta,\phi,\alpha)$ and $p(z,\theta,\phi,\alpha)$ are in turn given by:

$$h(z,\theta,\phi,\alpha) \;=\; \exp\left[\left(-|z|\frac{mv}{\hbar}\right)\sqrt{(\theta\cos\phi\cos\alpha+\theta_{\mathrm{E}}\sin\theta)^2+\theta^2\sin^2\phi}\right]\;, \tag{D.12}$$

$$p(z,\theta,\phi,\alpha) \;=\; 2\cos\left[\left(-|z|\frac{mv}{\hbar}\right)(\theta_{\mathrm{E}}\cos\alpha\;-\;\theta\cos\phi\sin\alpha)\right]\;, \tag{D.13}$$

for outgoing electrons and by:

$$h(z,\theta,\phi,\alpha) \;=\; \exp\left[\left(-|z|\frac{mv}{\hbar}\right)\sqrt{(\theta\cos\phi\cos\alpha-\theta_{\mathrm{E}}\sin\theta)^2+\theta^2\sin^2\phi}\right]\;, \tag{D.14}$$

$$p(z,\theta,\phi,\alpha) \;=\; 2\cos\left[\left(-|z|\frac{mv}{\hbar}\right)(\theta_{\mathrm{E}}\cos\alpha\;+\;\theta\cos\phi\sin\alpha)\right]\;, \tag{D.15}$$

for incoming electrons.

Finally, $\varepsilon(\omega)$ is the dielectric function given by:

$$\varepsilon(\omega) \;=\; 1 \;-\; \frac{\omega_{\rm p}^2}{\omega^2 - \omega_{\rm g}^2 - i\Gamma\omega}\;, \tag{D.16}$$

depending on the electron energy loss $\hbar\omega$, as well as on three parameters, the average excitation energy for valence electrons, $\hbar\omega_{\rm g}$, the damping constant, $\hbar\Gamma$, and the plasmon energy, $\hbar\omega_{\rm p}$.

Appendix E

Paper published during the PhD course and concerning this thesis

1. S. Taioli, S. Simonucci, L. Calliari, M. Filippi, and **M. Dapor**. "Mixed *ab initio* quantum mechanical and Monte Carlo calculations of secondary emission from SiO_2 nanoclusters". *Phys. Rev. B*, 79:085432, 2009.

2. S. Taioli, S. Simonucci, and **M. Dapor**. "SURPRISES: when ab initio meets statistics in extended systems". *Comput. Sci. Discovery*, 2:015002, 2009.

3. **M. Dapor**. "A Monte Carlo investigation of secondary electron emission from solid targets: Spherical symmetry versus momentum conservation within the classical binary collision model". *Nucl. Instrum. Meth. B*, 267:3055, 2009.

4. **M. Dapor**, M. A. E. Jepson, B. J. Inkson, and C. Rodenburg. "The effect of oxide overlayers on secondary electron dopant mapping". *Microsc. Microanal.*, 15:237, 2009.

5. S. Taioli, S. Simonucci, L. Calliari, and **M. Dapor**. "Electron spectroscopies and inelastic processes in nanoclusters and solids: Theory and experiment". *Phys. Rep.*, 493:237, 2010.

6. C. Rodenburg, M. A. E. Jepson, E. G. T. Bosch, and **M. Dapor**. "Energy selective scanning electron microscopy to reduce the effect of contamination layers on scanning electron microscope dopant mapping". *Ultramicroscopy*, 110:1185, 2010.

7. **M. Dapor**, M. Ciappa, and W. Fichtner. "Monte Carlo modeling in the low-energy domain of the secondary electron emission of polymethylmethacrylate for critical-dimension scanning electron microscopy". *J. Micro/Nanolith, MEMS MOEMS*, 9:023001, 2010.

8. M. Ciappa, A. Koschik, **M. Dapor**, and W. Fichtner. "Modeling secondary electron images for linewidth measurement by critical dimension scanning electron microscopy". *Microelectronics Reliability*, 50:1407, 2010.

9. A. Koschik, M. Ciappa, S. Holzer, **M. Dapor**, and W. Fichtner. "A novel Monte Carlo simulation code for linewidth measurement in critical dimension scanning electron microscopy". *Proc. of SPIE*, 7729:77290X-1, 2010.

10. **M. Dapor**, N. Bazzanella, L. Toniutti, A. Miotello, and S. Gialanella. "Backscattered electrons from surface films deposited on bulk targets: A comparison between computational and experimental results". *Nucl. Instrum. Meth. B*, 269:1672, 2011.

11. **M. Dapor**, L. Calliari, and G. Scarduelli. "Comparison between Monte Carlo and experimental aluminum and silicon electron energy loss spectra". *Nucl. Instrum. Meth. B*, 269:1675, 2011.

12. **M. Dapor**. "Secondary electron emission yield calculation performed using two different Monte Carlo strategies". *Nucl. Instrum. Meth. B*, 269:1668, 2011.

13. **M. Dapor**. "Comparison between energy straggling strategy and continuous slowing down approximation in Monte Carlo simulation of secondary electron emission of insulating materials". *Progress in Nucl. Sci. and Technol.*, 2:762, 2011.

14. **M. Dapor**, L. Calliari, and S. Fanchenko. "Energy loss of electrons backscattered from solids: Measured and calculated spectra for Al and Si". *Surf. Interface Anal.*, 44:1110, 2012.

15. **M. Dapor**. "Monte Carlo simulation of secondary electron emission from dielectric targets". *Journal of Physics: Conference Series*, 402:012003, 2012.

16. **M. Dapor**, N. Bazzanella, L. Toniutti, A. Miotello, M. Crivellari, and S. Gialanella. "Backscattered electrons from gold surface films deposited on silicon substrates: A joint experimental and computational investigation to add new potentiality to electron microscopy". *Surf. Interface Anal.*, 45:677, 2013.

Bibliography

[1] W. Bothe. *Handbuch der Physik*, volume 22/2, page 1. Springer-Verlag, Berlin, 1933.

[2] R.D. Birkhoff. *Encyclopedia of Physics*, volume 34, page 53. Springer-Verlag, Berlin, 1958.

[3] H. Ibach. *Electron Spectroscopy for Surface Analysis*. Springer, Berlin, Heidelberg, 1977.

[4] H. Niedrig. *J. Appl. Phys.*, 53:R15, 1982.

[5] J.I. Goldstein, D.E. Newbury, P. Echlin, D.C. Joy, C. Fiori, and E. Lifshin. *Scanning Electron and X-Ray Microanalysis*, page 53. Plenum, New York, 1984.

[6] D.E. Newbury, D.C. Joy, P. Echlin, C.E. Fiori, and J.I. Goldstein. *Advanced Scanning Electron Microscopy and X-Ray Microanalysis*, page 3. Plenum, New York, 1986.

[7] L. C. Feldman and J. W. Mayer. *Fundamentals of Surface and Thin Film Analysis*. North-Holland, New York, Amsterdam, London, 1986.

[8] P. Sigmund. *Particle Penetration and Radiation Effects*. Springer-Verlag, Berlin, 2006.

[9] R. F. Egerton. *Rep. Prog. Phys.*, 72:016502, 2009.

[10] R. F. Egerton. *Electron Energy-Loss Spectroscopy in the Electron Microscope*. Third Edition, Springer, New York, Dordrecht, Heidelberg, London, 2011.

[11] L. L. Carter and E. D. Cashwell. *Particle-transport simulation with the Monte Carlo method*. USERDA Technical Information Center, Oak Ridge, Tennessee, 1975.

[12] F. Salvat, J. M. Fernández-Varea, E. Acosta, and J. Sempau. *PENELOPE: A Code System for Monte Carlo Simulation of Electron and Photon Transport*. Nuclear Energy Agency - Organisation for Economic Cooperation and Development Publishing, 2001.

[13] R. Shimizu and Ding Ze-Jun. *Rep. Prog. Phys.*, 55:487, 1992.

[14] D. C. Joy. *Monte Carlo Modeling for Electron Microscopy and Microanalysis*. Oxford University Press, New York, 1995.

[15] A. F. Bielajew. *Fundamentals of the Monte Carlo method for neutral and charged particle transport*. The University of Michigan, Ann Arbor, 2001.

[16] N. F. Mott. *Proc. R. Soc. London Ser.*, 124:425, 1929.

[17] R. H. Ritchie. *Phys. Rev.*, 106:874, 1957.

[18] H. Fröhlich. *Adv. Phys.*, 3:325, 1954.

[19] J. P. Ganachaud and A. Mokrani. *Surf. Sci.*, 334:329, 1995.

[20] R. H. Ritchie and A. Howie. *Philosophical Magazine*, 36:463, 1977.

[21] P. M. Echenique, R. H. Ritchie, N. Barberan, and J. Inkson. *Phys. Rev. B*, 23:6486, 1981.

[22] H. Raether. *Excitation of Plasmons and Interband Transitions by Electrons*. Springer-Verlag, Berlin, 1982.

[23] D. L. Mills. *Phys. Rev. B*, 34:6099, 1986.

[24] D. R. Penn. *Phys. Rev. B*, 35:482, 1987.

[25] J. C. Ashley. *J. Electron Spectrosc. Relat. Phenom.*, 46:199, 1988.

[26] F. Yubero and S. Tougaard. *Phys. Rev. B*, 46:2486, 1992.

[27] Y. F. Chen and C. M. Kwei. *Surf. Sci.*, 364:131, 1996.

[28] Y.C. Li, Y.H. Tu, C.M. Kwei, and C.J. Tung. *Surf. Sci.*, 589:67, 2005.

[29] A. Cohen-Simonsen, F. Yubero, and S. Tougaard. *Phys. Rev. B*, 56:1612, 1997.

[30] Z.-J. Ding. *J. Phys. Condens. Matter*, 10:1733, 1988.

[31] Z.-J. Ding and R. Shimizu. *Phys. Rev. B*, 61:14128, 2000.

[32] Z.-J. Ding, H. M. Li, Q. R. Pu, Z. M. Zhang, and R. Shimizu. *Phys. Rev. B*, 66:085411, 2002.

[33] W. S. M. Werner, W. Smekal, C. Tomastik, and H. Störi. *Surf. Sci.*, 486:L461, 2001.

[34] S. Taioli, S. Simonucci, L. Calliari, M. Filippi, and M. Dapor. *Phys. Rev. B*, 79:085432, 2009.

[35] S. Taioli, S. Simonucci, and M. Dapor. *Comput. Sci. Discovery*, 2:015002, 2009.

[36] S. Taioli, S. Simonucci, L. Calliari, and M. Dapor. *Phys. Rep.*, 493:237, 2010.

[37] M. Dapor, N. Bazzanella, L. Toniutti, A. Miotello, and S. Gialanella. *Nucl. Instrum. Meth. B*, 269:1672, 2011.

[38] M. Dapor, N. Bazzanella, L. Toniutti, A. Miotello, M. Crivellari, and S. Gialanella. *Surf. Interface Anal.*, 45:677, 2013.

[39] M. Dapor, L. Calliari, and G. Scarduelli. *Nucl. Instrum. Meth. B*, 269:1675, 2011.

[40] M. Dapor, M. Ciappa, and W. Fichtner. *J. Micro/Nanolith, MEMS MOEMS*, 9:023001, 2010.

[41] M. Ciappa, A. Koschik, M. Dapor, and W. Fichtner. *Microelectronics Reliability*, 50:1407, 2010.

[42] A. Koschik, M. Ciappa, S. Holzer, M. Dapor, and W. Fichtner. *Proc. of SPIE*, 7729:77290X–1, 2010.

[43] M. Dapor, M. A. E. Jepson, B. J. Inkson, and C. Rodenburg. *Microsc. Microanal.*, 15:237, 2009.

[44] C. Rodenburg, M. A. E. Jepson, E. G. T. Bosch, and M. Dapor. *Ultramicroscopy*, 110:1185, 2010.

[45] H. A. Bethe. *Ann. Phys. Leipzig*, 5:325, 1930.

[46] R. O. Lane and D. J. Zaffarano. *Phys. Rev.*, 94:960, 1954.

[47] K. Kanaya and S. Okayama. *J. Phys. D. Appl. Phys.*, 5:43, 1972.

[48] A. Jablonski, F. Salvat, and C.J. Powell. *J. Phys. Chem. Data*, 33:409, 2004.

[49] G. Wentzel. *Z. Phys.*, 40:590, 1927.

[50] E. Reichert. *Z. Phys.*, 173:392, 1963.

[51] J. Llacer and E. L. Garwin. *J. Appl. Phys.*, 40:2766, 1969.

[52] M. J. Berger and S. M. Seltzer. *National Research Council Publication, Whasington D.C.*, 1133:205, 1964.

[53] J. J. Ritsko, L. J. Brillson, R. W. Bigelow, and T. J. Fabish. *J. Chem. Phys.*, 69:3931, 1978.

[54] B. L. Henke, P. Lee, T. J. Tanaka, R. L. Shimabukuro, and B. K. Fujikawa. *At. Data Nucl. Data Tables*, 27:1, 1982.

[55] B. L. Henke, P. Lee, T. J. Tanaka, R. L. Shimabukuro, and B. K. Fujikawa. *At. Data Nucl. Data Tables*, 54:181, 1993.

[56] U. Buechner. *J. Phys. C: Solid State Phys.*, 8:2781, 1975.

[57] Z. Tan, Y. Y. Xia, X. Liu, and M. Zhao. *Microelectronic Engineering*, 77:285, 2005.

[58] J. C. Ashley and V. E. Anderson. *IEEE Trans. Nucl. Sci.*, NS28:4132, 1981.

[59] C. J. Powell and J. B. Swann. *Phys. Rev.*, 115:869, 1959.

[60] S. Tanuma, C. J. Powell, and D. R. Penn. *Surf. Interface Anal.*, 17:911, 1991.

[61] M. Dapor. *Surf. Sci.*, 600:4728, 2006.

[62] W. H. Press, S. A. Teukolsky, W. T. Vetterling, and B. P. Flannery. *Numerical Recipes in C. The Art of Scientific Computing*. Second Edition, Cambridge University Press, Cambridge, 1992.

[63] S. E. Koonin and D. C. Meredith. *Computational Physics*. Addison-Wesley, Redwood City, 1990.

[64] T. Kobayashi H. Yoshino S. Horiguchi, M. Suzuki and Y. Sakakibara. *Appl. Phys. Lett.*, 39:512, 1981.

[65] G. Messina, A. Paoletti, S. Santangelo, and A. Tucciarone. *La Rivista del Nuovo Cimento*, 15:1, 1992.

[66] H. Bichsel. *Nucl. Instrum. Meth. B*, 52:136, 1990.

[67] M. Dapor. *Nucl. Instrum. Meth. B*, 267:3055, 2009.

[68] P. Kazemian. *Progress towards Quantitive Dopant Profiling with the Scanning Electron Microscope*. Doctorate Dissertation, University of Cambridge, 2006.

[69] N. Roduit. *http://www.jmicrovision.com*, 2010.

[70] T. Zhenyu and X. Yueyuan. *Scanning*, 24:257, 2002.

[71] M. Dapor, B. J. Inkson, C. Rodenburg, and J. M. Rodenburg. *Europhysics Letters*, 82:30006, 2008.

[72] M. Dapor, L. Calliari, and S. Fanchenko. *Surf. Interface Anal.*, 44:1110, 2012.

[73] M. Dapor. *Nucl. Instrum. Meth. B*, 269:1668, 2011.

[74] M. Dapor. *Progress in Nucl. Sci. and Technol.*, 2:762, 2011.

[75] D.C. Joy. *http://web.utk.edu/∼srcutk/htm/interact.htm*, 2008.

[76] R. Cimino, I. R. Collins, M. A. Furman, M. Pivi, F. Ruggiero, G. Rumolo, and F. Zimmermann. *Phys. Rev. Lett.*, 93:014801, 2004.

[77] M. A. Furman and V. H. Chaplin. *Phys. Rev. Special Topics - Accelerators and Beams*, 9:034403, 2006.

[78] I. M. Bronstein and B. S. Fraiman. *Vtorichnaya Elektronnaya Emissiya*. Nauka, Moskva, 1969.

[79] L. Reimer and C. Tolkamp. *Scanning*, 3:35, 1980.

[80] R. Böngeler, U. Golla, M. Kussens, R. Reimer, B. Schendler, R. Senkel, and M. Spranck. *Scanning*, 15:1, 1993.

[81] S. Tanuma, C. J. Powell, and D. R. Penn. *Surf. Interface Anal.*, 37:978, 2005.

[82] T. Koshikawa and R. Shimizu. *J. Phys. D. Appl. Phys.*, 6:1369, 1973.

[83] O. S. Rayora and A. E. Curzon. *Thin Solid Film*, 123:235, 1985.

[84] O. S. Rayora and A. E. Curzon. *Thin Solid Film*, 199:313, 1991.

[85] O. S. Rayora and A. E. Curzon. *Phys. Stat. Sol. A. Appl. Res.*, 193:319, 1994.

[86] P. Hirsch, M. Kassen, M. Puttmann, and L. Reimer. *Scanning*, 16:101, 1994.

[87] L. Frank, R. Stekly, M. Zadražil, M. M. El-Gomati, and I. Müllerova. *Mikrochim. Acta*, 132:179, 2000.

[88] M. M. El Gomati, C. G. Walker, A. M. D. Assa'd, and M. Zadražil. *Scanning*, 30:2, 2008.

[89] J. Ch. Kuhr and H. J. Fitting. *J. Electron Spectrosc. Relat. Phenom.*, 105:257, 1999.

[90] Y. Lin and D. C. Joy. *Surf. Interface Anal.*, 37:895, 2005.

[91] M. Yasuda, K. Morimoto, Y. Kainuma, H. Kawata, and Y. Hirai. *Jpn. J. Appl. Phys.*, 47:4890, 2008.

[92] C. G. Walker, M. M. El-Gomati, A. M. D. Assa'd, and M. Zadrazil. *Scanning*, 30:365, 2008.

[93] G. F. Dionne. *J. Appl. Phys.*, 44:5361, 1973.

[94] M. Boubaya and G. Blaise. *Eur. Phys. J.: Appl. Phys.*, 37:79, 2007.

[95] É. I. Rau, E. N. Evstaf'eva, and M. V. Adrianov. *Physics of the Solid State*, 50:599, 2008.

[96] M. Dapor. *Journal of Physics: Conference Series*, 402:012003, 2012.

[97] G. F. Dionne. *J. Appl. Phys.*, 46:3347, 1975.

[98] P. H. Dawson. *J. Appl. Phys.*, 37:3644, 1966.

[99] C. G. Frase, D. Gnieser, and H. Bosse. *J. Phys. D: Appl. Phys.*, 42:183001, 2009.

[100] J. S. Villarrubia, A. E. Vladár, B. D. Bunday, and et al. *Proc. of SPIE*, 5375:199, 2004.

[101] J. S. Villarrubia, A. E. Vladár, and M. T. Postek. *Surf. Interface Anal.*, 37:951, 2005.

[102] J. S. Villarrubia, N. Ritchie, and J. R. Lowney. *Proc. of SPIE*, 6518:65180K, 2007.

[103] J. Baró, J. Sempau, J. M. Fernández-Varea, and F. Salvat. *Nucl. Instrum. Methods Phys. Res. B*, 84:465, 1994.

[104] J. M. Fernández-Varea J. Baró, J. Sempau and F. Salvat. *Nucl. Instrum. Methods Phys. Res. B*, 100:31, 1995.

[105] R. M. Martin. *Electronic Structure. Basic Theory and Practical Methods*. Cambridge University Press, Cambridge, 2004.

[106] M. D. Crescenzi and M. N. Piancastelli. *Electron Scattering and Related Spectroscopies*. World Scientific, Singapore, 1996.

[107] R. G. Newton. *Scattering Theory of Wave and Particle*. Springer Verlag, New York, 1982.

[108] J. Daniels, C. V. Festenberg, H. Raether, and K. Zeppenfeld. *Springer Tracts in Modern Physics*, 54:78, 1970.

[109] H. Venghauss. *Phys. Status Solidi B*, 71:609, 1975.

[110] A. G. Marinopoulos, L. Reining, A. Rubio, and V. Olevano. *Phys. Rev. B*, 69:245419, 2004.

[111] M. Dapor, L. Calliari, and M. Filippi. *Nucl. Instrum. Meth. B*, 255:276, 2007.

[112] M. H. Reilly. *J. Phys. Chem. Solids*, 31:1041, 1970.

[113] W. S. M. Werner. *Phys. Rev. B*, 74:075421, 2006.

[114] I. Kyriakou, D. Emfietzoglou, R. Garcia-Molina, I. Abril, and K. Kostarelos. *J. Appl. Phys.*, 110:054304, 2011.

[115] C. J. Tung, Y. F. Chen, C. M. Kwei, and T. L. Chou. *Phys. Rev. B*, 49:16684, 1994.

[116] A. Jablonski and C. J. Powell. *Surf. Sci.*, 551:106, 2004.

[117] F. Yubero, N. Pauly, A. Dubus, and S. Tougaard. *Phys. Rev. B*, 77:245405, 2008.

[118] R. Mayol and F. Salvat. *Atom. Data Nucl. Data Tables*, 65:55, 1997.

[119] G. A. van Riessen, S. M. Thurgate, and D. E. Ramaker. *J. Electron Spectrosc. Relat. Phenom.*, 161:150, 2007.

[120] G. F. Amelio. *J. Vac. Sci. Technol.*, B7:593, 1970.

[121] R. Shimizu. *J. Appl. Phys.*, 45:2107, 1974.

[122] A. Howie. *Microsc. Microanal.*, 6:291, 2000.

[123] A. Shih, J. Yater, P. Pehrrson, J. Buttler, C. Hor, and R. Abrams. *J. Appl. Phys.*, 82:1860, 1997.

[124] F. Iwase, Y. Nakamura, and S. Furuya. *Appl. Phys. Lett.*, 64:1404, 1994.

[125] F. Iwase and Y. Nakamura. *Appl. Phys. Lett.*, 71:2142, 1997.

[126] D. D. Perovic, M. R. Castell, A. Howie, C. Lavoie, T. Tiedje, and J. S. W. Cole. *Ultramicroscopy*, 58:104, 1995.

[127] D. Venables, H. Jain, and D. C. Collins. *J. Vac. Sci. Technol. B*, 16:362, 1998.

[128] S. L. Elliott, R. F. Broom, and C. J. Humphreys. *J. Appl. Phys.*, 91:9116, 2002.

[129] T. H. P. Chang and W. C. Nixon. *Solid-State Electron.*, 10:701, 1967.

[130] N. Ashcroft and N. D. Mermin. *Solid State Physics*. W.B Saunders, 1976.

[131] A. K. W. Chee, C. Rodenburg, and C. J. Humphreys. *Mater. Res. Soc. Symp. Proc.*, 1026:C04–02, 2008.

[132] T. Koshikawa and R. Shimizu. *J. Phys. D. Appl. Phys.*, 7:1303, 1974.

[133] H. J. Fitting, E. Schreiber, J. Ch. Kuhr, and A. von Czarnowski. *J. Electron Spectrosc. Relat. Phenom.*, 119:35, 2001.

[134] S.-R. Lin, N. Sherman, and J. K. Percus. *Nucl. Phys.*, 45:492, 1963.

[135] P. J. Bunyan and J. L. Schonfelder. *Proc. Phys. Soc.*, 85:455, 1965.

[136] F. Salvat, J. D. Martínez, R. Mayol, and J. Parellada. *Phys. Rev. A*, 36:467, 1987.

[137] M. Dapor. *Phys. Lett. A*, 333:457, 2004.

[138] J. B. Furness and I. E. McCarthy. *J. Phys. B*, 6:2280, 1973.

[139] F. Salvat and R. Mayol. *Comput. Phys. Commun.*, 74:358, 1993.

[140] L. Calliari and S. Fanchenko. *Surf. Interface Anal.*, 44:1104, 2012.